POLITECNICO DI MILANO

Positronium formation in Self-Standing Materials for Antimatter Experimentation

Author:

Craig EVANS

Supervisor:

Prof. Rafael FERRAGUT

Coordinator:

Prof. Paola TARONI

Tutor:

Prof. Franco CICCACCI

February 21, 2018

You miss 100% of the shots you don’t take

Wayne Gretzky

ACKNOWLEDGEMENTS

The research presented within this thesis is made up of three years of patience and dedication to the field. I, as one researcher, was not alone in my research endevours. I had the pleasure of meeting and working with a wide range of researchers within my selected field and outside of it all together. This section is to acknowledge the people which have contributed to this final document and the furthering of myself as a well-rounded researcher.

Firstly, I would like to express my sincere gratitude to my supervisor Prof. Rafael Ferragut for the continuous support over the duration of my Ph.D research, for his patience, and immense knowledge. With his expertise within the LNESS positron group, I managed to expand my experimental and theoretical understanding within the field of antimatter. As well as open possibilities for collaboration with members of similar and different disciplines. On a personal level, he was there during any hardship and motivated me to reach the next plateau. I am humbly grateful for the experience and knowledge I have acquired from him during my PhD studies.

The second person I would like to acknowledge is a fellow colleague thoughout my PhD, Stefano Aghion. As a member of the VEPAS lab's team, he and I conversed on new ideas and way of proceeding to the next step. As I have learned with my time in Italy, this is best done over a coffee. I have come to realise that great ideas come when you open up and share ideas with others.

All my efforts would not be possible without the support from INFN. Marco Giammarchi in particular I would like to thank for his continuous appraisal to my missions at CERN and my ventures abroad furthering my results. Special thanks goes to Marco, for personally introducing to fellow researchers who were able to provide their expertise for further undertanding of the properties of the materials presented.

As coming from a Physics background, I was thrown into the deep end with Physical Chemistry for the development phase of the project. Without the guidance of Mariangela

Longhi and Karen Edler, I would not have reached as far as I have in regards to the final result. Opening my mind to a more interdisciplinary mind set has benefitted me as a researcher and hope to continue with further interdisciplinary projects in the future.

The new collaboration for our group was with the people of the Laser irradiation machining group. Rebeca Martínez Vázquez and Roberto Osellame contributed to a key major part of the final target produced. From the get-go, they were open with the capabilities and to try new ways for benefitting the overall result. Without their collaboration, the project would have not exceeded to the level it did.

Last but not least, I would like to thank the members of the AEgIS collaboration. During my time at CERN, I was surrounded by geniuses in their field working together towards a mutual goal. As mentioned in my perspective with intedisciplinary research, having the opportunity to work in this kind of atmosphere built up further motivation towards my final goal, and then to use my research to benefit the collaboration as a whole.

TABLE OF CONTENTS

LIST OF TABLES

LIST OF FIGURES

LIST OF PUBLICATIONS AND PROCEEDINGS OF THE CANDIDATE

[1] C. Evans et al. (AEgIS Collaboration), "Towards the first measurement of matter-antimatter gravitational interaction", EPJ Web Conf. (2018) Submitted.

[2] S. Aghion et al. (AEgIS Collaboration), "Compression of a mixed antiproton and electron non-neutral plasma to high densities", Eur. Phys. J. D (2018) in press.

[3] P. Yzombard et al. (AEgIS Collaboration), "Overview of Recent Work on Laser Excitation of Positronium for the Formation of Antihydrogen", JPS Conf. Proc., vol. 18 (2017) 011026.

[4] G. Consolati et al. (AEgIS Collaboration), "Positronium for Antihydrogen Production in the AEgIS Experiment", Acta Phys. Pol. B, vol. 132 (2017) 1443.

[5] F. Prelz et al. (AEgIS Collaboration), "The DAQ system for the AEgIS experiment", J. Phys.:Conf. Ser., vol. 898 (2017) 032014.

[6] S. Mariazzi, L. Smestad et al. (AEgIS Collaboration), "Charcterization of a transmission positron/positronium converter for antihydrogen production", Nucl. Instr. Meth. Phys. Res., vol. 407 (2017) 55.

[7] S. Mariazzi et al. (AEgIS Collaboration), "Positron Manipulation and Positronium Laser Excitation in AEgIS", Defect and Diffusion Forum, vol. 373, (2017) 11.

[8] S. Aghion et al. (AEgIS Collaboration), "Measurement of antiproton annihilation on Cu, Ag and Au with emulsion films", J. Instrum., vol. 12 (2017) P04021.

[9] R. Caravita et al. (AEgIS Collaboration), “Advances in Ps Manipulations and Laser Studies in the AEgIS Experiment”, Acta Phys. Pol. B, vol. 48 (2017) 1583.

[10] R.S. Brusa et al. (AEgIS Collaboration), “The AEgIS experiment at CERN: measuring antihydrogen free-fall in earths gravitational field to test WEP with antimatter”, J. Phys. Conf. Ser, vol. 791 (2017) 012014.

[11] S. Aghion et al. (AEgIS Collaboration), “Laser excitation of the n=3 level of positronium”, Phys. Rev. A, vol. 94 (2017) 012507.

[12] S. Aghion et al. (QUPLAS Collaboration), “Detection of low energy antimatter with emulsions”, J. Instrum., vol. 11 (2016) P0617.

[13] N. Pacifico et al. (AEgIS Collaboration), “Direct detection of antiprotons with the Timepix3 in a new electrostatic selection beamline”, Nucl. Instr. Meth. Phys. Res., vol. 362 (2015) 86.

[14] A. Kellerbauer et al. (AEgIS Collaboration), “Probing antimatter gravity, The AEgIS experiment at CERN”, EPJ Web Conf., vol. 126 (2016) 02016.

[15] R. Caravita et al. (AEgIS Collaboration), “Towards a gravity measurement on cold antimatter atoms”, Il Nuovo Cimento C, vol. 39 (2016) 6.

[16] S. Aghion et al. (AEgIS Collaboration), “Positron bunching and electrostatic transport system for the production and emission of dense positronium clouds into vacuum”, Nucl. Instr. Meth. Phys. Res. B, vol. 362 (2015) 86.

[17] Y. Rong, D. He, A. Sanchez-Fernandez, C. Evans, K. J. Edler, R. Malpass-Evans, M. Carta, N. B. McKeown, T. J. Clarke, S. H. Taylor, A. J. Wain, J. M. Mitchels and F. Marken, “Intrinsically Microporous Polymer Retains Porosity in Vacuum Thermolysis to Electroactive Heterocrbon”, Langmuir, vol. 31 (2015) 123000.

SUMMARY

Antimatter, the counterpart of ordinary matter, exists in scarce quantities comparing to the abundance of matter in our observable universe. A long journey has been made since the initial postulation by Dirac of the antielectron in 1928 to the current research on antiatomic atoms (antihydrogen, antiprotonic helium) mainly at the Antiproton Decelerator at CERN in Geneva, Switzerland. Physicists around the world are working together searching for differences between matter and antimatter. This thesis project was conducted in collaboration with AEgIS (Antimatter Experiment, gravity, Interferometry, Spectroscopy), a CERN based experiment that wants to create antihydrogen through the charge exchange reaction. This reaction involves antiprotons being introduced to laser excited positronium (Ps). They plan to use this method to create an antihydrogen pulsed beam to observe the shift of its trajectory caused by the effect of the Earth's gravitational field. The idea is to test the matter-antimatter gravitational interaction for the first time. This is a test of the Weak Equivalence Principle, which states that the free fall trajectory of a body does not depend on its composition. In quantum field theory (QFT), gravity has not yet been included unlike the remaining fundamental interactions (electromagnetic, weak and strong). The measurement of the gravitational interaction between matter and antimatter could contribute to elaborate a solid theoretical framework within QFT. The charge exchange reaction requires an efficient source of cold Ps atoms to allow the largest quantity of antihydrogen to be produced. Ps in the triplet state, ortho-positronium (o-Ps), possesses spin 1 (where positrons and electrons spins are parallel) and lives in vacuum an average of 142 ns at the ground state (n=1). The antiproton/Ps interaction demands a longer Ps lifetime and a higher n quantum number. A method which can be used is to increase its lifetime by means of laser excitation. With current laser technology, it is possible to excite o-Ps long enough for the charge exchange process to occur. Excitation to Rydberg levels has been undertaken by the AEgIS experiment last year (n= 1 to 3 and then n= 3 to 20). For o-Ps production,

the widely used method is employing a mesoporous silica target in the reflection geometry. In this geometry, positrons are implanted from one side in this material, form Ps within the pores, thermalize and exit into vacuum from the same implantation side. It is predicted (through simulation) that changing the geometry to transmission (i.e. Ps exit in the opposite direction of implantation) would benefit this process by increasing the quantity of cold o-Ps emission into vacuum.

The VEPAS laboratory of Politecnico di Milano (L-NESS, Como) is involved in the project for the development of these mesoporous silica materials that create a sufficient quantity of Ps inside the pores and then emit them thermalized into vacuum in reflection. The most relevant challenge of this project was to develop for the first time a self-supported target with the ability to emit Ps in the transmission geometry. To accomplish this, it is necessary to overcome an intrinsic difficulty represented by the high fragility of the mesoporous materials to produce a film with the following characteristics: (i) self-supported; (ii) micrometric thickness; (iii) high porosity and low density ($<$1 g/cm^3); (iv) hydrophobicity and (v) interconnected pores with nanometric dimensions (3-15 nm). A variety of physical chemistry techniques were incorporated during the development period including spin-coating, liquid-to-air interface, monolith growth, etc. The more promising film was in the form of the spin-coated films, developed in collaboration with the University of Milan and the SmartMatLab (Milan). This is a consortium of the chemistry department of the university of Milan, CNR and international partners; the Industrie De Nora, CISI scrl, Laboratori Alchemia and Pereoceramics spa. A sol-gel mixture was administered onto a Si [111] substrate, then spun leaving a thin sol-gel material ready for calcination. The mixture consisted of TEOS (Si(OC2H5)4), water (pH= 1.25 with HCl) and ethanol to a molar ratio of (1:5:3.8), a cationic surfactant (CTAB: CH3(CH2)15 N+(CH3)3 Br-) was added to 0.1 CTAB/Si molar ratio and then diluted with ethanol (ratio 1:1). A cylindrical oven was used for the calcination process, removing the unwanted surfactants and leaving a mesoporous silica thin film. The thicknesses were determined to be around 750

nm, measured via HRTEM imaging, where it was also observed that a change in morphology at both the bulk/surface and bulk/substrate interfaces were present, showing an open pore structure. These open pores would greatly benefit the o-Ps emission into vacuum. A polystyrene/toluene-based layer was administered onto the substrate prior to the sol-gel, this layer would then be removed via dissolution to release the sol-gel and allow transferal. A laser-irradiated, chemically etched, holed substrate with transmission $\approx 70\%$ was used as the secondary substrate to allow self-standing to be possible. A continuous positron beam (energy range 0.1-20 keV) based at the VEPAS lab was used to characterize these films to find the Ps production properties within the porous materials. The spin-coated material was found to have a high quantity of o-Ps at low implantation energies ($\approx$1 keV), the estimation for the Ps formation yield was $\approx 65\%$, compared with the historically high Ps producing materials (Aerogel $\approx 60\%$). The pore diameter determined to be 3-4 nm (obtained via a positron lifetime measurement) which falls within an acceptable dimension range predicted from simulation. The development of the self-supported targets is still on-going but initial tests with these prototypes has been proposed within the AEgIS apparatus at CERN to compare to similar targets. The self-supported target to produce Ps in transmission proposed in this thesis are also relevant for other experiments of fundamental Physics as QUPLAS (QUantum interferometry and gravity with Positrons and LASers) that proposes to form a Ps beam to gravitational tests by means of interferometric techniques.

CHAPTER 1
INTRODUCTION

1.1 Positrons

Every elementary particle in our universe has its own antiparticle. The positron is the most readily-available antiparticle here on Earth, the antimatter equivalent of the electron. Paul Dirac in 1928 [1], postulated the existence of antimatter in the form of the anti-electron. Soon after in 1932, this antiparticle was experimentally discovered by Carl Anderson [2], a positive particle (named positron) with a mass much lower than the proton was observed within a Wilson chamber as illustrated in Fig. 1.1. The CPT theorem [3] which is a combination of Charge conjugation (C), Parity (P) and Time reversal (T) is used to determine the properties of all matter and antimatter in our universe. The mass, energy, spin and momentum stay the same whilst the remaining internal quantum numbers change in polarity (charge, baryon number, lepton number, etc.).

When a positron meets an electron at rest, they annihilate into two γ rays with the combined energy equal to the combined mass of the fermion pair. The total energy E is described as,

$$E = 2E_{\gamma} = 2m_0c^2, \tag{1.1}$$

where m_0 is the rest mass of the electron/positron and c is the speed of light. E is equal to 1.022 MeV. These gamma rays (511 keV each) are emitted back-to-back at an angle of ($\theta = \pi$ rad). When the annihilating pair experiences a non-zero momentum before annihilation, this causes a shift in the annihilation angle and emission energies. De Benedetti et al. [4] in 1949 found that the annihilation angle experiences a deviation α with respect to the

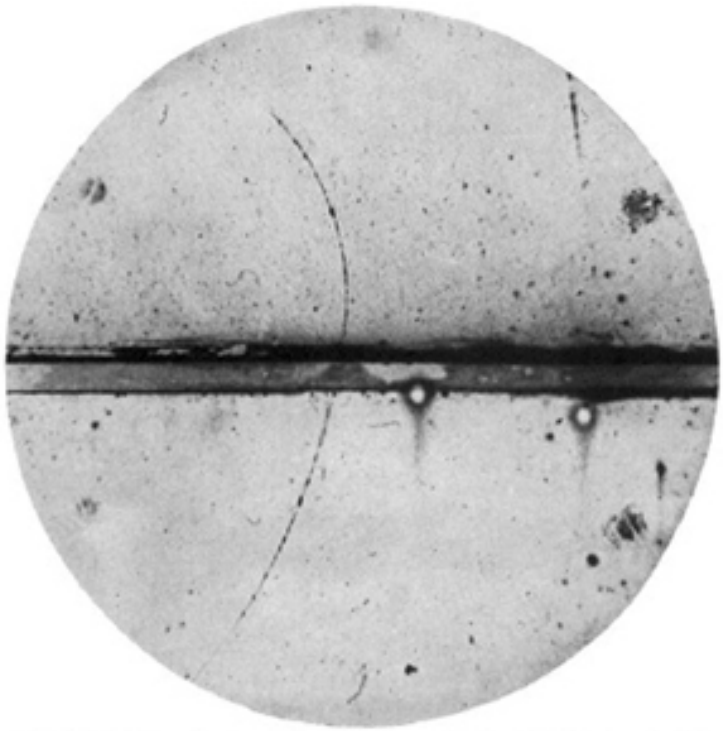

Figure 1.1: The first track observed within a Wilson chamber produced by a positron [2].

laboratory frame. The angle between the two gamma ray annihilation is described as

$$\theta = \pi \pm \alpha, \tag{1.2}$$

where α is in the mrad scale. The energy difference created by this deviation was discovered in the same year by DuMond et al. [5]. When the positron is within a material, it experiences thermalization before it annihilates. The material electrons (in this case) have a higher velocity in comparison to the thermalized positrons. From this, information on the electron momentum distribution of the material could be extracted, this opened the possibility of using positrons for material analysis. Two positron techniques take advantage of this effect [6], Doppler Broadening of the annihilation radiation (see section 2.2.2) and Angular Corrrelation [7, 8]. These non-destructive techniques can be used for the studies of defects within several types of material [9, 10, 11] , Fermi surface mapping [7], mesoporous materials and the observation of positronium production [12].

1.1.1 Positron Sources

Positrons are emitted from a radioactive source during a β^+ decay. A commonly used source for positron experimentation is from the β^+ of an artificially created sodium-22 (^{22}Na) source. The properties of the decay are detailed as

$$^{22}Na \rightarrow {}^{22}Ne + \beta^+ + \nu + \gamma, \tag{1.3}$$

where the γ-ray is emitted with an energy of 1.275 MeV. The sodium isotope has a half-life of around 2.6 years which is useful for longer lasting experiments implementing positrons. Since 90.3% of the decays produced from ^{22}Na results in the emission of a positron, this makes this isotope very useful for positron-related research. Figure 1.2 shows the decay scheme, where the rest of the decays (around 9.7%) leads to an excited neon state, partly due to electron capture from the inner atomic shell. Also, a minority of the positrons decay down directly to the ground state of neon. The energy spectrum (shown in Fig. 1.3) of the

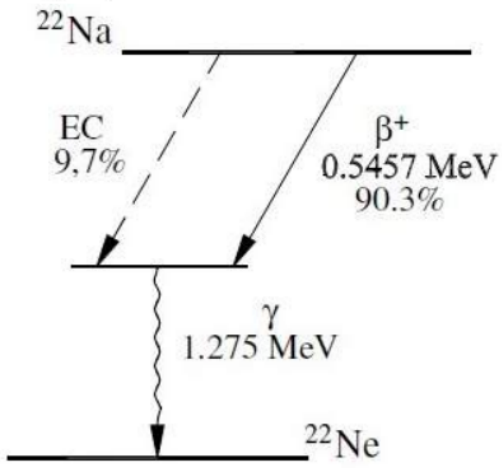

Figure 1.2: Scheme of radioactive decay for ^{22}Na source [6]

positrons emitted by the radioactive decay is of a wide energy range (0-542 keV). As the positron energy increases, this extends the implantion depth reached by the positron within the selected material.

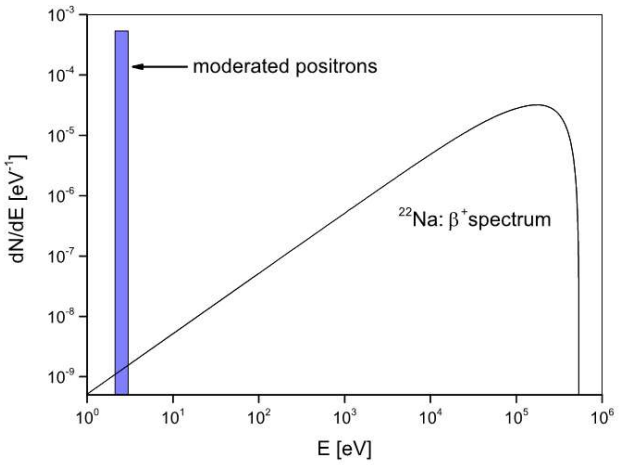

Figure 1.3: Positron emission spectrum of a ^{22}Na radioactive source [13]. This also includes the energy ranges between 1 and 3 eV (shown in blue) which are obtained when the source is coupled with a moderator (explained further in Section 2.2.1). The positrons at these energies are used for creating slow positron beamlines.

1.1.2 Positron Interaction with Matter

In this section, we will discuss the various interactions possible with positrons and solid materials prior to annihilation. When energetic positrons make contact with the target materials surface, a fraction of those do not enter the material, but backscatter (Fig. 1.4(A)). The quantity of positrons backscattered is dependent on three parameters: The initial positron energy, the entrance angle normal to the surface and the atomic number of the material [14]. After the exclusion of the positron which have backscattered, the remaining positrons which do enter the material lose their kinetic energy though several interactions. This stopping process continues until the positron thermal energy threshold is reached. In this state (in regards to metals and semiconductors), the positrons remain in a delocalized Bloch state and diffuse into the material (Fig. 1.4(B)). Less energetic positrons (E$<$1 keV) can reach the surface after initial implantation prior to arriving to the thermal threshold. These can then be remitted into vacuum as epithermal positrons (Fig.1.4 (C)). Positrons which thermalize inside the material can show several possible behaviours prior to annihilation (further explored in Section (1.1.3)). Bulk material diffusion (Fig. 1.4 (D)) where the

positrons remains in the delocalized state until annihilation occurs (see Section (1.1.4)). If the material has defects present, positron diffusion can be interrupted due to the positron becoming trapped within the defect (Fig. 1.4 (E)). This is further explained in Section (1.1.5). This causes high localization of the positron wavefunction and causes the positron to annihilate in a trapping state. De-trapping can occur if the defect is shallow allowing the positron to return to its previous delocalized state. Positrons which enter in open defects (or pores) large enough (>1nm [15]) have the possibility to create positronium atoms Fig.1.4 (F). This topic is described more indepth in Section 1.2.

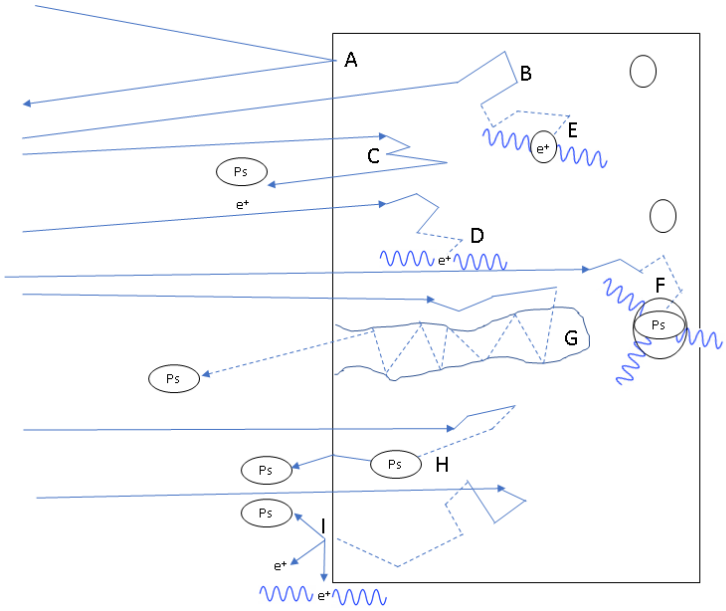

Figure 1.4: The interaction possibilities with a positron and matter. Positron backscattering (A). The implanted positron experiencing a stopping effect which leads to thermalization and diffusion in the material (B). (C) Epithermal positron emission after partial thermalization. (D) Delocalized positron annihilating within the bulk. Positron trapping within a defect of the material and subsequent annihilation (E). (F) The positron inside an open volume forming Positronium (Ps) (nanometric cavity). (G) Ps formation within a defect interconneted to vacuum allowing the Ps to escape. (H) Formation of Ps in the bulk and emission into vacuum from the surface. (I) Backdiffusion of the positron towards the surface leading to either positron emission into vacuum, positron trapping in the surface layer or Ps emission.

1.1.3 Positron thermalization and diffusion

Thermalization (also shown in Fig. 1.4) occurs when a positron is implanted into a sample material. This process reduces the kinetic energy of the positron via scattering events. This process continues down until it reaches the thermal energy ($\frac{3}{2}k_BT \approx 37$ meV) at room temperature. Within matter, the duration of this process is very short, typically from a few, to tens of picoseconds before annihilation occurs (dependent on the target material and the positron incident energy). For high energies after implantation into the material ($>$100 eV), the energy transfer rate is very high, which continue through core ionization (typical for insulators), causing a rapid decrease in energy. In general for high energies, the positron/electron scattering process is dominant. Depending on the properties of the material, different processes can dominate. Different processes can occur between metals and semiconductors within the thermal energy range. For metals under these conditions, the excitation of the conduction electron band dominate. For semiconductors, the dominant process is that of the excitation of the electron hole-pairs, where energies exceed the bandgap. At sub-eV energy levels, phonon scattering becomes dominant.

It is useful to perform positron annihilation spectroscopy (see section 2.1) by means of a slow positron beam since it allows to tune the positron implantation energy and, thus, the depth profile of the implanted positrons within a sample target. In that way, it is possible to conduct depth profile studies on the sample of interest. When monoenergetic positrons are implanted into the matter, e.g. via a positron beam (see section 2.2.1), they first need to thermalize before further processes within the material can take place. The positron implantation or thermalization profile is described by [16],

$$P(z,E) = -\frac{d^{-(\frac{z}{z_0})^m}}{dz} = \frac{mz^{m-1}}{z_0^m}\mathrm{e}^{[-(\frac{z}{z_0})^m]}, \tag{1.4}$$

where m is an adimensional parameter and z_0 is a function that depends on the implantation

energy and described as:

$$z_0 = \frac{\bar{z}}{\Gamma[(\frac{1}{m}) + 1]}, \tag{1.5}$$

where Γ is the Euler gamma function and $\bar{z}$ is the mean positron implantation depth, described by,

$$\bar{z} = \frac{A}{\rho} E^n, \tag{1.6}$$

where ρ is the material density. Examples of the Mahkov implantation profiles showing the differences perceived from a variety of positron implantation energies in Si are shown in Fig. 1.5. The remaining variables (A, m and n) have been determined by the combined results of experimental and Monte Carlo simulation. A = 40 nm g cm^{-3} keV^{-n} [17], m = 2 and n = 1.6 [18]. The stopping power S_p experienced on the positrons is considered under

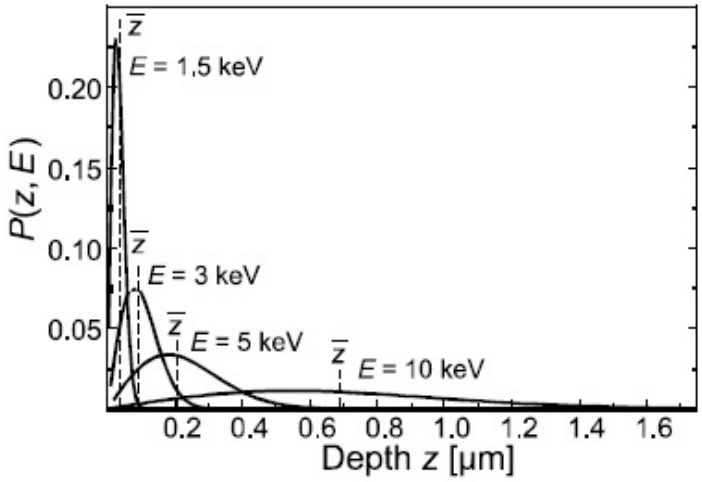

Figure 1.5: Graph showing the differing Makhov profiles at varying positron energies within silicon [6].

a continuous approximation [19], described by,

$$S_p = -dE/dx. \tag{1.7}$$

Regardless of the positron implantation energy, the fast positrons experience a heavy reduction in energy over a time t_{e1}. The positron energy gets reduced down to a lower limit

in the order of ≈100 eV. Once the energies have been reached, Coulomb scattering occurs over time t_{e2} until the threshold energy E_{ph} is reached (≈ eV). Under this energy range, further thermalization occurs from scattering with the phonons of the material. t_{e2} is within the range of $5 \leq t_{e2} \leq 83ps$ which is in the same range as t_{ph} needed to reach the thermal equilibrium energy $\frac{3}{2}k_BT$. The total thermalization time t_{therm} incorporate t_{e1}, t_{e2} and t_{ph} which is estimated by,

$$t_{therm} = \begin{cases} \frac{186.5}{r_s^2}ps & \frac{3}{2}u_{0c} \leq \frac{T}{T_0}, \\ \frac{560}{u_{0c}^2 r_s^2}[(\frac{8}{3}U_{0c})^{\frac{1}{2}} - 1]ps & \frac{3}{2}u_{0c} \leq \frac{T}{T_0}, \end{cases} \tag{1.8}$$

where $u_{0c} = \frac{E_k}{k_B T_0}$, E_k is the positron kinetic energy, r_s the classical electron radius and T_0 = 316 K. To understand the timescale of the thermalization process, for Pb the thermalization time is 45 ps and for Al, 13 ps. After the thermalization ends, the potential of the target material begins to affect the thermalized positrons. The positron kinetic energy at the thermal equilibrium, which is given by,

$$E_k = \frac{1}{2}m_0v^2 = \frac{3}{2}k_BT, \tag{1.9}$$

defines the de Broglie wavelength of the particle. It is informative to express the de Broglie wavelength of a thermalized positron within a bulk of a material as a function of the temperature through,

$$\lambda_B = 61(\frac{316}{T})^{\frac{1}{2}}\mathring{A}. \tag{1.10}$$

In fact, equation 1.10 allows a direct comparison between the positron λ_B and the typical interatomic distances ($a \approx (3-5)\mathring{A}$) from which it is possible to conclude that a thermalized positron can "see" many sites of a lattice. This positron (thermalized)/lattice interaction can provide information on the lattice structure and possible defects present.

The mean positron diffusion length is determined by,

$$L_+ = \sqrt{\tau_b D_+} \tag{1.11}$$

where,

$$D_+ = \tau_r \frac{k_B}{m^*} T, \tag{1.12}$$

where τ_b is the bulk mean positron lifetime and τ_r is the relaxing time for the scattering process (dominant). m^* is the positron's effective mass (1.3-1.7 m_0).

1.1.4 Bulk annihilation

Bulk annihilation happens when the positron remains delocalized within the bulk of a material. The annihilation rate Γ is given by,

$$\Gamma = \pi r_0^2 c \int d^3 r \rho_+(r) \rho_-(r) \gamma(\rho_-(r)), \tag{1.13}$$

where ρ_+ and ρ_- are the positron and electron density, respectively, $\gamma(r)$ is a density dependent enhancement factor which is caused by the strong electron-positron correlation which, in-turn, increases the electron density of the site of the positron. r_0 is the classical electron radius described as,

$$r_0 = \frac{1}{4\pi\epsilon_0} \frac{e^2}{m_0 c^2} \tag{1.14}$$

The annihilation rate scales with the density whilst the positron lifetime scales inversely ($\tau = \Gamma^{-1}$).

1.1.5 Defects

Dislocations (or vacancies) within materials represent deep potential wells that trap the positrons. Positrons can be used as an effective probe for material defects due to the properties of the wave function when thermalized (reaching to 10^5-10^6 lattice cells over its

lifetime). An estimation can be undetaken by assuming some primary parameters, λ_B= 60 $\mathring{A}$, interatomic distance of a = 3-5 $\mathring{A}$ and the positron diffusion length of 100 nm. Using the Fermi Golden rule, the trapping rate k can be determined as [20],

$$k = \frac{2\pi}{\hbar} \sum_{i,f} P_i M_{if}^2 \delta(E_i - E_f) \tag{1.15}$$

where M_{if} is the transition element matrix from the initial state i (delocalized wave) to the final state f (localized state), P_i is the occupational probability of the i state. E_i and E_f are each energy at the initial and final states respectively. k can be further simplified and is found to be proportional to the defect concentration C as shown here,

$$k = \mu C, \tag{1.16}$$

where μ is the trapping coefficient due to the nature of the specific defect [6].

1.2 Positronium

Positronium (Ps) is a bound state of an electron and a positron. The existence of this matter/antimatter bound state was predicted by Mohorovičić in 1934 [21]. This is a hydrogen-like atom with a reduced mass of $m_0/2$, this change from hydrogen halves the energy levels compared to hydrogen. Because of this, ground Ps has a binding energy of approximately -6.8 eV. The term "positronium" was proposed by Ruark [22] in 1945. Ps is quasi-stable as it is susceptible to annihiation over a period of time. The lifetime of Ps depends on the spin state where two exist, the singlet ($S = 0$) and triplet state ($S = 1$). The electron and positron within the singlet state have antiparallel spins and experience a mean lifetime of 125 ps in vacuum. This is called para-positronium (p-Ps) and the lifetime was predicted by

Pirenne (1947) [23] and is given by,

$$\Gamma_{2\gamma}(^1S_0, n_{Ps}) = \frac{1}{2}\frac{mc^2}{\hbar}\frac{\alpha^5}{n_{Ps}^3}, \tag{1.17}$$

where n_{Ps} is the Ps quantum number, m_0 is the electron mass, α is the fine-structure constant and $\hbar$ is Planck constant. When annihilation occurs with p-Ps, mainly two gamma rays are produced with energies equal to the combined mass of the electron-positron pair. The difference in the triplet state is that the spins are parallel and has a longer mean lifetime of 142 ns in vacuum and annihilates mainly into three gamma rays. This is called ortho-positronium (o-Ps) and the lifetime was correctly predicted by Ore and Powell (1949) [24] and determined by

$$\Gamma_{3\gamma}(^3S_1, n_{Ps}) = \frac{2}{9\pi}(\pi^2 - 9)\frac{mc^2}{\hbar}\frac{\alpha^6}{n_{Ps}^3} \tag{1.18}$$

The experimental discovery of Ps by Deutch (1951) [25] was performed within various gases.

1.2.1 Positronium formation

Observations of Ps formation are usually found when positrons interact with homogeneous materials, mainly within alkali solids and amorphous materials which feature insulating properties (molecular or ionic). However, some crystalline materials have been shown to produce Ps (e.g. quartz, which was found to be p-Ps dominated) but this is in the minority. In the case of metals and semiconductors, no Ps has been observed experimentally within. For metals, this is due to the high electron density. The time the positron takes to reach an electron is too short to allow Ps formation. For semiconductors, it has been hypothesized [8] that the Ps radius is much wider comparing to regular Ps formation ($\approx 2\mathring{A}$) due to electric fields present. Because of this, the positron subsequently annihilates with another electron preventing the annihilation of Ps in three gamma rays as o-Ps, rendering Ps measurement impossible.

Two ways of modelling the Ps atom within an insulating (crystalline) material are based on models relating to excitons and electron-hole couples [19]. The exciton-based models have two cases. The first model is that of the Wannier exciton, the Ps atom is modelled with an electron-positron distance (radius r) larger than interatomic distances. The effective mass approximation for the electron and positron is valid within this model, making it semiclassical. It is possible to determine that Ps travels as an atom with a mass ($2m_{e^-}$) and the wavefunction is determined to be hydrogen-like where the radius a is,

$$a = \frac{a_0 \epsilon m_{e^-}}{\mu} \tag{1.19}$$

where ϵ is the static dielectric constant, μ is the effective reduced mass and a_0 is the Bohr radius. For the Ps behaviour within semiconductors, this model works well due to the high dielectric constants (as semiconductors have).

The second model is based on the Frenkel-Mott exciton theory, where the electron/ positron radius is comparable to the interatomic distances, in-turn the size is also similar. Because of this, the effective mass approximation does not apply. The calculation of the electric, magnetic fields and annihilation rates are possible with this model. A main difference with this scheme is that the wave function is represented by the sum of the Ps eigenstates [19].

The main use of this model is opening the ability to calculate the Ps properties within a material, the two dominant Ps formation processes within this method are described via the Ore gap and the spur models.

From the Ore gap model [26], the electron transfer reaction is described as,

$$e^+ + M \rightarrow Ps + M^+ \tag{1.20}$$

where M is the medium molecule, the Ps energy is described as $E_{Ps} = E_{e^+} - I_m + I_{Ps}$ when the reaction is adiabatic. I_m and I_{Ps} is the ionization potential of the medium and Ps,

respectively. The energy range needed for Ps formation is $I_m > E > I_m - I_{Ps}$ to avoid the probability of ionization ($E > I_m$) and to have enough energy ($E < I_m$) for the reaction to take place. Thus, with the assumpton that the positron energy distribution is constant ($E < I_m$), the maximum probability is determined as,

$$P_{max} = \frac{I_{Ps}}{I_m}. \tag{1.21}$$

The Ore gap model can be explained from the use of these principles. This model works well for diatomic gases as well as a good basis for semiconductor prediction. But for polyatomic systems, this model loses its usefulness.

The "modified" spur model [27] consists of two types of reactions listed as,

$$e^+ + M \rightarrow M^+ + e^+ + e^-, \tag{1.22}$$

and,

$$e^+ + M \rightarrow M^+ + (e^+ + e^-). \tag{1.23}$$

The reaction shown in (1.21) would lead to a probability described as,

$$P = 1 - exp(-\frac{e^2}{\epsilon k_B T r_t}), \tag{1.24}$$

where r_t is the distance between the thermalised positron and electron, e is the electron charge and T is the absolute temperature. This process occurs when the total kinetic energy of the positron-electron pair is larger than the potential energy between them. For the second case (equation (1.22)), the kinetic energy of the pair is less. If there is one positron and α pairs of positive ions and electrons, the kinetic energy of the positron would be sufficient to not be influenced by the electrons, but over time this would change and neutralize. In a system of randomly positioned charged particles, the probability can be statistically

described as,

$$P = \frac{\alpha}{(\alpha + 1)}. \tag{1.25}$$

From here, two Ps formation processes are probable, via coulombic influence (P_0) or the combination of the free electrons and positrons inside the spur (P_{sp}). Both of these are incorporated to obtain the total positronium formation probability P_t as,

$$P_t = P_0 + P_{sp} - P_0 P_{sp}. \tag{1.26}$$

1.2.2 Positronium formation on surfaces

As shown previously in Fig. 1.4, Ps can form from positron interaction with matter. One possible mechanism for Ps formation is when positrons diffuse towards the surface after initial implantation, to then form Ps at the surface, that mainly escape into vacuum. Generally, Ps diffusion into a condensed matter medium is extremely slow comparing to Ps interaction with porous materials.

Positronium emission from a surface is highly dependent on the Ps work function W_{Ps} of the material, shown as

$$W_{Ps} = -\mu_{Ps} + E_B - \frac{R_{inf}}{2}, \tag{1.27}$$

where R_{inf} is the Ps energy in vacuum, E_B is the bound energy of the Ps atom inside the material and μ_{Ps} is the chemical potential defined as,

$$\mu_{Ps} = \mu_+ + \mu_- = -W_+ - W_-. \tag{1.28}$$

where μ_+ and μ_- are the electron and positron chemical potentials. Ps is emitted into vacuum only if the Ps work function W_{Ps} is less than zero. Ps in silica is emitted at 1 - 3 eV [28]. Another possible way of creating surface Ps is from a thermalized positron (mentioned prior) diffusing back to the surface and taking an electron as it exits. These processes are very common when positrons are implanted into matter near the surface or

within porous materials.

1.2.3 Positronium diffusion and cooling in porous materials

A model for positronium diffusion and cooling inside silica with inteconnected pores was proposed in [29]. This section briefly describes the concepts and ideas of this work. The Ps created within these pores have the ability to lose energy (thermalize) via collisions with the pore walls. These collisions are described via a quantum mechanical model where the Ps interact via scattering with the phonons present at the pore wall surface [30]. For one, diffusion is dependent on the Ps energy (E_{Ps}). Non-thermal diffusion comes into play due to this process being undertaken at a relatively slower rate. Two factors can affect the quantity of Ps emitted into vacuum, the implantation depth in the material and the Ps behaviour within the cavities of the material in question. The Ps yield can be simply described as a function of the positron implantation energy (K) with the assumption that the diffusion coefficient (D_{Ps}) is a function of the Ps kinetic energy (E_{Ps}) as,

$$D_{Ps}(E_{Ps}) = \frac{\Lambda}{3C}\sqrt{\frac{2E_{Ps}}{m_{Ps}}}, \tag{1.29}$$

where Λ is the seperation between pores, C is the mean collisions per pores and m_{Ps} is the Ps mass. From this the Ps yield for the triplet state can be derived to,

$$f_d = \frac{f_0}{1 + \bar{x}/\sqrt{D_{Ps}\tau}}, \tag{1.30}$$

where f_0 is the Ps branching ratio at the surface and τ the lifetime. $\bar{x}$ is the mean implantation depth and is described by,

$$\bar{x} = \frac{A}{\rho}K^{\nu} \tag{1.31}$$

where A = 2.81 μg/cm^2 [31], ρ = 1.35 g/cm^3 is the mean material density (for the mesoporous silica) and ν is $\approx$1.7. The behaviour of the Ps atoms in a porous media can be

modelled if we consider Ps as a classical particle bouncing between the pore walls and assume the Ps atom would diffuse towards the surface at Γ mean free path (pore spacing in this case). The final energy E_{Ps} can be derived as,

$$E_{Ps}(K) = E_i exp(-3\alpha A^2 K^{2\nu} C^2/\rho^2\Lambda^2) + E_{min}, \tag{1.32}$$

or in a simplified term,

$$E_i exp(-QK^{2\nu}) + E_{min}, \tag{1.33}$$

where α is the fractional energy loss at each interaction and E_{min} is the minimum average total energy of a thermalized Ps atom within a pore. $Q = 3\alpha A^2 C^2/\rho^2\Lambda^2$. For mesoporous silica, α has been found to be $\approx 8 \times 10^{-5}$ [29]. The number of collisions N is described as,

$$N = 3(\bar{x}/\Lambda)^2 C^2 = \frac{3A^2 K^{2\nu} C^2}{\rho^2\Lambda^2}. \tag{1.34}$$

In the case for high positron implantation energies (K>2 keV), D_{Ps} becomes constant. So F_d becomes,

$$f_d = \frac{f_0}{1 + (K/K_0)^\nu}, \tag{1.35}$$

where K_0 is the implantation energy for which approximately 50% of the Ps is able to reach the suface, this term is called "half-energy". For lower implantation energies, equation (1.35) does not accurately model the behaviour of Ps within a porous material. This is due to thermalization not being taken into account and due to the dependence on K for Eqs. (1.29) and (1.33) [29]. So, for low energies, Eqs. (1.29), (1.30), (1.31) and (1.33) need to be combined to allow a more accurate estimation for the triplet state Ps yield. Doing so obtains this expression,

$$f_d = \frac{f_0}{1 + K^\nu A_1^{-1}(E_i exp(-QK^{2\nu}) + E_{min})^{-\frac{1}{4}}}. \tag{1.36}$$

In the case when K = K_0, the implantation depth can be approximated to be equal to the mean diffusion length ($L \approx \bar{x}(K_0)$. This can be shown as,

$$L = \frac{A}{\rho} K_0^{\nu} = \sqrt{2 D_{Ps} \tau L}, \tag{1.37}$$

where τ_L ($\tau/2$)) is the average time for the Ps atom to arrive at the surface from a depth L. For positron implantation energies greater than 2 keV, the Ps has the ability the thermalize within the pores. The mean time needed for Ps emission after implantation, taking into account the diffusion into the pores, is determined as,

$$t = \frac{\bar{x}^2}{2 D_{Ps}} = \frac{A^2}{2 D_{Ps} \rho^2} K^{2\nu}, \tag{1.38}$$

and from this, Ps-based products ($Ps, Ps^+, Ps^-, etc.$) have enough time to be emitted out of the pores.

Freshly formed Ps due to the quantum confinement effect, can cool down to a threshold of,

$$E_0 = \frac{\pi \hbar^2}{2 m_{Ps} a^2}, \tag{1.39}$$

within a pore, where $\hbar$ is the Planck constant, m_{Ps} is the Ps mass and a is the radius of the pore. As an example, thermalization of Ps can not be undertaken at room temperature with a material of pore sizes smaller than 3 nm ($E_0 \approx$ 42 meV). Comparing this to the thermalization energy E_{th} at room temperature described as,

$$E_{th} = \frac{3}{2} k_B T, \tag{1.40}$$

which is calculated to be around 38.5 meV This also does not take into account the pick-off effect also present and more prevalent with smaller pore sizes [11], thus reducing the probability.

CHAPTER 2

POSITRON ANNIHILATION SPECTROSCOPY TECHNIQUES

2.1 Positron Annihilation Lifetime Spectroscopy (PALS)

2.1.1 Concept

Positron Annihilation Lifetime Spectroscopy (PALS) is a method of obtaining information on, defects of metals and metal alloys [9], semiconductors [10], on free volumes in polymers [11] and for conducting morphology studies of mesoporous materials [12]. This type of spectroscopy measures the lifetime of positrons and positronium within a material that normally follows a series of exponential decays. Indeed a positron lifetime spectrum is a composition of exponential decays, i.e. the components of the spectrum, each one attributed to a specific phenomenon. For mesopores in particular the information on their morphology, i.e. the pore sizes and their interconnectivity, is to be found in the ortho-positronium annihilation events. This constitutes the longest components of a spectrum, usually in the range between $10^{-8} - 10^{-7}$s. The o-Ps lifetime can be used to calculate the sizes of the pores through the Tao-Eldrup model [32], which describes Ps behaviour within different pore-like strutures.

2.1.2 Experimental setup

This section introduces a conventional set-up used for PALS measurements in homogeneous materials.

One of the more commonly used positron sources is ^{22}Na. It is administered in the form of an aqueous solution of sodium chloride, dried between two sheets of kapton foil. Kapton is commonly used in lifetime spectrometers for its mechanical and thermal properties [33]. In order to perform a measurement, a "sandwich" configuration is implemented where two

samples of the same material are placed on either side of the source, with two scintilators assigned to the Start and Stop signals. The former is obtained from the 1.275 MeV gamma ray, produced when a positron is emitted (see Sec. 1.1.1), and the latter is given by the positron annihilation gamma ray. The scheme of a positron lifetime spectrometer in a fast-fast configuration is shown in Fig. 2.1. For the initial step for gamma ray detection,

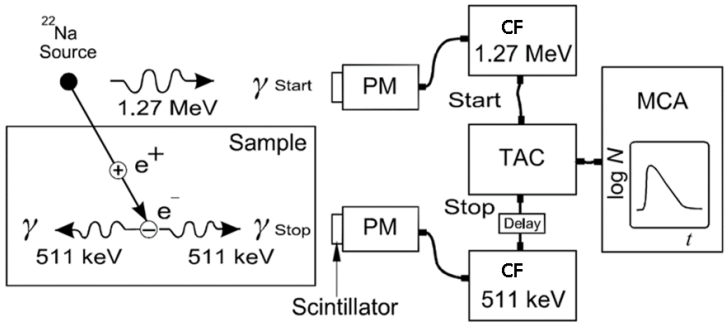

Figure 2.1: Layout of the lifetime experiment based at the VEPAS lab, The lifetime runs in a fast-fast coincidence and measures the time difference between the start and stop signals via two photomultipliers [6].

the scintillating crystal (PilotU for the start signal and BaF_2 for the stop signal in our case) converts the incoming gamma ray to visible or ultraviolet radiation ranges (via fluorescence processes) [34]. Either photoelectric absorption by the core electrons, Compton scattering or the production of electron-photon couples can take place when the gamma ray penetrates into the scintillator. Electrons of the scintillator can absorb photoelectrically the incoming gamma ray.

Each scintillator is coupled with a photomultiplier (PM). The anode exit of each PM is connected to a constant fraction discriminator (CFD), these are used to generate and feed fast logic signals to the time to amplitude converter (TAC).

A delay is incorporated ($\approx$ few ns) to reduce and avoid non linearities within the TAC experienced at low time intervals. With the time delay excluded, the time elapsed between the Start and Stop signals is proportional to the amplitude produced by the TAC. Conversion of the analog signal and storage of the digital information are done via a coupled system

of an analog-digital converter (ADC) and a multichannel analyzer (MCA) or an emulation card connected to a PC.

2.1.3 Data analysis

An analysis software suite called PATFIT-88, was specifically developed for the analysis of positron lifetime spectra [35]. PATFIT-88 is used when the spectrum can be decomposed into discrete components, e.g. when the distribution of pore sizes are narrow enough in a mesoporous material. POSITRON-FIT, a program included in the PATFIT suite, is implemented to extract information of the specific lifetime components within a material. POSFIT (or LT) is another software that allows the components to be set to discrete and/or continuous [36]. POSFIT is mainly used when there is a significant distribution of the pore sizes within the material, therefore, a continous distribution of lifetimes.

POSITRON-FIT is based on a model summing up the exponential decays, convoluted with the lifetime spectrometer resolution function. The spectrum is described as,

$$f(t) = \sum_{j=1}^{k_0} (a_j * R)(t) + B, \tag{2.1}$$

with parameters of

$$a_j = \begin{cases} A_j e^{-\frac{t}{\tau_j}}, & t > 0 \\ 0, & t < 0 \end{cases} \tag{2.2}$$

where k_0 is the assumed number of components (dependent on the quality of the electronics), R is the resolution function, B background, a_j being the decay function (j-th component). A_j is a pre-exponential factor given by,

$$A_j = \frac{I_j}{\tau_j}, \tag{2.3}$$

where τ_j and I_j are the average lifetime and the lifetime intensity of the j-th component.

The resolution function R depends on the experimental set-up but can be modelled as a sum of one or more k_p gaussian functions described by,

$$R(t) = \sum_{p=1}^{k_p} \frac{w_p}{\sqrt{2\pi}\sigma_p} exp(-\frac{(t - t_0 - \Delta t_p)^2}{2\sigma_p^2}), \tag{2.4}$$

where Δt_p and t_0 are the time displacement and the zero time channel respectively. σ_p is the standard deviation charateristic of each gaussian curve. In the case of our form of analysis, the resolution curve consists of one single gaussian curve where the value for σ can be derived by performing a measurement with a ^{60}Co [37]. A single gaussian is enough for our analysis due to the low feedback from the electronics present.

Estimation of the individual mean lifetime τ_j and factor A_j can be undertaken. And from this, the individual intensities I_j can then be calculated. The code performs the fit according to the minimum square method, i.e. by the minimization of the following equation:

$$\chi^2 = \sum_{i=1}^{n} w_i \mid y_i - f_i \mid^2, \tag{2.5}$$

where f_i is the predicted count of the i-th channel, y_i is the real count rate of the i-th channel and w_i is the reciprocal of the variance of the error distribution (typically gaussian) associated to the value of the i-th component. A requirement the program demands is the quantity of components expected in the material to create an estimation of the intensities and lifetimes. The goodness of the fit is normally evaluated by means of the chi-squared test which requires the calculation of χ^2 divided by the degrees of freedom, i.e. the total number of points minus the number of free parameters. Some programs (Matlab, Origin) usually use other crieteria for determining the goodness of the fit (R^2) [38].

2.2 Variable Energy Positron Annihilation Spectroscopy

The Variable Energy Positron Annihilation Spectroscopy (VEPAS), is a research based platform within the L-NESS centre in Como. The main research directions followed with

VEPAS is the study and characterization of metals, metal alloys, semiconductors, polymers, oxides and mesoporous materials. The main apparatus within the lab is in the form of a slow continuous positron beam. This operates in an entirely electrostatic regime with no magnetic components present.

2.2.1 Slow Positron Beam

Positron source and moderation

The source of positrons used for this system is sodium-22 (^{22}Na). This emits positrons via a beta decay mechanism as described in Chapter 1, where the positrons are emitted with a broad energy distribution of 0-542 keV as shown in Fig. 1.3.

For slow positron experimentation, a moderation step is introduced. A tungsten (W) single crystal [001] orientated thin film (1μm in thickness) is placed in front of the source capsule. From the tungsten, around 87% of the incoming positrons are emitted in an unthermalized state, due to the mean implantation depth being much greater than the W thickness. A second fraction (around 13%) are not energetic enough to be emitted and they subsequently diffuse, thermalize and annihilate within the W bulk structure. A small fraction of positrons thermalize within the foil and are emitted with kinetic energies around 1-3 eV (see Fig. 1.3). Positrons are spontaneously emitted from the surface due to the negative positron work-function of the material. These positrons form the beam. The efficiency of the moderator is around 10^{-4} [39].

Electrostatic System and Sample Chamber

The slow positron beam in Como accelerates the positrons via electrostatic optics, as shown in Fig. 2.2. The initial step is to perform an extraction of the emitted moderated positrons via a modified Soa gun (Further information on the electrostatic design can be found in Ref. [40]). This modified Soa gun is located at front of the source and moderation region. The extraction is done via the difference in voltage from the moderator and the extraction

electrode from the Soa gun. This induces a potential on the moderated positrons and with the current set-up allows a variation in positron energy (0.1-20 keV). The electrodes located after the Soa gun are used for further guiding and focusing of the low energy positrons towards the bending region. This is also used as a way of removing the background for the detectors that would be produced by the higher-energy positron annihliations hitting the target. In order not to allow highly energetic positrons to reach the sample chamber, a set

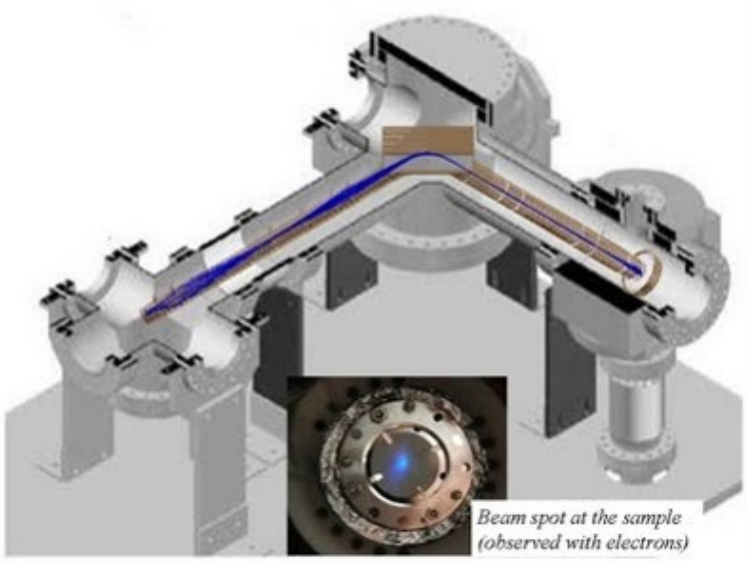

Figure 2.2: 3D schematic of the variable energy positron beam based in the VEPAS lab. In blue, the particle trejectories simulated through SIMION [41]. The bender is located at the center of the system where the beam is redirected towards the sample chamber.

of bending electrodes are used. These cause a 90 ° change in direction of the monoenergetic positrons, as shown in Fig. 2.2. The re-directed positrons are then refocussed by the first electrode of the second array, then accelerated by the proceeding. The final electrode is a three way-segmented lens, which is used to focus the beam onto the sample, with a beam diameter around 2-3 mm (FWHM). The various voltages of the scheme are shown in Fig. 2.3

The samples studied with the VEPAS beam are mounted on a grounded copper holder which is placed on the beam axes. The positioning procedure involves the use of a reference red laser previously aligned with the positron beam.

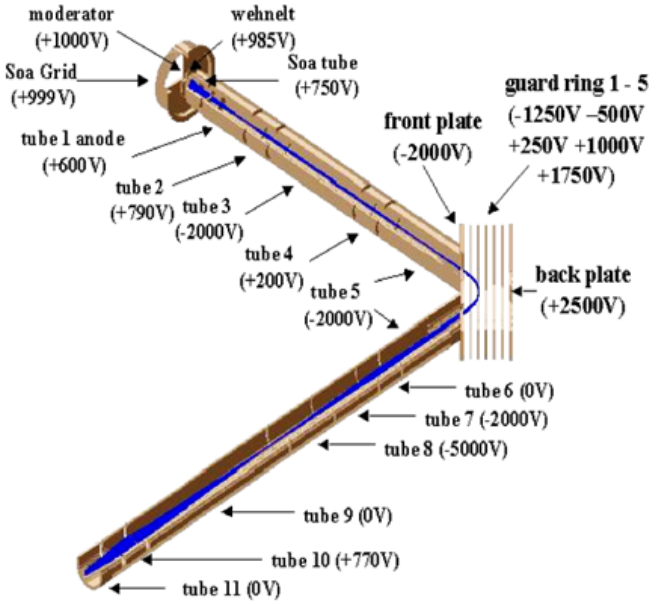

Figure 2.3: 3D simulation of the VEPAS beam.

To obtain a high positron transport efficiency the minimum implantation energy is 1 keV for the system at L-NESS. To obtain a lower positron implantation energy, a positive bias potential is set onto the copper holder and the target. With this method, 0.1-0.9keV are possible with potentials from 900-100V applied to the target, respectively.

Detection System

For the detection of gamma-rays, high-purity germanium (HPGe) detectors are used. The reason for the high-purity is related to the detector efficiency. In-fact, due to the high penetrating power of the gamma rays within matter, the depletion depth needs to be the order of 1 cm [34]. It is possible to tune the depletion depth d by controlling the net impurity concentration N. They are related through the following formula:

$$d = (2\epsilon V/eN)^{1/2}, \tag{2.6}$$

where ϵ is the dielectric constant, e is the electron charge and V is the reverse bias voltage. However, to reach such a thick depletion depth, it is necesary to obtain a very low impurity concentration of 10^{10} atoms/cm^3, as it is for the HPGe detectors employed in the VEPAS lab.

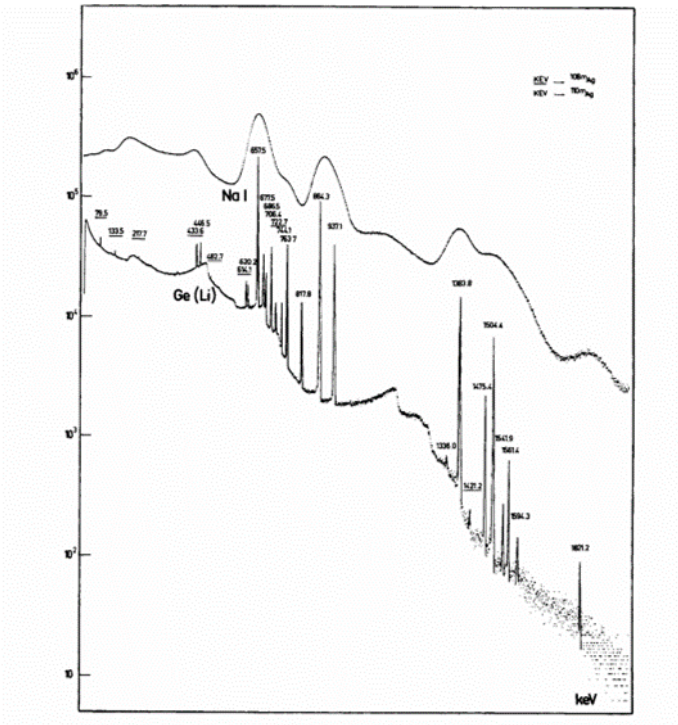

Figure 2.4: Comparison between the detection of ^{108}Ag and ^{110}Ag sppectra obtained with the NaI scintillator and HPGe detector [34]

During operation, a cryogenic dewar is utilized to keep each germanium detector at a cold temperature (around 77 K). This is needed due to the small band-gap (0.7 eV) for Ge. This small bandgap at room temperatures allows leakage currents (thermally-induced), the thermal noise produced from this effect would render the detector unusable.

The benefit of using HPGe detectors is for the energy resolution, closely spaced gamma-ray energies as shown in Fig. 2.4 are easily distinguishable, especially for the spectrum of energies produced from the positron annihilations. The resolution of a single peak (FWHM) depends on the energy of the gamma ray and for the 511 keV the resolution is approximately 1.3 keV [34]. The incoming gamma rays are detected by firstly enter-

ing the germanium, it is then absorbed by the germanium, this is converted into a number of electrons proportional to the initial photon energy (at the interband level). The excited electrons are transported and stored via the potential (≈keV) across the germanium unit. Under a reverse bias voltage, an electric field runs both the depleted and pure regions and gathers the electrons and the holes to the electrodes at which the potential is applied.

2.2.2 Doppler Broadening Spectroscopy

This technique involves the detection of momentum for the annihilation radiation produced from the electron and positron, this is called Doppler Broadening Spectroscopy (DBS). This method opens the possibility of exploring defects and electronic structure of material. A typical experiment would utilize a ^{22}Na source or a slow positron beam coupled with a single HPGe detector. A benefit of a beam (with variable energies) is the ability to explore the Doppler spectrum at different material depths. Properties of the material can be observed as a function of the implantation profile. With this technique, it is also possible to obtain information of the production of positronium at surfaces and within porous materials. Positronium can be used as a probe for examining voids and cavities.

If the center of mass of the annihilating couple (e^+ and e^-) was at rest in respect to the laboratory frame of reference, the two gamma rays would be anti-parallel, each with exactly 511 keV in energy. However, within a material, the center of mass of the positron/electron couple is not at rest and its momentum is almost equal to the material's electron momentum (since the velocity of the positron (after diffusion) is much slower than the material electrons present). Therefore, the two annihilating gamma rays are affected by Doppler shifts, which brings information of the electron momentum distribution. In the direction of the gamma rays (z), the momentum p_z causes a Doppler shift ΔE for the 511 keV annihilation photons ($\Delta E = p_z c/2$).

From numerous events detected, the complete Doppler spectrum would become broadened due to the individual shifts across the direction of annihilation. The momentum in the

x and y direction (P_x, P_y) cause a deviation of an angle (Θ) disturbing the collinearity of the annihilating γ-rays described by,

$$\Theta_{x,y} = \frac{P_{x,y}}{m_0 c}, \tag{2.7}$$

where m_0 is the rest mass of the electron. The technique that measures the deviation in angle is called ACAR (Angular Correlation of positron Annihilation Radiation) [6].

S and W parameters

From the subsequent annihilation of the positrons from interaction with a material, a 511 keV peak broadened by the Doppler effect is produced, as shown in Fig. 2.5. Two parameters are obtained from this peak, the S (Shape) parameter and the W (Wing) parameter also shown in Fig 2.5. Those parameters correspond to the area of the spectrum A_S under the energy range of 511$\pm$ 0.85 keV for the S-parameter and the area A_W within the range from 511 $\pm$ 1.8 keV to 511 $\pm$ 4 keV for the W-parameter. The total area A_T of the annihilation peak is calculated in the range of 511 $\pm$ 4.25 keV. The S-parameter provides information

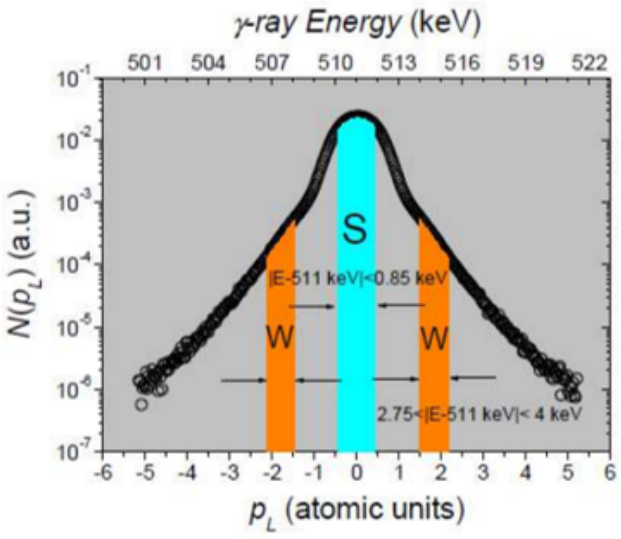

Figure 2.5: Typical spectrum of the summed counts across both detectors with the S and W parameters specified.

on the annihilating para-positronium (p-Ps) atoms and positron annihilation with the conduction and valence electrons (low momentum electronic distribution). The W-parameter provides information on the positron to core electron annihilations (high momentum distribution) when positrons are implanted. To take a relevant example of this with the work presented, for a positron within a vacancy, it is more probable for it to bind with a valence electron and produce a larger conribution to the peak (normalized to the overall area). To experimentally obtain the information for the S parameter, the area under the S peak (A_S) is divided by the total area (A_T). For the W parameter both wing areas (A_{W1}, A_{W2}) are summed together and divided by the A_T to obtain this information. For a fixed beam energy, the implanted positrons will follow a Makhovian profile, where later diffusion occurs. The S parameter can be expressed as,

$$S_n(E) = f_{surf}(E)S_{surf} + f_{bulk}(E)S_{bulk} + \sum_i f_{def-i}(E)S_{def-i}, \tag{2.8}$$

where S_{surf}, S_{bulk} and S_{def-i} are the individual S-parameters at the surface, in the bulk and within defects respectively. The $f_{surf,bulk,def-i}$ are the probabilities at each annihilation region described by the followig equations:

$$f_{surf} = D_+[\frac{dn(z,E)}{dz}]_{z=0}, \tag{2.9}$$

$$f_{bulk} = \lambda_b \int_0^\infty n(z,E)dx, \tag{2.10}$$

$$f_{def-i} = \nu_i \int_0^\infty C(z)_{v-i} n(z,E)dz, \tag{2.11}$$

where D_+ described the annihilation coefficient, $C(z)_{v-i}$ signifies the i defect concentration, λ_b the annihilation rate at the bulk and ν_i the coefficient for trapping in the material. These three probabilities need to be normalised to 1.

Obtaining useful information from these parameters is done via a program well-known in the positron annihilation community, VEPFIT [42]. Utilizing the information from the S-parameter with this program it is possible to extract information on the characteristics of single or multi-layered materials (like porous structures, boundaries and the positron diffusion length L_+).

Considering all possible annihilation channels, the overall S and W parameters are given by:

$$S = \frac{\sum_i f_i S_i}{\sum_i f_i}, \tag{2.12}$$

$$W = \frac{\sum_i f_i W_i}{\sum_i f_i}. \tag{2.13}$$

A difference in the experimentation is the use of two detectors in coincidence (CDB), shown in Fig. 2.6 These two detectors increases the energy resolution to a factor of $\sqrt{2}$

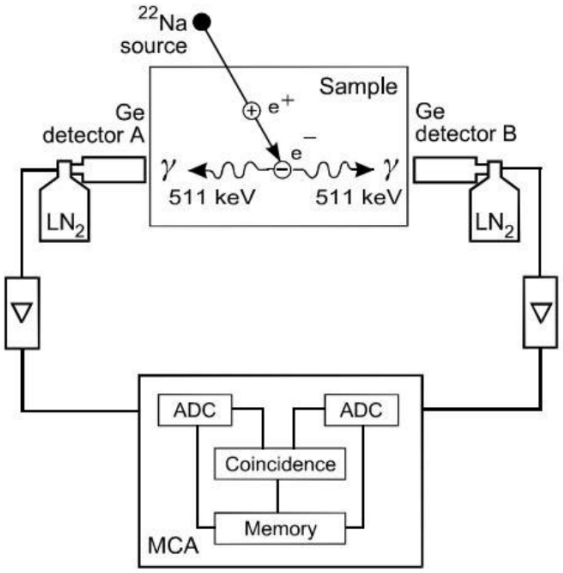

Figure 2.6: Schematic of the set-up of Coincidence positron Doppler Broadening [6].

and reduces background noise from two orders of magnitude with respect to the measurements with one detector [43].

Positronium Fraction

Similar to the experimental lay-out for obtaining the S and W parameters from the previous subsection, it is possible to gain an insight on the o-Ps formation properties of the target material.

The way of determining the quantity of Ps produced within a certain material is called the $3-\gamma$ method [44]. Due to the different annihilating properties between o-Ps and p-Ps, the annihilation spectra created from the positron/positronium annihilating within a material, produces two key features, the valley and peak region, shown in Fig. 2.7. Following Ref. [44] the peak can be described by,

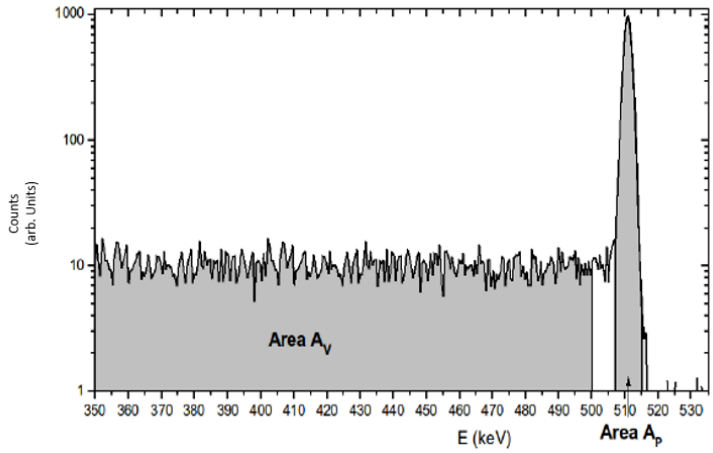

Figure 2.7: The annihilation spectrum indicating both the area of the valley (350-500 keV) and area of the peak (511$\pm$4.25 keV) needed for $F_{3\gamma}$ calculation.

$$P = P_0 + F_{3\gamma}(P_1 - P_0), \tag{2.14}$$

where $F_{3\gamma}$ is the positronium fraction, P_0 is the area of the peak when 0% Ps is formed and P_1 in the area for 100% Ps. Instead, the valley is described by,

$$V = V_0 + F_{3\gamma}(V_1 - V_0), \tag{2.15}$$

where V_0 and V_1 indicate 0% and 100% respectively in the valley. These can be combined to form a relationship shown as,

$$R = \frac{V}{P}. \tag{2.16}$$

From the relationship the Ps fraction $F_{3\gamma}$ can be determined as,

$$F_{3\gamma} = \left[1 + \frac{P_1}{P_0}\frac{R_1 - R}{R - R_0}\right]^{-1}, \tag{2.17}$$

where R_0, P_0 and R_0, P_1 are the parameters for 0% (F_0) and 100% (F_1) positronium fractions respectively.

To obtain the experimental parameters for this equation to work, the 100% and 0% Ps formation yields need to be taken to calibrate the system. A Ge single crystal [100] is used for this. To obtain $\approx 100\%$ Ps, a target of germanium is heated to 1000 K where in this environment, all positrons form positronium (at zero implantation energy) R_1. R_0 is taken at 0% as mentioned, done by using the highest implantation energy within the Ge [45].

To understand further about the o-Ps, the pick-off effect needs to be included into this equation. This offers a reduction of probability for 3_γ annihilation to a fraction of,

$$\epsilon = \frac{\lambda_{3\gamma}}{\lambda_{3\gamma} + \lambda_{p.o.}}, \tag{2.18}$$

where $\lambda_{3\gamma}$ and $\lambda_{p.o.}$ are the annihilation rate in the pores/cavities and the pick-off annihilation rate respectively. The values for these are obtained through positron lifetime measurement. So combining these equations accurately describes the o-Ps fraction by,

$$F(E) = \frac{3}{4}\frac{1}{\epsilon}F_{3\gamma}(E). \tag{2.19}$$

2.3 Energy tunable Positron and Positronium Annihilation Lifetime Spectroscopy (PPALS)

A new addition to the Como VEPAS laboratory is an upgrade to the slow positron beam to allow tunable energy Positron and Positronium Annihilation Lifetime Spectroscopy (PPALS) measurements to be conducted. The setup is based on a similar system that works with a magnetically guided positron beam [46]. In the present case, the beam is totally guided by an electrostatic system. Positrons pass through the center of a holed microchannel plate (MCP, see Fig. 2.8) placed along the beam axis and then are implanted within the target material. The implantation process emits secondary electrons into vacuum [47] which are then detected by the MCP. This in-turn creats the Start signal for the spectrometer. The Stop signal is generated, as with the conventional lifetime spectrometers, i.e. by the gamma rays of the positron-electron or Ps annihilation.

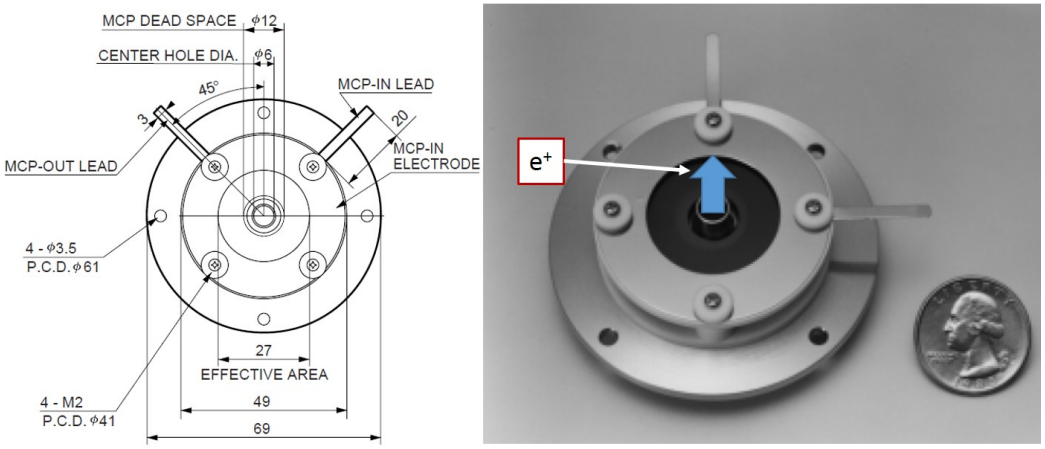

Figure 2.8: Holed MCP used in the lifetime setup to collect the start signal. On the left panel the dimension units are in millimeters.

A scheme of the system is shown in Fig. 2.9: i) the Start signal is generated by means of a fast signal of secondary electrons using a holed MCP (Hamamatsu, model: F4294-09, rise time of 330 ps and FWHM of 600 ps) ii) the MCP signal goes into a constant fraction discrimator (CFD) to limit the range of the signal and reduce the noise and to deliver a read-

able pulse from the time amplitude converter (TAC) iii) the TAC waits for the annihilation Stop signal iv) the produced gamma ray is detected by a gamma ray detector consisting of a BaF_2 scintillator crystals of $1.5'' \times 1$ cm mounted on two XP2020 photomultiplier (PMT) coupled with Ortec 269 bases v) the PMT pulse goes through a CFD and a delay line vi) the TAC reads the Stop signal and deliver an unipolar pulse, proportional to the Start/Stop input time difference, to the multi-channel analyzer (MCA).

To increase the count rate the measurements were performed by means of two fast-fast lifetime spectrometers working in parallel as shown in Fig. 2.9. The peak to background rate was 10^4, the conversion of 93.5 ps/CHN and a time resolution of 2 ns, mainly due to the time of flight of the secondary electrons. For each implantation energy the total area under the spectra were about 10^6 counts on 8192 channels.

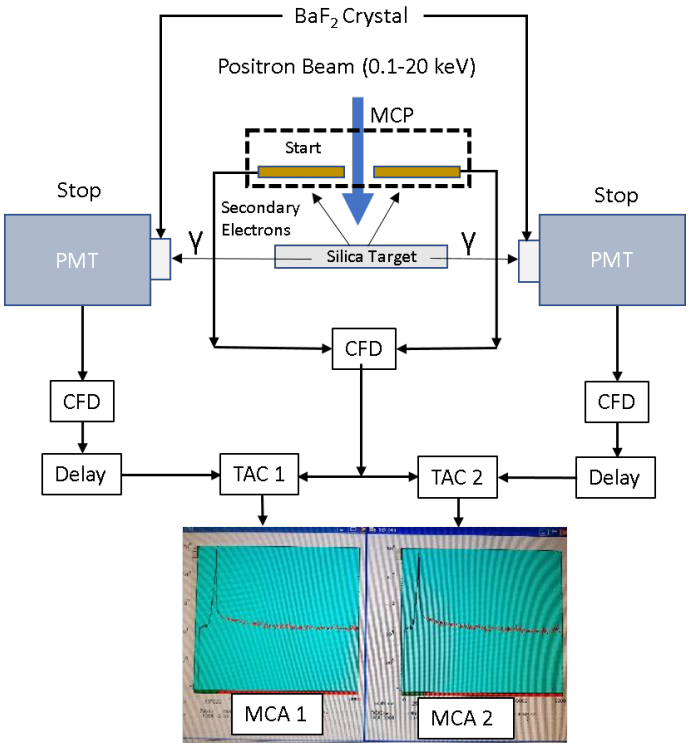

Figure 2.9: Scheme of the PPALS system implemented to the present work at the Como lab (LNESS).

CHAPTER 3
ANTIMATTER COLLABORATIONS

Two experiments will be discussed within this chapter, AEgIS and QuPLAS, where the Como positron group of Politecnico di Milano is an active collaborator. The main contributions produced by this group are in regards to the development and characterization of new positron to positronium converters for both experiments. Six months of this PhD was spent at CERN for antiproton trapping and manipulation experiments.

3.1 Introduction and historic remarks

As detailed in Chapter 1, the existance of the positron was theorized by Dirac [1] and experimentally observed by Anderson [2] in 1928 and 1932 respectively. These discoveries, opened the understanding that other particles may have their very own antiparticle. In Paul Dirac's Nobel prize speech in 1933, he predicted the existance of further antiparticles and inparticular, the antiproton. But, the discovery of this antiparticle needed a different type of experimental apparatus, a particle accelerator. At that time, accelerators were in the very early stages of development. In 1954, the Bevatron based at the Lawrence Berkeley National Laboratory began operation. This particle accelerator was able to give high kinetic energies to the protons to several GeV and directed towards a fixed metallic target. A year later, antiprotons were experimentally observed by a team led by Emilio Segré and Owen Chamberlain. These antiprotons were formed via pair production [48]. This led to the Nobel prize being awarded jointly to these two researchers. In 1956 under a separate team led by Burce Cork, also at the Bevatron, were able to observe the antineutron [49].

A natural consequence of the existence of the positron, antiproton and antineutron was the theory that also antiatoms could be formed. Antideuterion was produced in 1965 by two separate facilities, the proton synchrotron at CERN by A. Zichichi et al. [50] and at

the Brookhaven National Laboratory by L. Lederman et al. [51]. This antiatom consists of an antiproton and an antineutron. This discovery laid the foundation for the creation of antiatomic systems, in particular the simplest antimatter atom, the antihydrogen atom $\overline{H}$. This antiatom would consist of an antiproton with a positron in its orbit. The Low Energy Antiproton Ring (LEAR) based at CERN, was utilized to obtain low energy antiprotons to be used for subsequent antihydrogen formation. These atoms were first produced by G. Bauer et al. [52] by directing the antiprotons towards a Xe gas. Interactions with these atoms produced antihydrogen at energy levels ($\approx$GeV) with speeds close to the speed of light and in low quantities. Further research with the low quantities of high energy antiatoms was deemed to be impossible and a new method was needed as a means of production.

In 1997, CERN approved a new facility for slow antiproton production named the Antiproton Decelerator (AD) [53]. This would provide antiprotons for the next generation of antimatter experiments, lower energy antiprotons ($\approx$5 MeV) in much higher quantities (10^7) in 200 ns bunches. The access to lower energy antiprotons opened the possibility of cold antihydrogen production. The ATHENA experiment [54] was the first to produce antihydrogen via the mixing of antiprotons and positrons in a nested trap, initiating a three body recombination process. This method allowed the production of antihydrogen at cool temperatures ($\approx$100 K)This was closely followed by the ATRAP experiment [55]. The current direction of antimatter research is to see if there are any asymmetry properties between antihydrogen and hydrogen. One particular property of high interest is the effect of Earth's gravitational acceleration on antihydrogen.

3.1.1 The Antimatter Factory

This section at CERN is called "The Antimatter Factory" and home of the AD, which houses a number of experiments which receive low energy antiprotons. These antiprotons are created from high energy protons accelerated by the Proton Synchnotron (PS) [53]. The

AD is the only current facility that produces antiprotons at low energies and the home of low energy antihydrogen and antiprotonic helium production [56].

Current experiments receiving antiprotons are of the ALPHA (Anthydrogen Laser PHysics Apparatus), AEgIS (Antimatter Experiment: gravity Interferometry Spectroscopy), ASACUSA (Atomc Spectroscopy And Collisions Using Slow Antiparticles), ATRAP (Antihydrogen TRAP), BASE (Baryon Antibaryon Symmetry Experiment) and a new addition to the AD, GBAR (Gravitatonal Behaviour of Antihydrogen at Rest) soon to be installed. A new decelerating ring is currently in construction to decelerate antiprotons further called ELENA (Extra Low ENergy Antiprotons) [57] to around 0.1 MeV, which is expected to be fully operational in 2020.

Antiproton Decelerator

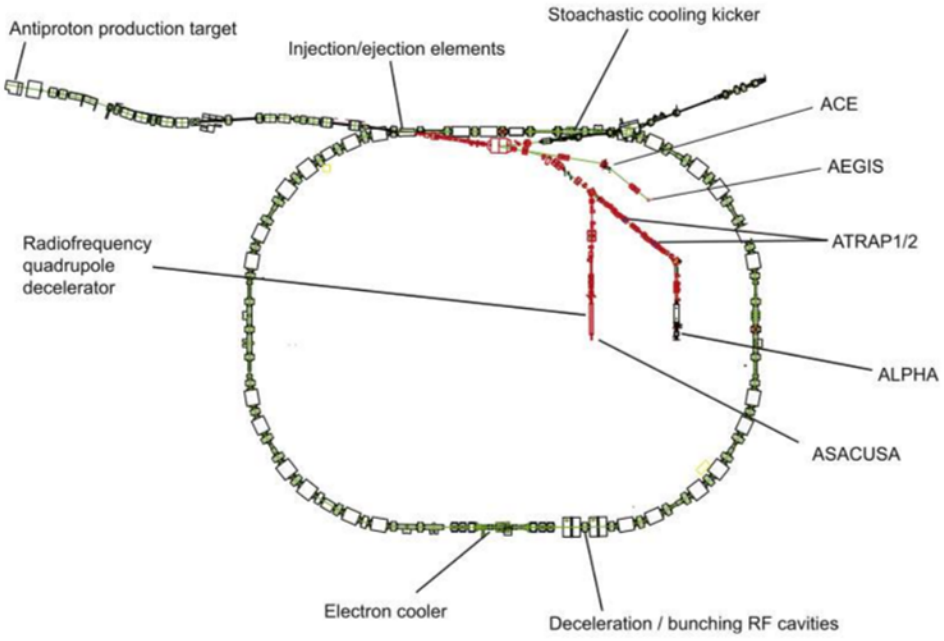

Figure 3.1: Schematic of the Antiproton Decelerator including current experiment locations [58]

The decelerating ring consists of an oval-like ring 182 m in circumference [53], shown

in Fig. 3.1. As mentioned in the previous section, PS accelerated protons hits a target (Iridium). Pair production reaction occurs and emits antiprotons in the opposing surface of the block. The process is shown as,

$$p_{beam} + p_{Target} \rightarrow p + p + p + \overline{p}. \tag{3.1}$$

The initial protons are accelerated by the PS to energies around 26 GeV before hitting the target. This energy is much higher than the E threshold for the reaction (E≈6 GeV) and allows a higher efficiency of $\overline{p}$ production ($\approx 10^{-6}$). Around 5×10^7 $\overline{p}$ are produced and injected into the AD region with initial momenta of ≈3.6 GeV/c. The momenta sread is around 6% with a transverse emittance of $\epsilon \approx 200$ π mm mrad. The AD functions in a cyclic mode with a time duration of ≈100 s. With these $\overline{p}$ injected into the deceleration ring, three cooling processes are put into effect.

(1) Cooling is undertaken within the radio frequency (RF) cavities via RF bunch rotation where the bunch pulse is stretched preserving the longitudinal emittance. The spread of momentum is reduced during this process. (2) Stochastic cooling and deceleration is induced across the ring by the steering electrodes. The momenta and transverse position of the antiprotons are detected and these electrodes are pulsed in respect to these positions, reducing the energies to around 2 GeV. (3) Electron cooling is utilized for further reduction of the momenta to around 100 MeV/c through the Coulombian mechanism. This is a very efficient cooling process reducing energies down to around 5.3 MeV. All these cooling steps are visually shown in Fig. 3.2

3.2 AEgIS

This section is dedicated to the Antihydrogen Experiment: Gravity Interferometry Spectroscopy (AEgIS) collaboration where the Como group contributes to the progression to the creation of antihydrogen $\overline{H}$ via charge exchange [59, 60]. They plan to measure the ef-

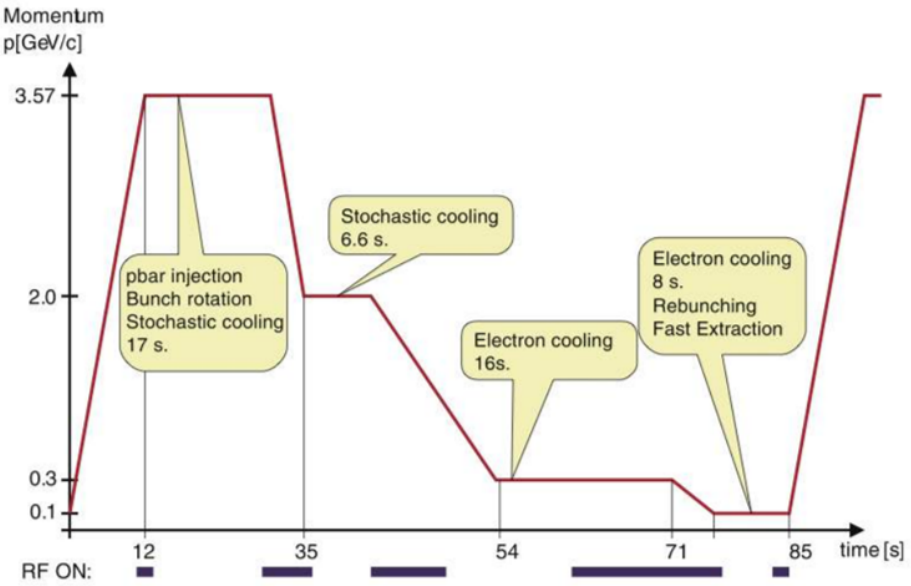

Figure 3.2: Antiproton Decelerator cooling cycle. The $\bar{p}$ energies are shown over time. The lower energy part demonstrates the stochastic and electron cooling [58]

fect of the Earth's gravitational field on a beam of $\overline{H}$. Main achievements in the form of the laser excitation and positronium transmission production will be detailed in this section.

3.2.1 Experimental Aim

Matter and its counterpart Antimatter, are two observables in our universe where the latter has an unexplained absence in comparison to the former. The reason for this is still an unsolved puzzle and is currently being explored by CERN based experiments at the antimatter factory facility. An interest to many antimatter physicists is to find any asymmetries between the two, in the form of hydrogen and antihydrogen. The central Quantum Field theory (QFT) for describing the properties of matter and antimatter is with the CPT (Charge conjugation, Parity, Time reversal) theorem [3]. Mass, momentum, energy and spin is determined to remain unchanged under this theorem whilst the remaining additive quantum numbers (baryon number, charge, etc.) invert. A subject of high interest for many experiments is the observation of the effect of gravity on antimatter. As gravity is described as

a geometric property of space-time within general relativity, it has not yet been included successfully in QFT, so this remains undescribed within the CPT theorem. This would be also the first observation of the Weak Equivalence Principle (WEP) with neutral antimatter and a possible lead to a QFT which includes gravity [61]. The effect of a gravitational field on a system (described with WEP) does not depend on its composition or structure [62]. With regular matter, WEP has been tested within 10^{-13} [63]. For the charged antiparticle trapping (e.g. antiprotons and positrons), Penning traps [64] are used which implement a combination of electric and magnetic fields to confine them.

Stray residual electric and magnetic fields [65] produced from these forms of trap make it impossible to perform gravitational observation with these particles. The ATHENA experiment created low-energy antihydrogen $\overline{H}$ in 2002 [54]. They formed this neutral antiatom by implementing the three-body reaction by the mixing of low energy trapped antiprotons ($\overline{p}$) and positrons (e^+). Due to the stray fields mentioned previously only affecting charged matter, this opened the possibility to test WEP on neutral atoms of antihydrogen. The ALPHA collaboration performed a preliminary measurement of the Earths gravitational effect on magnetically trapped $\overline{H}$. As a result, the gravitational acceleration of $\overline{H}$ was constrained to within $\approx$100 times the g value for matter [66].

In 2007, The AEgIS collaboration [59, 60] proposed an experiment to measure the effect of gravitational field on $\overline{H}$ atoms to 1% accuracy. This would include the design of a cold $\overline{H}$ beam (the concept is shown in Fig. 3.3). Rydberg-state antihydrogen $\overline{H}^*$ will be produced via a charge exchange process [67] by introducing cold trapped $\overline{p}$ to cold, Rydberg-state positronium (Ps^*). Ps^* is the bound state of an electron e^- and a e^+ laser excited to Rydberg levels to increase the principal quantum number n and its lifetime [67]. The charge exchange reaction described as [67, 68],

$$Ps^* + \overline{p} \rightarrow \overline{H}^* + e^-, \tag{3.2}$$

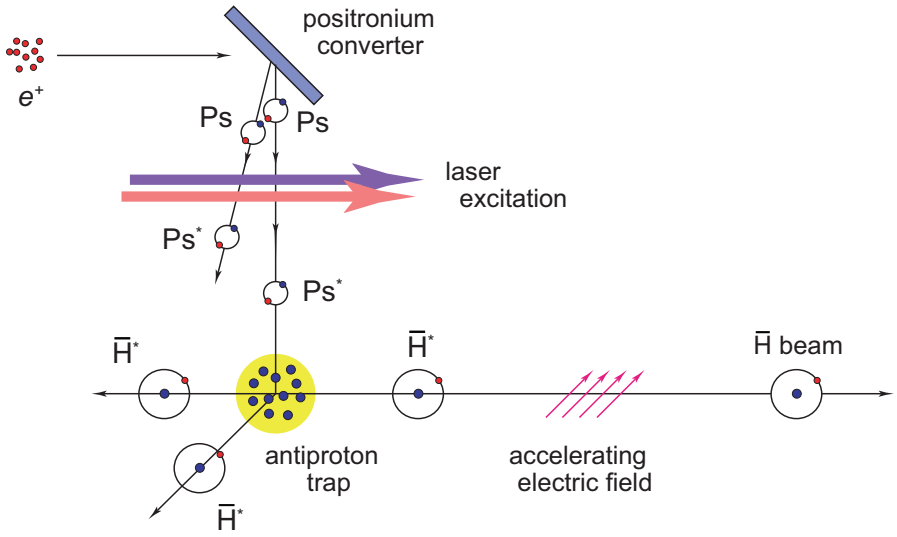

Figure 3.3: Antihydrogen formation process using the charge exchange reaction between Ps and cold $\overline{p}$.

The benefit of $\overline{H}^*$ for the creation of the proposed beam is that the electric dipole moment is large, allowing Stark acceleration to occur, and thus to direct the particles forming the beam [69]. The $\overline{H}^*$ needs to decay to its ground state to allow any accurate gravitational measurementto take place. It is predicted that the ground-state should be reached prior to the entering of the gravity measurement region. It is important to have ground-state antihydrogen to remove the effect of the Stark fields used previously for the initial acceleration. The Stark fields will no longer affect the antihydrogen in flight when it reaches the ground-state. Rydberg state Ps also benefits the charge exchange process. The formation cross-section for this process increases to the fourth power of the Ps principal quantum number comaring to ground-state Ps. [67, 68].

3.2.2 AEgIS Apparatus

The AEgIS apparatus, shown in Fig. 3.4, utilizes two superconducting magnets, one 5 T and one 1 T magnet. These respectively surround the initial antiproton trapping and the $\overline{H}$ formation regions which are used to radial confinement of the charged anti-particles. A series of cylindrical electrodes inside each magnet form a Penning-Malmberg trap ar-

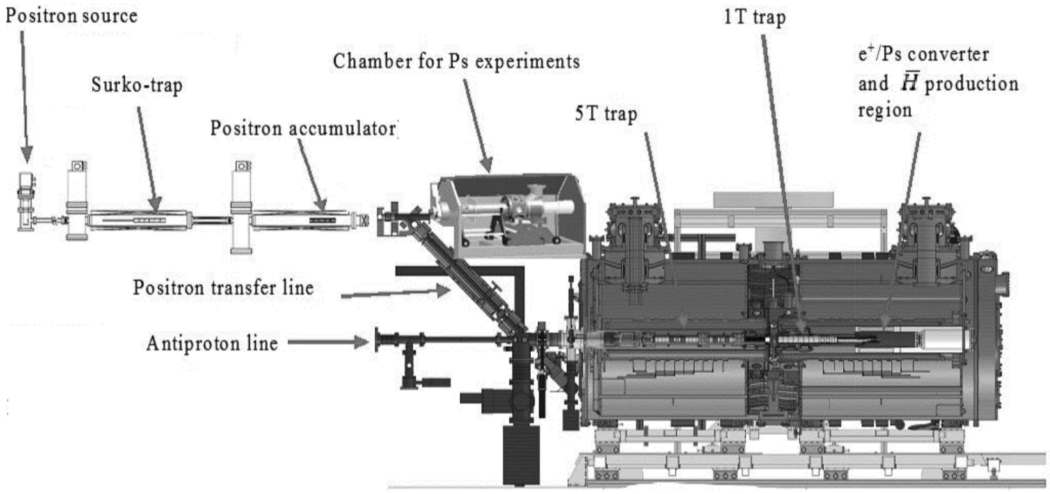

Figure 3.4: The experimental setup scheme of the AEgIS experiment. The positron beam and test chamber on the upper left area are presented in more detail in Fig. 3.7. This image excludes the moiré deflectometer (presented later in Fig 3.5 and Fig 3.6).

rangement [64], used for axial confinement. A bunch of 3×10^7 $\overline{p}$ with kinetic energies around 5 MeV initially are delivered from the AD and pass through a set of aluminium foils (degraders) to reduce the incoming $\overline{p}$ energy to a few keV. High voltage electrodes within the 5 T have the capability of trapping a fraction of the decelerated $\overline{p}$. These antiprotons are then electron cooled [70] by the interactions with a previously stored e^- plasma. $\overline{p}$ are cooled down to a few kelvin. Once the cooling preocess is complete, the removal of the e^- is needed (undertaken with a voltage kick) leaving only the antiprotons within the trap. The $\overline{p}$ are then transferred to the 1 T region.

For the gravitational test, the beam will pass through a classical moiré deflectometer made up of two gratings and a position sensitive detector [71], as shown conceptually in Fig. 3.5. The deflectometer fringes are subject to an expected vertical shift h, caused by the gravitational effect affecting the incoming pulses of $\overline{H}$ during flight, described as

$$h = g_h \left(\frac{L}{v} \right)^2 , \tag{3.3}$$

where L is the distance between the first and the second grating (which is also the same

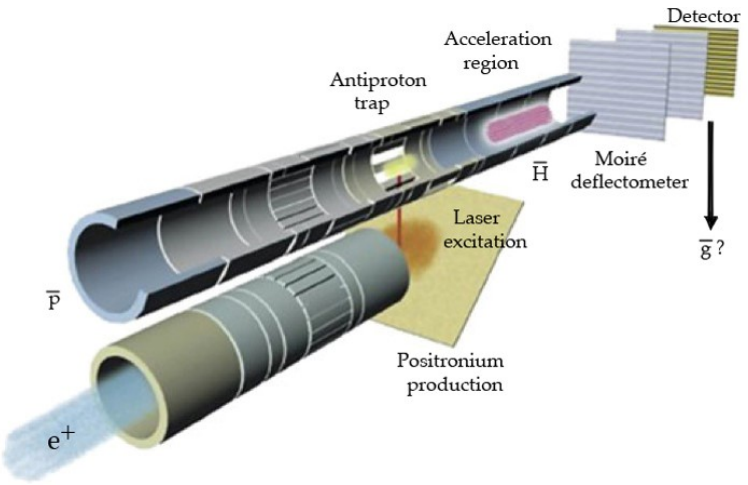

Figure 3.5: 3D view of the antihydrogen formation region (not to scale).

value for the distance between the second grating and the detector), g_h is the gravitational acceleration experienced on $\overline{H}$, and v is the perpendicular velocity of the $\overline{H}$ after the Stark acceleration before the moiré deflectometer. Differing velocities v will be implemented to extract the g_h value [72]. Figure 3.6 shows the concept of the deflectometer. A small-scale prototype of the deflectometer has already been tested with antiprotons [73].

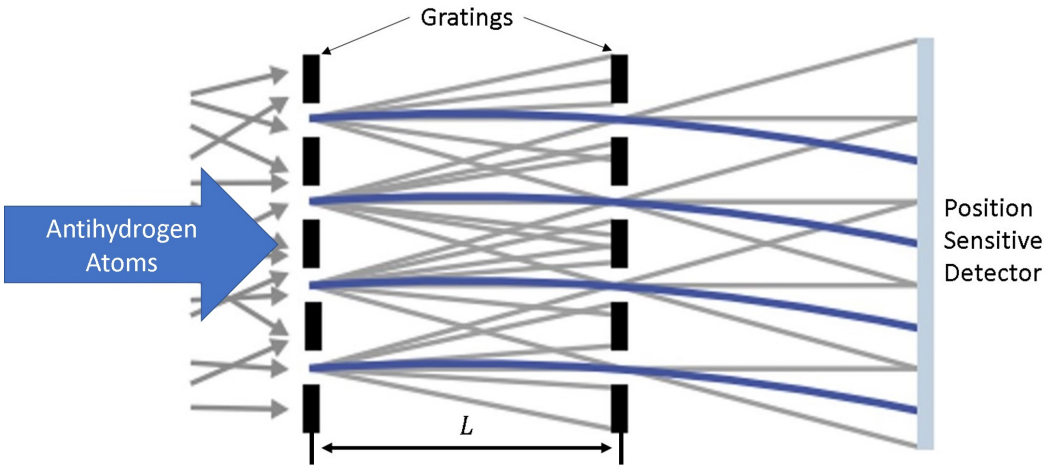

Figure 3.6: Sketch of the moiré deflectometer showing the antiprotons passing through the two gratings then hitting the position sensitive detector. The dark blue line indicates the expected/predicted downward shift caused by the gravitational force of the Earth. In the measurement of Ref. [71], the position sensitive detector was in the form of an emulsion detector [74].

3.2.3 Positron System

Positron Moderation and Trapping

The source of positrons used is of the same radioactive isotope in section 1.1, but with a different type of moderator. The ^{22}Na source is surrounded by a metallic cone structure, which is coupled with a cryogenic unit "cold head". This unit is designed to keep the area down to 7 K; at these temperatures neon is able to be deposited and freeze onto the conical wall. The moderator efficiency for neon is around 1% with a mean positron energy of 2 eV. The spread of these energies are approximately 1 eV. The moderated positron are first extracted via a drift tube towards a $E \times B$ filter. This allows seperation of the moderated and unmoderated components of the beam, where the unmoderated positrons remain uneffected by the combined fields and subsequently annihilate within this region. The redirected moderated positrons then enter a three stage Surko trap, consisting of an electrode arrangement with 3 sections of increasing diameter, this is within the region labelled Surko-trap in Fig. 3.7. An initial buffer gas (N_2) is administered into this system to allow initial cooling of the incoming positrons via collisions with the gas particles. This was optimized to allow sufficient cooling with only a single pass to allow high trapping efficiency, obtained by using a high pressure of gas in the first stage region of N_2 (10^{-3} mbar). Due to the changes in diameter in the upcoming sections, this naturally decreases the pressure of nitrogen as the diameter increases, in the other two-stages, the pressures would become 10^{-4} and 5×10^{-6} mbar respectively. At the final stage of the trap section, a lower potential well applied to allow the cooled positrons to be confined. Reducing the quantity of N_2 and the base pressure decreases the annihilation rate of each pulse within the system, which in turn allows multiple pulses of positrons to be gathered. These positrons are then compressed radially with use of a segmented electrode assembly called a rotating wall electrode (frequencies used 5-6 MHz). It has been determined that the positrons cooled and confined in the potential well experience a lifetime of around 2 s. Fig. 3.7 shows the whole positron system

schematically.

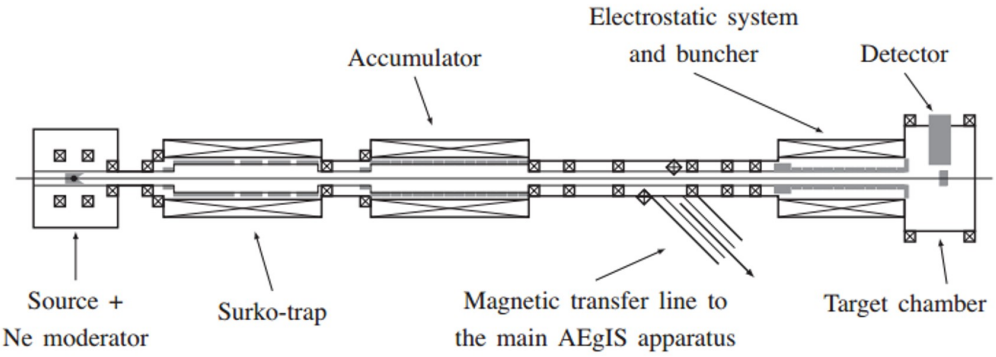

Figure 3.7: Side view of the positron accumulation setup, including the Ps test chamber at the far right. (Image from Ref. [75]).

Positron Accumulator

The cooled positron are then accumulated from the trap region to the accumulator (see Fig. 3.7) of the positron system where many positron pulses are stored at a low base pressure ($\approx 10^{-10}$ mbar) allowing storage times on the order of several hundred seconds. The magnetic field is produced with a solenoidal magnet located across the length of the Surko trap. The magnetic field strength of 0.1 T allows radial confinement of the positrons. The 23 cm length electrode stack, made up of 1.27 cm radius electrodes (23 in total), allows longitudinal confinement and accumulation of positrons. The potential well produced with these traps has a depth of 14 V. In this region, a small quantity of N_2 is allowed to leak to here from the trap region as well as a cooling gas which feature lower annihilation rates with positrons (e.g. CO_2, SF_6 etc.). This allows further cooling for the positrons as they trap within this electrode assembly potentials, and to decrease the annihilation rate with the cooled positrons and the gas, allowing accumulation to occur.

For the detection of the annihilation gamma rays as the positrons are directed to a material, a CsI Scintillating crystal coupled with a photodiode is useful. The crystal converts the gamma rays hitting the crystal into light which is then detected via the photo diode (similar to detectors mentioned in Chapter 2). Under current conditions, around 8×10^7 positrons

can be stored over a 450 s period (≈300 pulses). These numbers were met when the main apparatus magnets were not in use. Strong stray magnetic fields from these magnets affect the maximum numbers possible to be stored.

To use the stored positrons within the trap, these need to be released axially to allow the transportation of the plasma. This is done with use of specialised electronics connected to the end electrodes which creates an axial voltage ramp, opening the trap (lowering the potential wall) and pushing the particles out by increasing the electrodes located at the rear of the plasma. This act is done simultaneously (in a wave-like motion).

Positron Testing Chamber

There are two directions where the ejected positrons can be directed, downwards towards the main apparatus, and to the Ps test chamber located linear to the positron system. This dedicated section is for the studies of Ps formation and excitation. Within the testing area, the sample is placed on a moveable holder allowing changes of geometry and direction of Ps emission. Before the positrons enter the sample, they are compressed and accelerated by means of a buncher placed between the end of the accumulator and the testing chamber. The buncher is also used to give the positron kinetic energy needed for efficient Ps formation (usually around a few keV). SSPALS is the main technique for the detection of Ps generated within the system at CERN. This incorporates a PbWO4 crystal ($25\times25\times20$ mm^3) coupled to a Hamamatsu R11265-100 PMT for the production of the spectra containing information of the production and emission of Ps from the target. The whole chamber is schematically shown in Fig. 3.8.

Positron Transfer Line

To introduce the accumulated positron pulse into the main apparatus, a transfer line is used. This line connects the positron system to the experiment via a 45° tube. Magnetic correction coils are utilized to divert the positrons during flight to follow down the 2.5 m

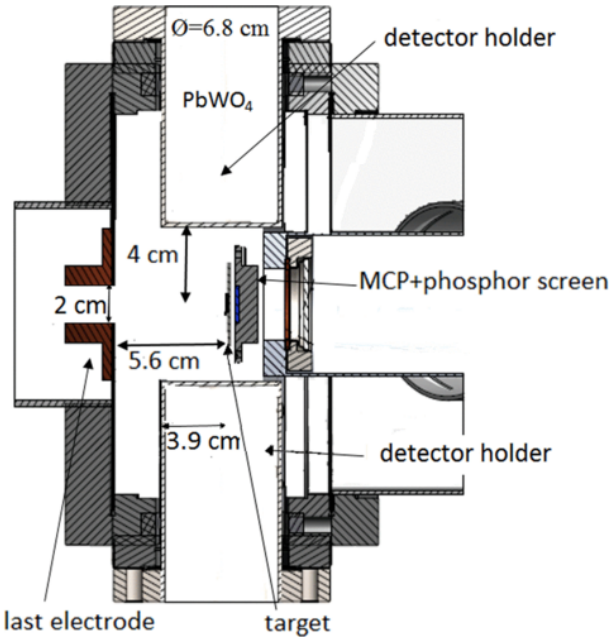

Figure 3.8: The Ps testing chamber (Ref. [76]).

line. These coils have a magnetic field strength range of 0.05-0.25 T.

3.2.4 Antiproton System

For the trapping and manipulation of antiprotons, a Penning Malmberg trap is implemented. The antiproton trap sections are: the C-trap and P-trap both located within the 5T region. The inner diameter of the trap electrodes are 30 mm in diameter across a 1 m distance (102 electrodes in total). Both traps can be controlled separately or together to explore new ways of manipulating antiproton plasma to find the best conditions before transfer into the antihydrogen formation region. Both traps have two sets of segmented electrodes which allows rotating wall (RW) compression of the plasma trapped within. The RW drive is produced by inducing a sinusoidal voltage signal with a 90 degree shift for each segment. The voltage as a function of time (t) can be described as,

$$V(t) = A_{RW} sin(\omega_{RW} t + \phi), \tag{3.4}$$

where ω_{RW} is the rotating wall drive frequency, A_{RW} is the rotating wall amplitude and ϕ is the phase shift. F_{RW} is the rotating wall frequency and described as,

$$F_{RW} = \frac{\omega_{RW}}{2\pi}. \tag{3.5}$$

This frequency is shifted by 90° (ϕ) for each rotating wall segment which creates a rotating dipolar radial field. For the AEgIS apparatus, the regular operating parameters for RW compression lie in the range of 300-400 kHz(F_{RW}) and 2-3V (ω_{RW}).

The magnetic field similar to the positron system as mentioned in section (3.4.1) allows radial confinement. Standard operation includes cooling of the antiprotons with use of preloaded electrons ($\approx 4 \times 10^8$) accross the trap. The RW electrodes are also used to manipulate the electron plasma to a radius of ≈1.5 mm prior to mixing with the antiprotons. The 5 MeV antiprotons produced from the AD needs their energy to be reduced further before catching can be possible. A beam counter (53 micrometer thick Si) and an Aluminium degrader (173.7 μm thick) are located prior to the electrode arrangement, decreasing the energies of a fraction of the incoming antiprotons to ranges around 0-100 keV (where a fraction is trapped by the HV electrodes set to 9 kV). The standard method of catching is having an end cap HV electrode up allowing the degraded antiprotons to be stopped. To avoid the antiprotons from escaping a secondary HV electrode is raised completing the axial confinement of the charged species (located at the beginning of the trap) with a short raise time of a few ns. The catching efficiency is around 1.25% from the received bunch (3×10^7) from the AD. The cooling of the electrons within the trap is done from the cyclotron radiation process induced by the high magnetic field.

Uncooled antiprotons (hot) are removed from the trap and towards the degrader for diagnostics using scintilators, this detects the annihilation products as they hit the degraders surface. This allows understanding on the cooling efficiencies of the antiprotons. The cooled antiprotons remain in the potential well.

Current trapping conditions allow $50\% - 60\%$ cooling efficiencies of around 2×10^5 antiprotons. The electrons are then removed using a 80 ns pulse of the end electrode, this pulse is fast enough to disallow any antiprotons from exitting as they have a slower velocity in comparison. The shape diagnostics are determined with use of a MCP coupled with a phosphor screen located at the end of the experiment. So, when the potential wall is lowered, the antiprotons travel towards the MCP surface, producing secondary electrons which interact with the phosphor screen, creating light able to be detected with a CCD camera.

The main reason of the RW compression is to reduce the plasma radius small enough to enter the final trapping region, the antihydrogen formation region where the electrode stack diameter is of 10 mm. Once transferred within this trapping section (U-trap), the antiprotons rest and wait for the incoming Ps through an open region shown in figure 3.5, in turn creating antihydrogen via charge exchange [59].

Laser System

With the aim to increase the Ps lifetime long enough to successfully perform the charge exchange reaction, laser excitation to Rydberg states is required. To accomplish this, two laser pulses are used for the initial excitation to the n=3 state and then to the Rydberg levels with the secondary. This needs to be timed to the moment o-Ps atoms make their way out of the positron/positronium converter and emitted into vacuum. The laser light source is provided by a 1064 nm Nd:YAG laser coupled with a harmonic generator that produces the original 1064 wavelength and that of the second harmonic (552 nm) and the fourth harmonic (266 nm). As shown in Fig. 3.9 you can see that these separate beams need to be combined to get to the wavelengths needed.

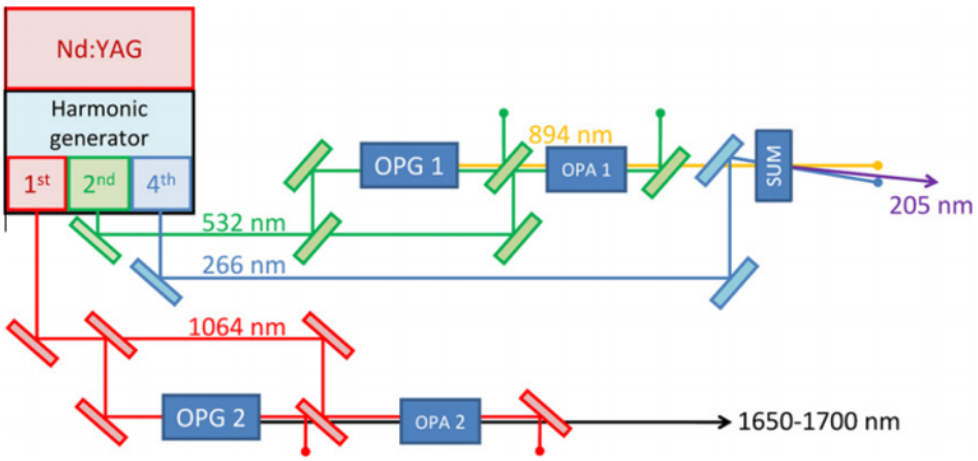

Figure 3.9: Laser system for the Rydberg excitation of Ps from Ref. [77]) The OPG (Optical Parametric Generator) and OPA (Optical Parametric Amplifier) are non-linear crystals.

3.2.5 Positronium Production

To obtain Ps for the charge exchange process, a reflection positronium target is implemented. This target features perpendicular nanochannels created via the electrochemical etching of Si via HF solution. The silicon naturally oxidises in air which leaves a layer of silica around the edges of the etched channels. Once oxidized the diameter became between 5-8 nm with 2 μm depth. Positrons at high energies scatter in the bulk of the target and a fraction of these form Ps. Then a fraction of these Ps atoms are emitted into vacuum. Prior to emission, Ps thermalizes via collisions with the nanochannels. Due to the pick-off process (mentioned in Chapter 1) the positron within the Ps atom can annihilate with an additional electron within the material, causing losses. From this process and the fact that p-Ps cannot be emitted due to the short lifetime (unable to complete thermalization process) cold o-Ps is emitted into vacuum. This is only one type of reflection target currently available. Other groups are also finding ways of improving the production of cold Ps running tests with different tyes of silica materials (e.g. Aerogel [12], etc.).

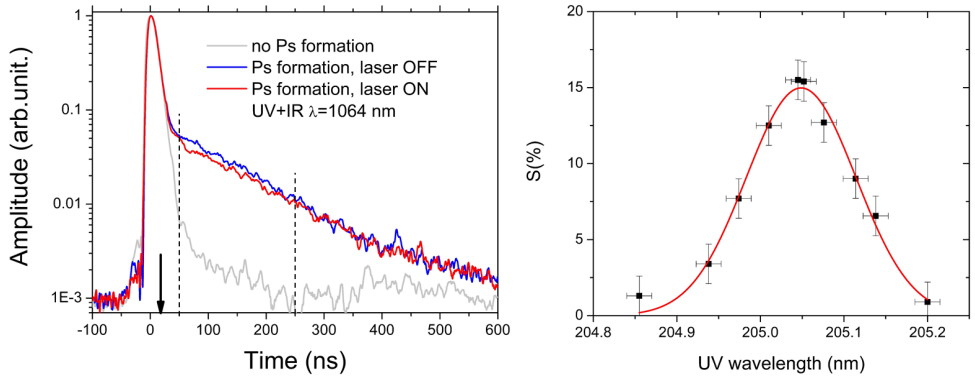

Figure 3.10: SSPALS measurement (left) containing 3 lifetime spectra. Light gray (background), Ps emitted into vacuum with laser OFF (blue) and with the UV+IR lasers ON (205.05 + 1064 nm) (red). The 50 to 250 ns region indicated by the vertical dashed lines was used to determine the S parameter (see Eq. (3)) for n = 3 (right). This graph illustrates the Ps excitation efficiency as a function of the UV laser wavelength (both images from Ref. [76]).

3.2.6 Positronium Laser Excitation

Two Positronium (Ps) states can be formed: the singlet state (Para-Positronium p-Ps) and the triplet state (ortho-positronium o-Ps). When formed in vacuum, all states of Ps annihilate into gamma rays having a total energy equal to the rest mass of both the electron and positron. What differs is the lifetime and the quantity of gamma rays produced. When p-Ps annihilates in vacuum, mainly two gamma rays are produced with a mean lifetime of 125 ps. Instead, when o-Ps annihilates in vacuum, mainly three gamma rays are emitted with a mean lifetime of 142 ns. The lifetime of o-Ps is long enough to perform laser excitation to increase its life prior to annihilation [78].

Recently performed by the AEgIS collaboration, Ps was laser excited to the n=3 state for the first time. A laser pulse was used with a wavelength around 205 nm to first reach the n=3 state, then a secondary laser pulse (1064 nm) was used to simultaneously photoionize the excited Ps [76]. The Ps test chamber housed the excitation lasers with the reflective target placed at the centre. Positron bunches of 20 ns of 3×10^7 positrons were focused onto the target and accelerated to a kinetic energy of 3.3 keV. o-Ps is then emitted into vacuum after the initial Ps formation process. The o-Ps in vacuum was detected via a

20x25x25 mm^3 $PbWO_4$ scintillator coupled with a Hamamatsu R11265-100 PMT (Photo Multiplier Tube). The single shot positron annihilation lifetime spectroscopy (SSPALS) method [79] was implemented to produce the Ps lifetime spectra through the detection of the annihilating gamma rays, as shown in Fig. 3.10.

A difference in the lifetime spectra can be seen between laser on and off within the space located within the two dashed vertical lines. The decrease observed inside this allocated region indicated an elongation of the o-Ps lifetime, directly caused by the laser excitation. With this alteration in the spectra, it was possible to obtain the o-Ps excitation efficiency from the S parameter defined here as,

$$S = (f_{off} - f_{on})/f_{off}, \tag{3.6}$$

where f_{on} and f_{off} are the areas within the allocated region in the spectra (dashed line), shown in the left image of Fig. 3.10, due to the laser being turned on and off respectively. A wavelength scan was also performed around this selected wavelength (as shown in the right pane of Fig. 3.10). What was found after performing this was that the dependence of the S parameter on the wavelength follows a Gaussian-like behaviour (caused by the Ps thermal distribution). The combined excitation and photoionization efficiency was determined to be around 15% [76]. The maximum corresponds to a wavelength of 205.05$\pm$0.02 nm. This agrees with the prevision of a previous work [77].

3.2.7 Positronium Transmission Characterization

Cold antiprotons and an efficient source of Ps are needed for the charge exchange process to be conducted. A e^+/Ps reflective converter is currently utilized as the source of Ps [80]. A novel way to upgrade the Ps source is to develop and implement a Ps transmission target for the increase of the quantity of themalized Ps emitted into vacuum. This would allow an increased quantity of antihydrogen produced and simplify the apparatus. The simplicity is in the form of transitioning toward an on-axis linear design from the current more in-

efficient off-axis design. A e^+/Ps converter was characterised within the Ps test chamber to test the feasibility of a new alternative for the current reflective geometry target [81]. The target tested consisted of an ultra-porous layer of meso-structured silica (thickness

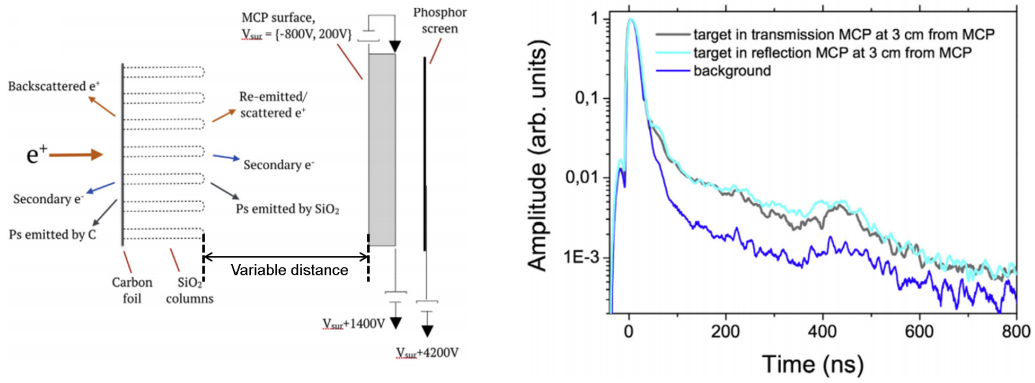

Figure 3.11: Sketch of the transmission measurement configuration (left) where the MCP is placed in front of the target to detect the secondary charged species produced. The target was inverted for reflection measurement. The lifetime spectra (right) are produced via SSPALS measured in reflection and transmission at an MCP-target distance of 3 cm (both images from Ref. [81]).

around 750 nm) evaporated over a 20 nm carbon foil (to provide a platform and mechanical stability for the film). The evaporation was performed with an e-gun at a glancing angle [82]. A $PbWO_4$ scintillator (located externally) was used to determine the Ps yield from the SSPALS spectra directed towards the central region where the target was placed (onto a movable actuator). The moveable actuator was needed to allow the converter to face upstream and then downstream for reflection and transmission measurements respectively. For both geometries, the Ps yield in vacuum was found to be around 7%, as reported from prior experimental studies [78, 82]. From the SSPALS spectra in both orientations (shown in the right pane Fig. 3.11), the o-Ps output was determined to be the same. This property opens the possibility for using these targets in both orientations.

An MCP was implemented to image and to monitor the quantity of other charged species (electrons and positrons) emitted from the target in both orientations. These images (Fig. 3.12) were taken in transmission geometry under differing potentials (between -800 V and +200 V), applied at the MCP frontal plate (see right pane of Fig. 3.11). It

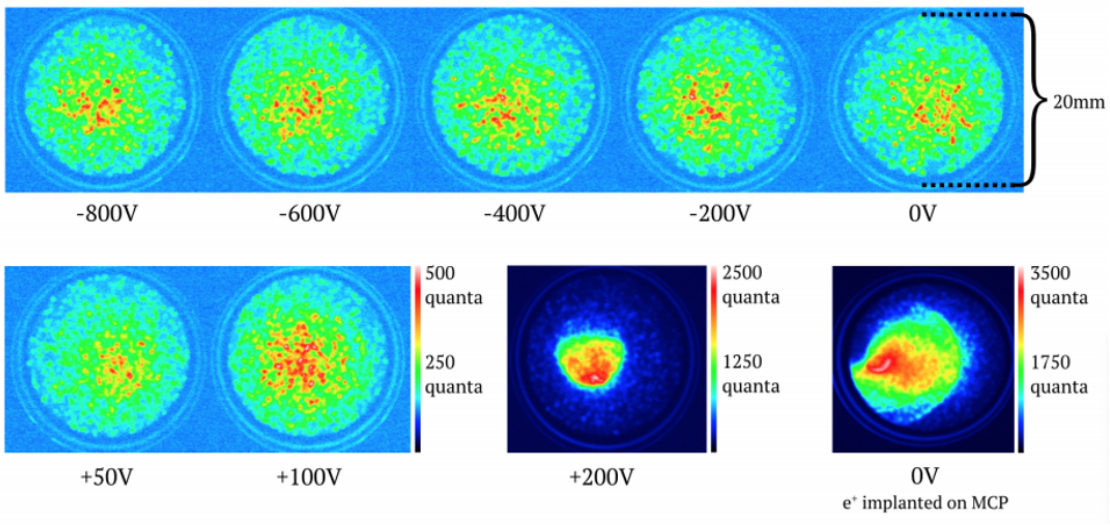

Figure 3.12: Images obtained from charged particles impinging on an MCP set-up as a function of the MCP surface potential applied, to determine the secondary electron energies. Positron implantation energy set to 3.3 keV (target set to transmission mode). The last image shows the particle spot without the target present (only positrons transmitted). Image also from Ref. [81].

was determined from these images that around 10% of positrons (around 1.2 keV) were re-emitted (initial positron implantation energy of 3.3 keV) [81]. Secondary electron emission in transmission was determined to be around 17% coming from the initial positron bunch in transmission mode.

3.3 QuPLAS

3.3.1 Introduction

Quantum wave properties have been observed for many types of matter-based systems (electrons [83], neutrons [84] atoms/molecules [85]). Even with advancements in interferometric technology, no such experiment has managed to observe the quantum interference behaviours with antimatter. CPT would suggest that symmetry should exist between matter and antimatter for a variety of properties but experimentally observing this has yet to be undertaken.

A new experimental collaboration (QUPLAS) plans to be the first to observe the interference behaviours with electrons, positrons and the matter/antimatter system positronium. The plan for QUPLAS is separated into a number of stages

QUPLAS-0) Measure and make a direct comparison of the quantum interference pattern of the positron and the electron, directly comparing antimatter and matter. The overall scheme is shown in Fig. 3.13.

QUPLAS-I) Obtaining the first ever interference pattern of positronium.

QUPLAS-II) Positronium Gravitation fall observation.

3.3.2 Experiment

QUPLAS is planned to follow the staged process to allow gradual progression towards the later and more complex steps. Work will be undertaken in tandem to allow the earlier phases to be completed and new technologies to be realised. The central location of the main experimental apparatus is at the VEPAS (Variable Energy Positron Annihilation Spectroscopy) where the existing continuous positron beam will be the main source of positrons, based at the Politecnico di Milano in Como (Italy). The positron beam has been described prior in Chapter 2. Without upgrades, QUPLAS-0 has all of the components needed for the experiment to take place. The later stages will need upgrades and new technology to be addressed (QUPLAS-I and II).

QUPLAS-0

The initial stage (QUPLAS-0) is directed to obtain separate inteference patterns of the fermionic particles as positrons and electrons. For the observation of these patterns, the positron system will be coupled to an interferometer and to a nuclear emulsion particle detector, as shown schematically in Fig. 3.13.

The position sensitive nuclear emulsion particle detector does already exist and has been tested with positrons [86] and antiprotons with the AEgIS collaboration [73].

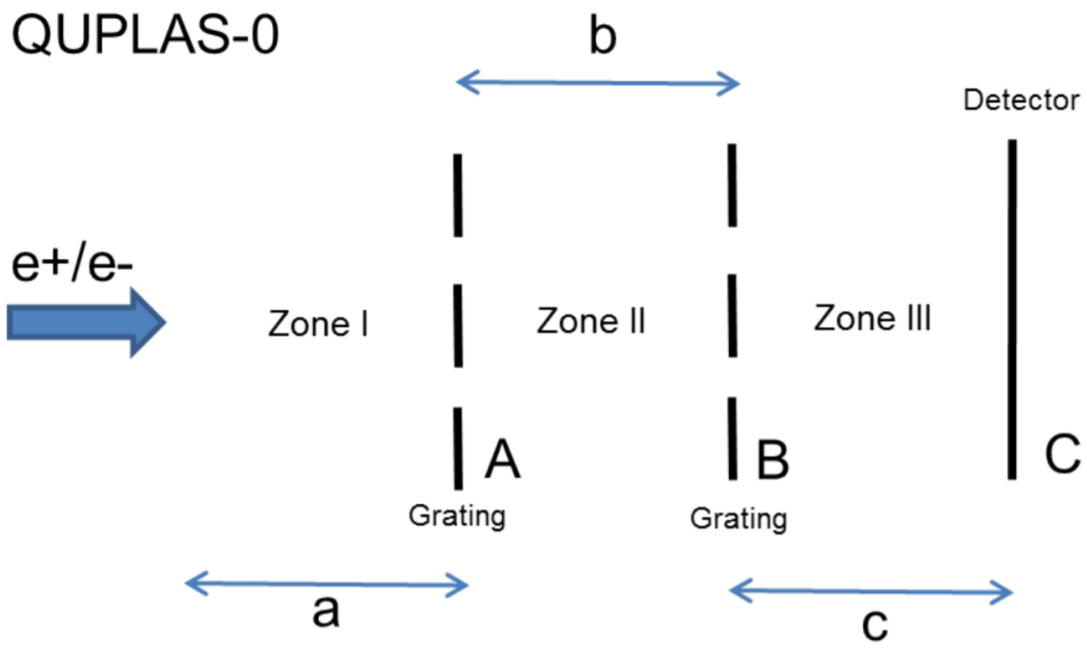

Figure 3.13: Schematic showing the initial phase (QUPLAS-0) where the two gratings are placed as a distance b from each other, and the emulsion detector at a distance c from the last grating.

The interferometric regime will be undertaken in the Talbot-Lau regime [87] with the continuous beam set to 10 keV. The interference gratings will have a nominal pitch of around 2 μm and 1 μm in thickness. With these current gratings and energies taken into account, the de Broglie wavelength and velocity can be calculated to be,

$$\lambda = \frac{h}{mv} = 1.2 \times 10^{-11} m, \tag{3.7}$$

and

$$v = \sqrt{\frac{2T}{m}} = 6 \times 10^{7} m/s, \tag{3.8}$$

respectively, where T is the kinetic energy and m is the positron mass (in the case for QUPLAS-I and II this would be the Ps mass). In this Talbot regime, the Talbot length L_T can be described as,

$$L_T = \frac{d^2}{\lambda} = \frac{d^2}{1.2 \times 10^{-11} m}, \tag{3.9}$$

where the pitch grating is d. The pitch defines the length where the periodicity repeats in the form of "Talbot Carpets" [87].

The precision of the micrometric gratings is the key to obtain the interference pattern in stage 0 (QUPLAS-0). Any errors made during the machining process would produce errors on the pattern produced. The current direction of the production of these films is through Electron Beam Lithography (EBL) for optimal construction. This will involve the development of a patterned resist deposition onto a SiNx-based substrate. A combination of dry and wet etching will be utilized for the reduction of thickness and obtaining the holed area with the required pitch as mentioned above. Currently between 30 to 60 % empty space areas are projected theoretically with this technology.

Lasers and incoherent light sources will be used for initial testing of these gratings during the prototyping phase. Talbot effects will be observable and analysed to determine the viability for the experiment, and for the future alignment procedures (where the rotational axis is paramount to correct). The same interferometer will also be used for electrons by replacing the positron source with a compact e-gun under the same energies. The projected e-gun consists of a tungsten filament or tip that can produce a thermionic or field emission based electron beam respectively. This change will allow direct comparison with electrons and positrons.

QUPLAS-I

This stage of the experiment aims on performing interferometry with the Ps atom. A pulsed positron beam (similar to the system mentioned in Section 3.2.3) would be implemented but with a transmission positron to positronium target prior to the first grating (as shown in Fig. 3.14). The transmission target will consist of a 1-10 μm thick mesoporous silica membrane where the positrons will enter and subsequently Ps will be emitted in the forward direction towards the gratings and then the position sensitive detector, in essence, creating a pulsed Ps beam when used with a pulsed positron system. As there are several processes which can

occur during the emission process (see section 1.2) unwanted charged particles (positrons and/or electrons) can also be present. Countermeasures will need to be researched into to remove the presence of these charged species.

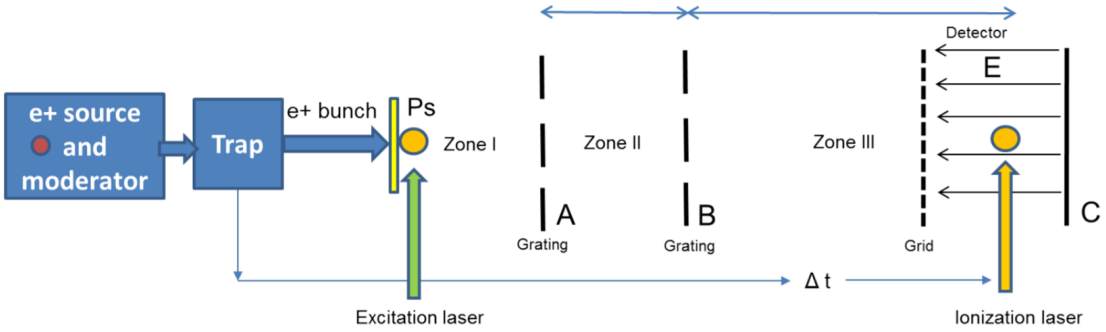

Figure 3.14: All zones are the same previously explained in Fig. 3.13 but in zone I, the new addition of a transmission target and pulsed positron beam will replace the previous continuous positron apparatus. In zone III, the emulsion detector will be upgraded to allow either laser ionization or via an induced electrical field to ionize the Ps passing.

The Ps of interest for this experiement is the o-Ps state where laser excitation is possible. Raising the state to a Rydberg level state is desireable to allow the Ps to live long enough to reach the position sensitive detector at the end of the apparatus. This process will be undertaken in Zone I (Fig. 3.14). It is projected that the o-Ps will be excited to a high n-state (>20).

For the laser excitation, a Nd:YAG laser (1064 nm) will be used in a Q-switched configuration. The laser will be coupled to duplication system to achieve second and fourth harmonic generation. As demonstrated in Section 3.2.7, the n=3 state can be achieved with Ps and QUPLAS plan to use the same first step prior to the Rydberg laser excitation (1 to 3 then to Rydberg). QUPLAS plan to excite the Ps high enough to obtain a lifetime on the μs scale.

For the detection of the Ps and the printing of the interferometric pattern of the Ps after the gratings, a specialized detector will need to be developed. A possible direction for this detection method could be coupling an emulsion (discussed in Section 3.3.3) based detector to a wire like structure at a precise voltage or incorporate a laser pulse for the ionizaion of

the Ps prior to the interaction with the detector (see Fig. 3.14, zone III).

QUPLAS-II

Once QUPLAS I is complete, a shift in direction will occur within the experiment (QUPLAS II). Now, the interest would be directed to the measurement of the gravitational fall of Ps. This would be a first new test of the Weak Equivalence Principle (WEP) on a matter/antimatter system.

Unlike the previous, this experiment would allow the ability to measure not only the interference pattern like in QUPLAS I, but also the displacement of the pattern produced by the interaction of Ps and Earth's gravitational field. This would require the use of the "slower" distribution of the emitted Ps (cooled by the mesoporous silica prior). For instance, when the Ps velocity is 10^3 m/s, it would produce a shift over a 1 m length of $\approx 5\mu$m.

3.3.3 Preliminary Results

This young experiment has been rapidly developing towards the QUPLAS-0 measurement. In this section a main achievement will be discussed in the form of the emulsion detector development [86].

Emulsion Detector Trials

These nuclear emulsions feature 0.2 micron diameter silver-bromide microcrystals within a gelatine matrix. Ionizing radiation interaction with these microcrystals create a latent image which (after a chemical development process) produces silver grains of around 1 μm. These grains are then visible via traditional optical means (e.g. Microscope, etc.). The University of Bern (a partner of the QUPLAS collaboration) produced these emulsions by pouring the gel onto a glass plate (holder). Glass was used to avoid thermal expansion issues (due to the small expansion properties). These films also had a 1.0 ± 0.1 μm gelatine

layer added at the surface of the emulsion to add protection from minor damages. A key factor of these films is their use within vacuum, such a possibility is granted by an addition of 1.5% glycerine to the gel to allow this, as reported in [88]. The VEPAS positron beam, described in Chapter 2 was used as the source of positrons for this trial. The positron kinetic energy was tuned between 3 to 18 keV to study the detection efficiency as a function of the positron implantation energy for a fixed exposure time of 120 $\pm$1 s. The beam spot at 15 keV is shown in Fig.3.15. The colours clearly can be used to determine the number of positrons detected [86].

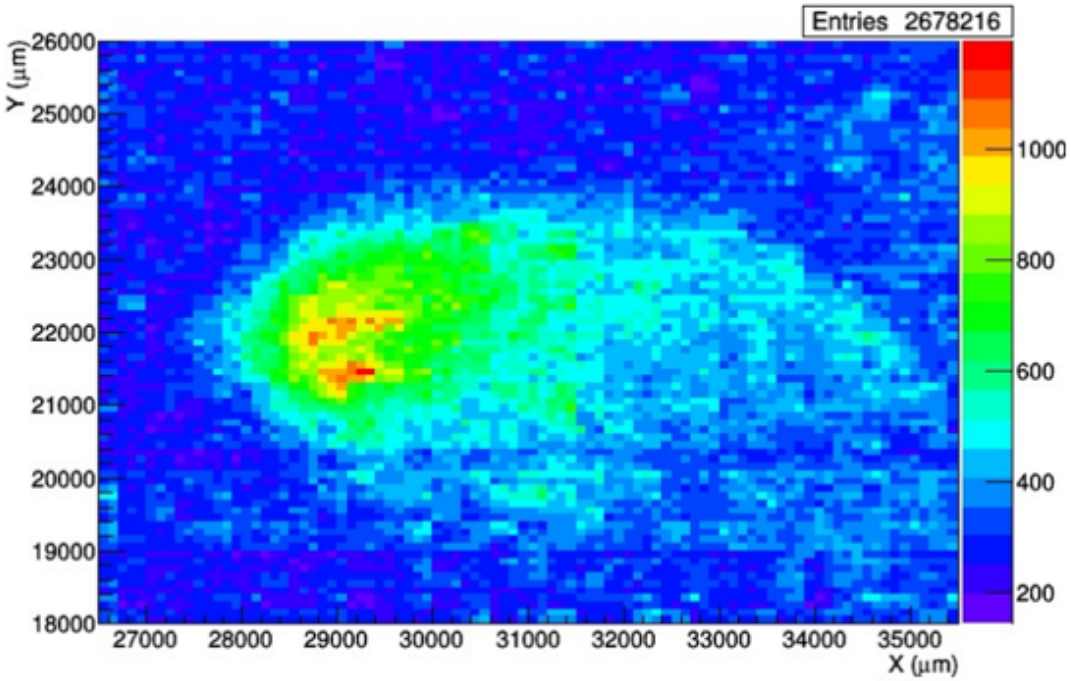

Figure 3.15: The beam spot image obtained with the emulsion detector. This profile was of 15 keV positrons. The colours indicate the number of positrons at the emulsion surface [86].

Figure 3.16 illustrates the positron implantation profile calculated into the 1 μm protective layer and emulsion detector. Higher energies were needed to pass through this layer to allow the positrons to annihilate inside the emulsion layer. From the beginning of the study, it was expected to not see minimal results from the lower energies due to this layer.

The emulsion (intrinsic) efficiencies were estimated (within error) to be about 80%. It was

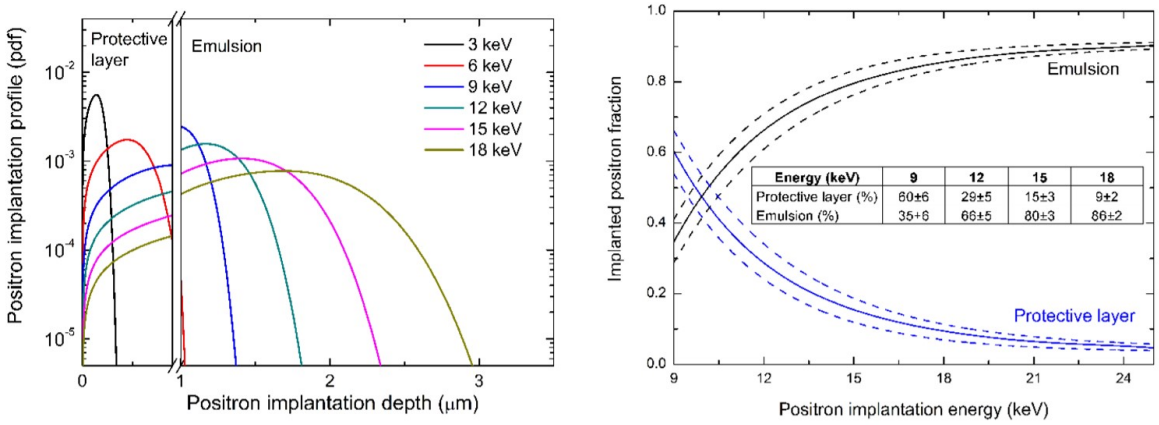

Figure 3.16: The left pane illustrates the calculated positron implantation profile where it shows the positron interaction between the protective layer and the emulsion itself and the right pane shows the positron fractions experiencing annihilation within the protective layer and the emulsion layer as a function of the positron implantation energy [86].

found that this didn't change with the positrons implantation energy, as shown in Fig. 3.17. From the results obtained and published, it was safe to say that these emulsion detectors were deemed useable for the upcoming interference measurement.

3.3.4 Future work

This step, will focus entirely on the interferometric properties of laser excited o-Ps. The overall scheme can be observed in Fig. 3.13. In our design, what is required is to have a beam (pulsed or continuous) of positronium, from a transmission target (concept shown in Fig. 3.18). It has been simulated that a mesoporous (pore diameter ≈1-10 μm) with interconnected pores free-standing silica target would be the ideal for this task (more detail in the next chapter). As mentioned within this chapter, some methods have already been explored with interesting results, but with an excess of charged particles rendering them too problematic for use with this apparatus. The realization of a target without charged particles emitted is desired for this experiment and further research with the detection methods will be explored for the neutral atom. The works presented in the next chapter are related to

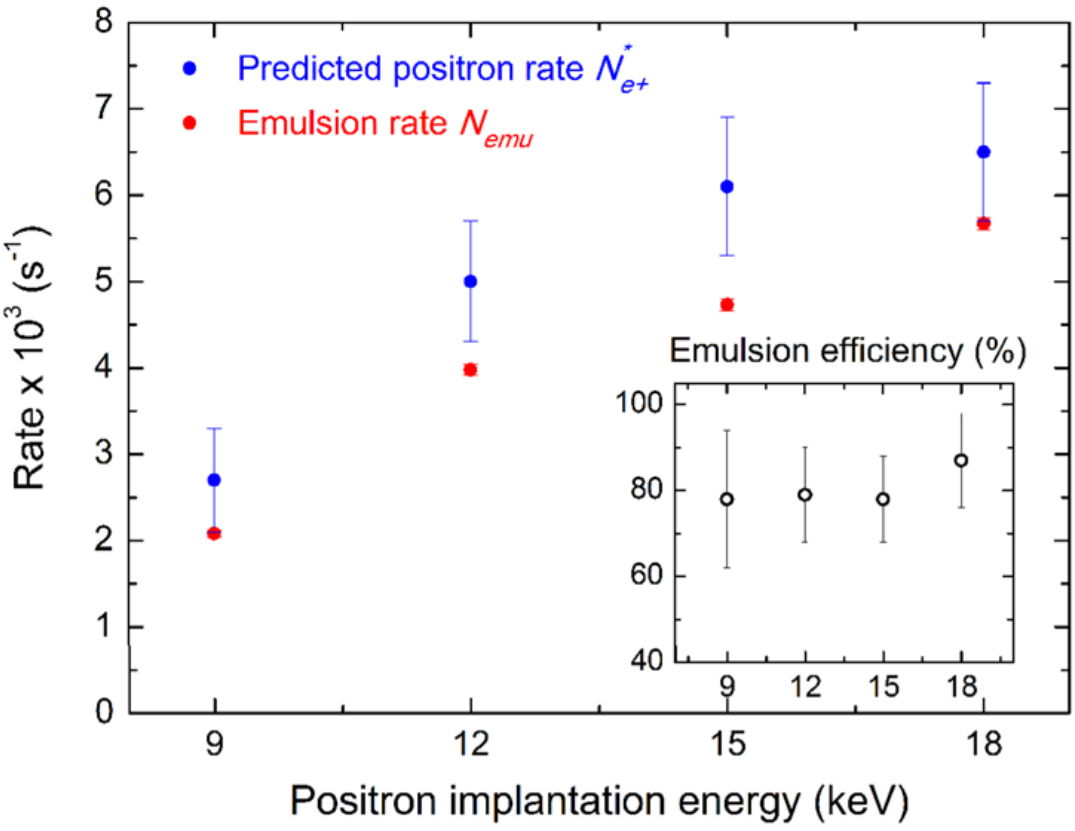

Figure 3.17: A direct comparison with the predicted and detected rates of implanted positrons as a function of the positron implantation energy. The emulsion efficiencies are detailed in the inner figure [86].

possible solutions to the transmision target needed for this experiment to continue.

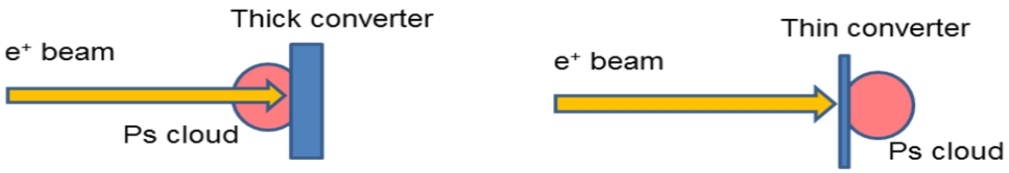

Figure 3.18: A proposed change in the direction of emission of Ps from the classic reflection geometry to the new transmission geometry.

CHAPTER 4

POSITRONIUM TRANSMISSION TARGET DEVELOPMENT

4.1 Motivation

As discussed in the previous chapters, the most common method of creating positronium is with use of a mesoporous silica target which emits in the standard reflection geometry. The quantity of Ps emitted depends on certain properties of the material in question (porosity, interconnectivity, pore diameter, thickness, etc). The lateral area is also important which is highly dependent on the dimensions of the beam spot for the maximization of the output. From Monte Carlo simulations undertaken by S. Aghion [37], a colleague based at the VEPAS lab, Como, it was deduced that a change of geometry would greatly benefit the quantity of "cold" Ps emitted into vacuum from the material. The simulation was based on a semiclassical model which takes into account the Ps behaviour within the mesoporous silica (which included Ps cooling and diffusion). Certain parameters for this prospective target was predicted, between 3-10 nm in pore diameter and a thickness between 1-5 microns (based on Aerogel data [37]). The surface area of the target would need to be comparable to the diameter of the beam (proposed silica area around 1 cm^2). This is all well and good theoretically, but the challenge arises with the synthesis of such a target. Very thin glass-like materials are known to be highly unstable and fragile as the surface area increases. A further element which adds to the perceived fragility due to the mesoporous networks needed within the film. Until now, standard techniques alone (i.e. selfassembly, spincoating, etc.) have not managed to produce the film with the correct parameters. In this chapter, a discussion will be presented on the various mesoporous silica films produced throughout the PhD period.

4.2 Silica Thin Film Production

4.2.1 Liquid to air interface films

In collaboration with the Edler Reserch group based in Bath University and lead by Professor Karen Edler, the research and development phase began (over a three month period) on finding good candidate materials for the task at hand. Their expertise working in the production of thin mesoporous films, stemming from previous works [89], contributed greatly in the development phase. A common approach for the preparation of these films is using a base tetraethoxysilane (TEOS) or a tetremethoxysilane (TMOS) as the source of silica. The solution required a surfactant template embedded within the solution which hexadecyltrimethylammonium bromide (CTAB) provides. The solution operates under acidic conditions during a regular synthesis process (around pH=2). This would then be placed into a container with a high open surface area and allow the silica sol-gel layer (pre-calcined silica solution) to form on top of the solution (under static conditions). A scheme of the synthesis is shown in more detail in Fig. 4.1.

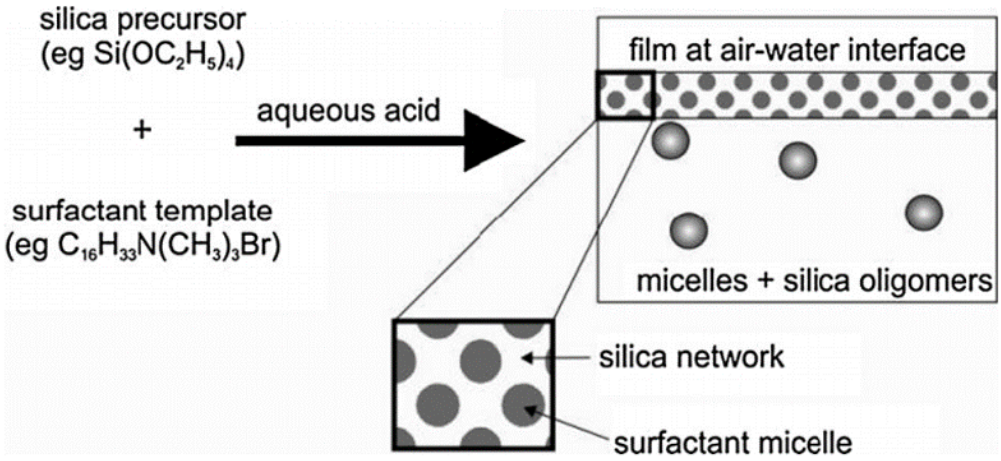

Figure 4.1: Silica-surfactant formation at the air-liquid interface via the synthetic route [89].

Typical thicknesses for these films can range around a few tens of nm [90] to around 20

μm [91]. Instead, typical pore diameters for these materials are around 3 nm. Harvesting these films can be accomplished in a few ways, via a substrate or mesh with an open area allowing the formation of self-supported films [89]. To obtain a mesoporous material from these films, they need to undergo a thermal process (calcination). This is usually undertaken with use of a high temperature oven with a controllable rise time. This removes the surfactants from the film, leaving a silica "skeleton" behind. This removal process has been known to cause unwanted effects to the nanostructure of the film, such as structure collapse and increased fragility [92]. At first attempts, due to the original recipe [89] having a low surface area, tweaking the original recipe was needed to obtain the desired film. For the films presented in this work, Polymer-cationic surfactant templated silica films were produced. Solutions were prepared prior. All solutions needed to be kept around 40°C.

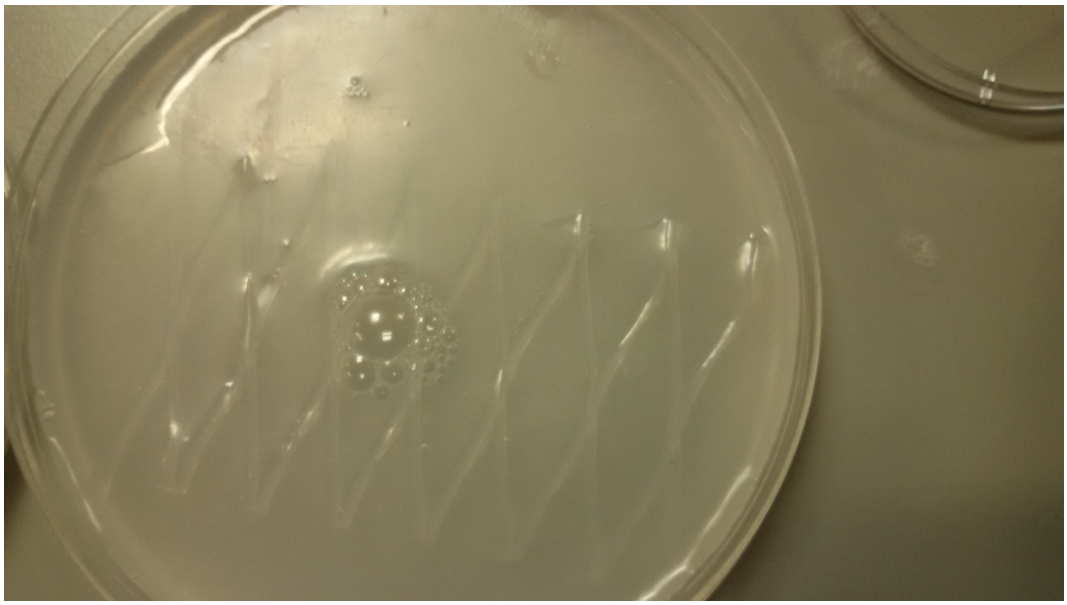

Figure 4.2: Solution freshly poured into a Petri dish with plastic mesh placed at the bottom.

The recipe for producing these samples included these preprepared components:

Hexadecyltrimethylammonium bromide (CTAB) solution (0.074 M)

Sodium Dodecyl Sulphate (SDS) Solution (0.0925 M)

Polyethyleminine (LPEI MW 750,000) Solution (60g/L)

The method for a typical 30 mL volume would involve adding 4 mL SDS solution with 15 mL of the CTAB solution into a polyethylene bottle. The mixed solution should become cloudy and give a CTAB:SDS of 4:1. 12 mL of the LPEI solution was then added and gently stirred magnetically with the bottle closed. This quantity of LPEI solution would give 24 g/L concentration to the combined solution. Once stirred, 0.084 M of TMOS was added and the solution continued to stir. Mesh was positioned within a wide Petri dish and the solution was poured over it as shown in Fig 4.2, submerging the entire mesh. The solution was left over night to form on top of the liquid surface. Initially a plastic mesh was submerged inside the Petri dish used for synthesis which was used for the harvesting of the film. Once removed, the film was placed hanged out to dry as shown in Fig. 4.3 also removing the excess solution which did not form beneath the membrane.

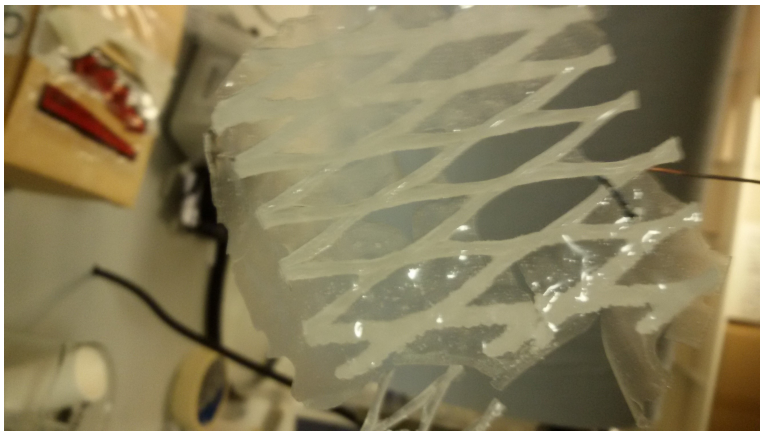

Figure 4.3: Film harvested and left to hang and dry, removing excess solution.

As you can see, not all open membranes within the mesh held its form and broke during either the transferral or the drying process. Once dried, the inner sections shown in the left image of Fig 4.4 were carefully removed and placed within a furnace for the calcination process. The oven (starting at room temperature) was set to a 1°C/min rise time to a maximum temperature of 600°C. This was done to completely remove the surfactants and leaving pure silica behind. The same slow rate was used to reduce the likelihood of pore collapse and damage to the film.

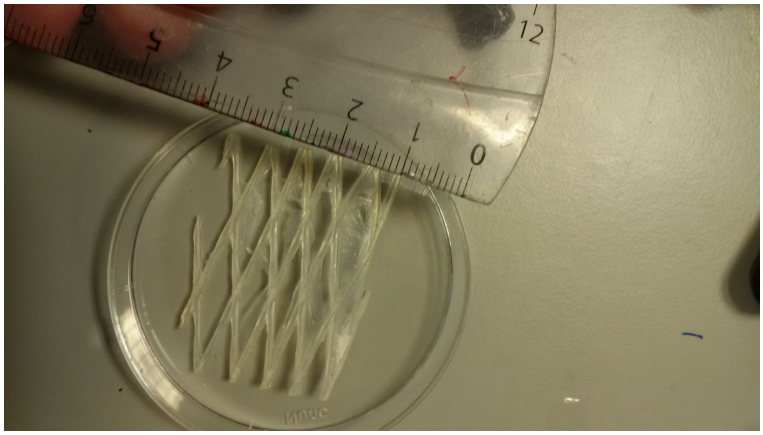

Figure 4.4: Dried film with a few broken films within the mesh.

Also shown in Fig. 4.4 is that the sizes of the films harvested with this recipe was too small for what is needed for the final target. It was also noticed that after film removal was that a lot of material was left behind unharvested. Changes to the removal frame was explored with varying results.

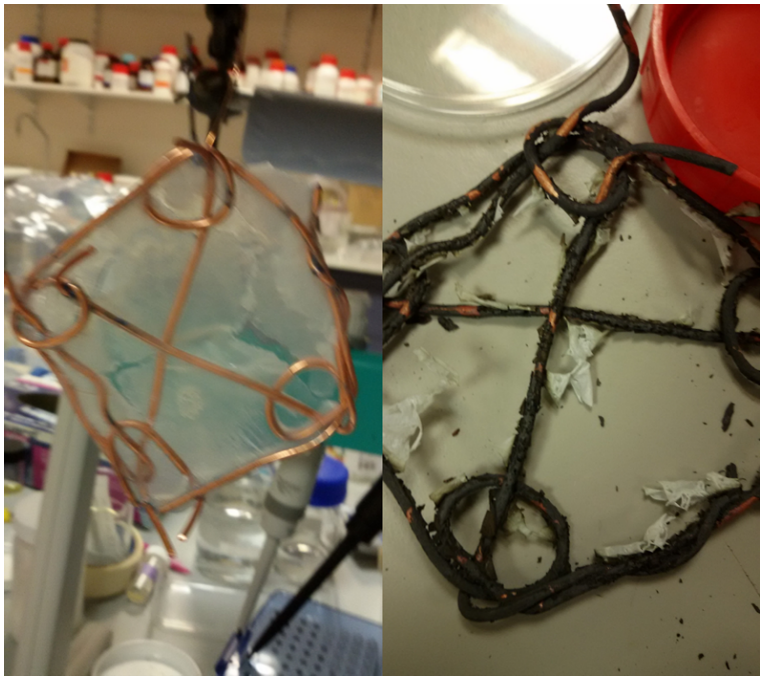

Figure 4.5: Homemade copper-based removal tool to remove larger areas and to calcine together with the film before calcination (left) and after calcination (right).

A copper based removal tool was tested with the film removal (being successful) but after the calcination process a reaction with the copper and the film caused destruction of the film, as shown in the right image of Fig. 4.5. Smaller copper based frames were also tested with similar results (Fig. 4.6).

Figure 4.6: Fine copper mesh after calcination.

With the harvesting process, at times shown in Fig 4.7, a larger piece can be removed. From this information in regards to the properties of these films, knowledge of fragility of the films were better understood. Even the removal process had the possibility of damaging these films.

Figure 4.7: Mesh showing an elongated section removed from the solution.

A novel method of removal of these films was developed after receiving this new infor-

mation. As a test, the mesh was cut to allow a larger open area. This allowed the removal of films with a larger surface area.

Figure 4.8: Film removed using mesh with cut section at the center to increase the surface area.

Figure 4.8 shows the result of this method. This produced a film which could be calcined and used for testing by means of the VEPAS positron beam. In this case, the thickness of the film was around 200 μm and the lateral dimension 2 cm $\times$ 1.5 cm. Further expansion of the surface area led to a new method for removal. Shown in Fig 4.9 is the way of removal utilizing a piece of teflon below.

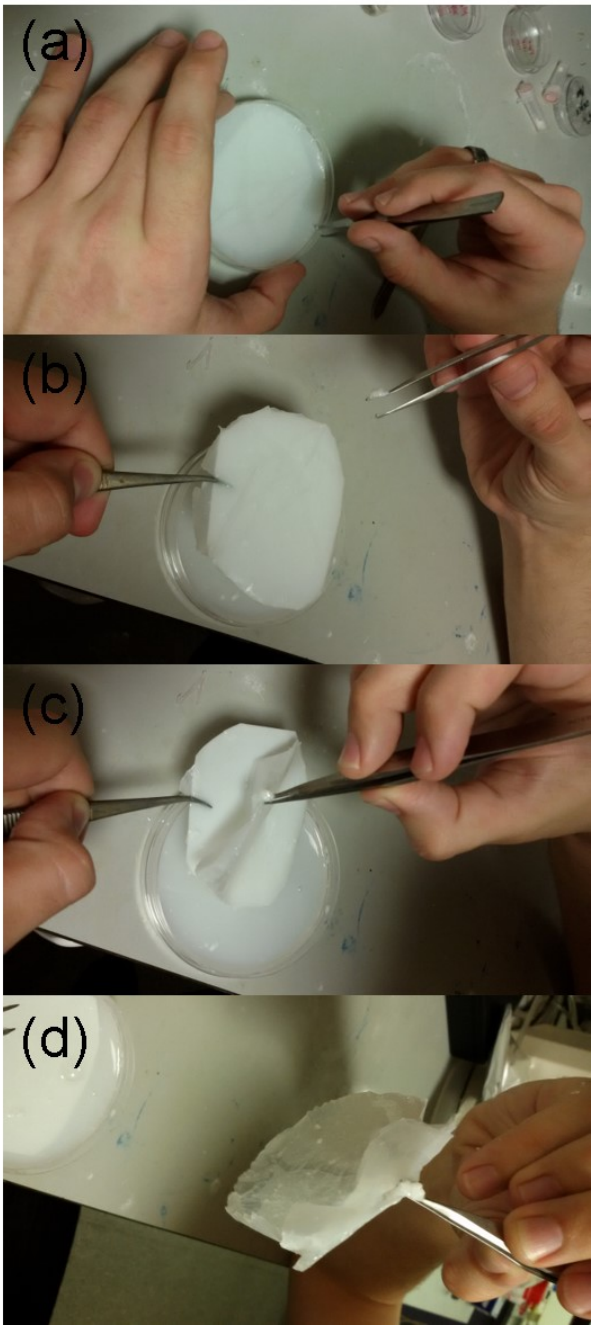

Figure 4.9: The teflon assisted method for liquid to air interface film removal, (a) physically separate the film from the outer rim of the dish, once complete (b) lift the teflon with the film and mesh on top, draining partially the excess solution. (c) use a separate tweezer at a higher angle to separate the film from the teflon continuing to drain the excess. (d) remove and set film to dry.

First, the outer circumference is carefully cut with a pair of tweezers to separate the formed film from the inner walls of the Petri dish. Then the mesh and teflon are lifted simultaneously with two separate tweezers at a 45° angle. This allowed drainage of the excess material and whilst lowering the possibility of tearing. Nearing the end of drainage, the mesh is lifted at a high angle and then removed from the teflon area.

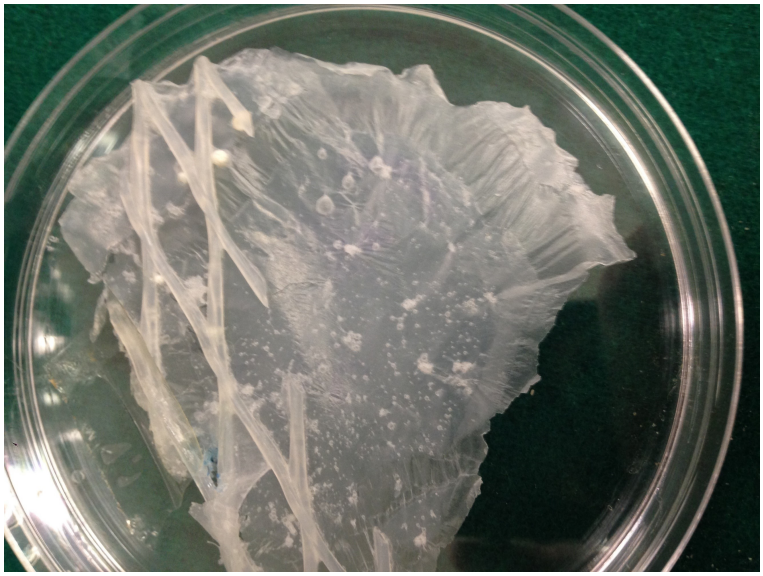

Figure 4.10: Large area liquid to air interface film obtained from teflon assisted removal.

This is then hanged out to dry as prior films. The finished extra large surface area film is shown in Fig. 4.10. Calcination of this film keeps most of its area and curls a lot less comparing to previous films (Fig. 4.11). The white colour is caused by natural microcracking during the calcination process. The fragility of these films made them very hard to handle making them very difficult to test for positronium production properties.

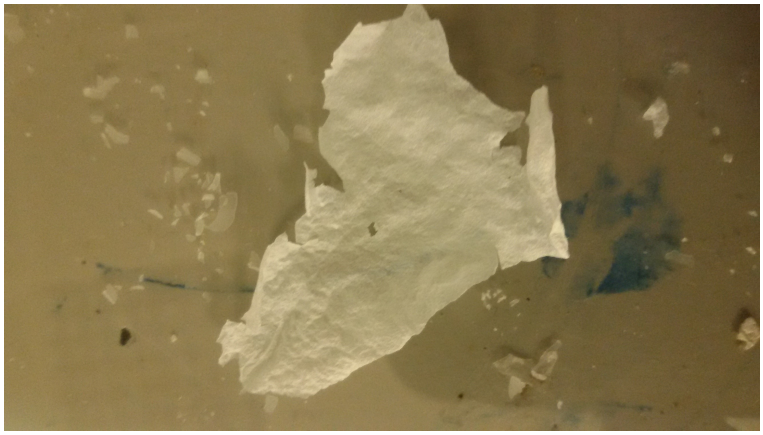

Figure 4.11: Calcined film of film obtained from teflon removal.

The precalcined film can cut into individual pieces and moved quite easily due to a much higher amount of elasticity. To improve manipulation after calcination, an aluminium holder with an open section was produced for each film as shown in Fig. 4.12. The frame needed to hold the film, but also be loose to not allow cracks during the changes in position due to thermal expansion and contraction. A successfully calcined film can be seen in Fig. 4.13. A benefit to the aluminium foil is a slight reduction of the curling process during the thermal process.

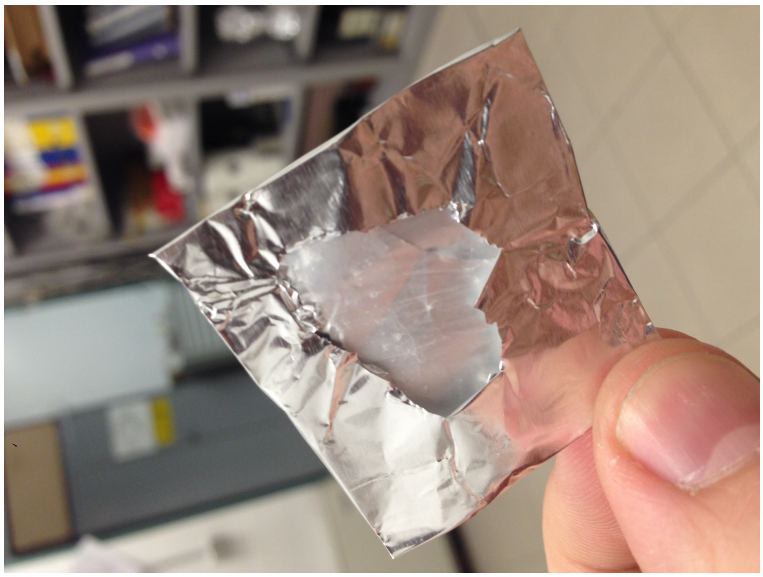

Figure 4.12: A cut piece of LTA film encased in aluminium holder, prior to calcination.

Figure 4.13: LTA calcined film within aluminium holder.

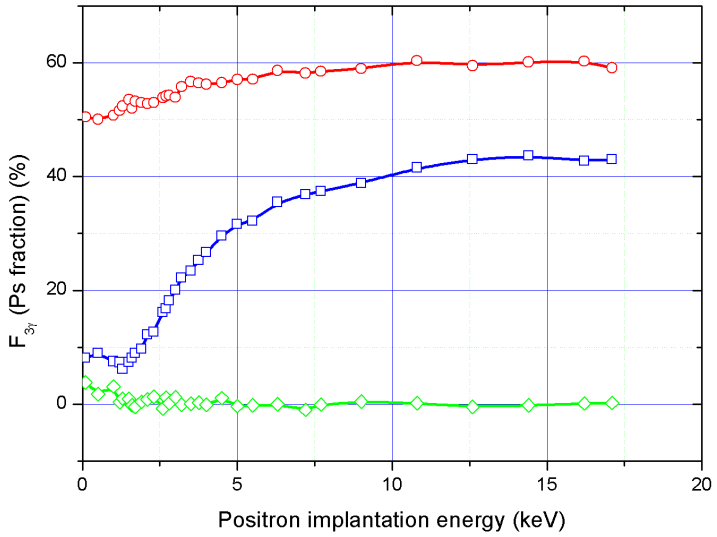

Figure 4.14: 3-γ fraction at varying energies showing the new LTA silica film (blue squares) comparing to well documented materials in the form of Aerogel 85 (red circles) and Aluminium (green diamonds).

The VEPAS positron beam was used to explore the positronium formation properties

of the material after calcination and make a comparison with other well-documented materials, shown in Fig 4.14. It is well known in the positron community that classical metals produce zero positronium within the bulk [93]. This was used as a zero for the o-Ps at higher positron implantation energies at the surface, positronium can be formed. Aerogel, a material studied extensively within our positron group was used as a comparison to these new materials. Aerogel has been proven to have a positronium yield of around 60%, one of the highest quantities studied so far. The LTA sample begins with a very low quantity of o-Ps formation around the surface and within the initial sections of the inner material. Comparing to the open-pored aerogel, it can be said that the pores of this material are closed, blocking low energy positrons access to the inner mesoporous zone (lack of surface to bulk interconnectivity). As the positrons increase in energy (between 2-3 keV) a sharp rise is observed. This indicates the positrons reaching the pore network and forming positronium inside the mesopores. The maximum yield for positronium was determined to be around 42% at the higher energy ranges, comparable to Aerogel.

As a candidate towards the final goal of obtaining positronium formation in transmission, these targets need to change some physical properties to allow this to happen. Comparing to the properties provided by the simulation mentioned in Section 4.1, targets are 2 orders of magnitude too thick making emission of Ps in transmission impossible with low implantation energies. As an emphasis of this, there is no decline in positronium formation via the pick-off effect present with the LTA data, meaning no positronium passes and interacts with the aluminium holder behind the silica, (the same with the Aerogel data). A preferential property in regard to the morphology would be to keep the bulk morphology, but to improve the initial layers between the bulk and the surface increasing the interconnectivity and thus reducing the implantation energies needed.

Reducing the thickness would not be a trivial process, from the original recipe to produce these films, creating an area large enough for the beam diameters due to the original micrometric thicknesses produced (and curling effects during calcination).

4.3 Spin-coated self-standing mesoporous 3D Silica

4.3.1 Spin-coated 3D Silica Synthesis

This method was explored with collaboration with the University of Milan and the Smart-MatLab (Milan) as a different and more controllable way to obtain films closer to the 1-5 micron thicknesses needed for the final target. A year and a half was dedicated on creating this prototype. Spin-coating has been known historically to be able to create thin homogenous films with varying meso-structures. The silica formulation used in this section of the thesis was originally reported here in Ref. [94], where they managed to create differing morphologies from the surface to air interfaces after calcination. These films were produced by initially magnetically mixing TEOS to a aqueous solution of water (pH=1.25 with HCl) and ethanol (molar ratio 1:5:3.8). The surfactant CTAB was ultrasonically combined to the solution with a CTAB/Si molar ratio of 0.1. It is suggested within the same article that for thicker films (around 1 micron), the solution should be diluted to a ratio with ethanol of 1:1 [94]. Further dilution would decrease the viscosity of the gel and thus reduce the thickness after spincoating. Filtration was done to avoid aggregates formed within the solution (0.45 μm) before being added to the substrate. The filtered solution was administered onto the Si [111] substrate surface and spun at 2000 RPM with an acceleration of 1500 RPM/s. A cylindrical oven was used to calcine the sample, for these samples, the rise time was set to 1°C/min from room temperature up to 500°C. The samples stayed at this temperature for 12 hours to thoroughly remove the surfactants. Then the temperature was reduced gently (1°C/min) until returning to room temperature.

XRD analysis [95], in collaboration with Daniel Chrastina (LNESS), was undertaken to monitor the inner properties of the material before and after calcination. It is important to follow the evolution of the target to avoid having the inner structure collapse in on itself. Also after the removal of the surfactants leaving the skeleton-like mesoporous network it is likely that the pores should shrink to a certain degree.

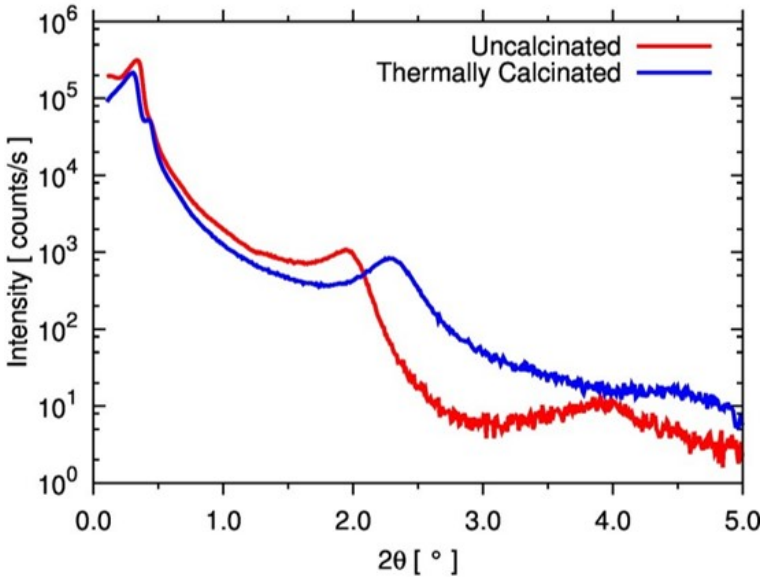

Figure 4.15: XRD 2θ-ω (scanning of the incident and diffracted beam) measurement showing sample 3D Silica before and after thermal calcination, 2θ corresponds to the angular position of the detector as it rotates around the sample and ω is the angular position of the sample.

Figure 4.15 shows the XRD results taken at the surface of the 3D Silica sample. The second peak for an angle of 2θ=2.0° indicates a pore periodicity at the surface of around 4.5 nm. It is clear that the peak shifts to 2.3° after calcination. This result indicates that the pore periodicity remains after the removal of the surfactant, but reduced to 3.9 nm.

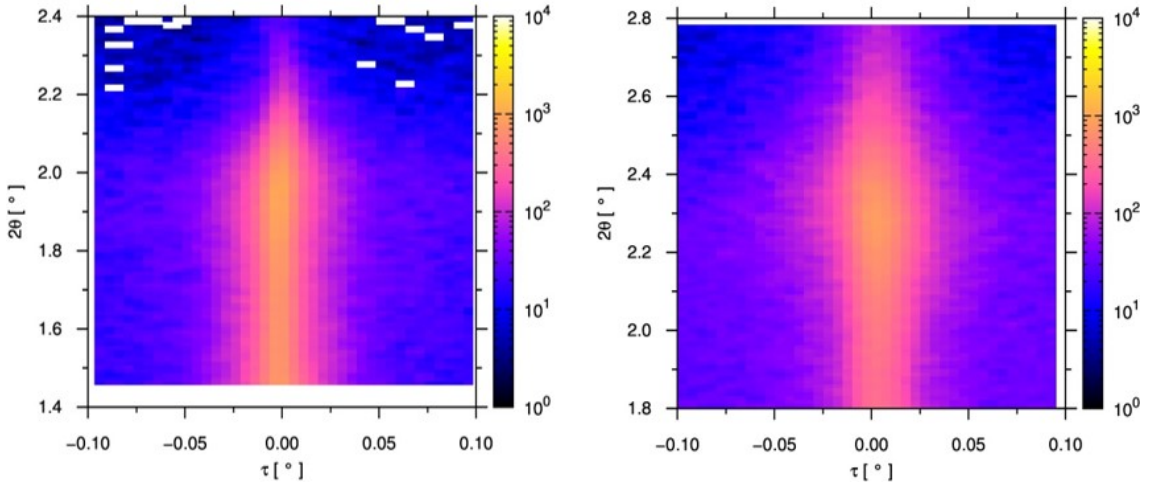

Figure 4.16: 2-dimensional reciprocal space maps plotted with 2θ as the y-axis and tilt $\tau = 2\theta/2\ \omega$ as the x-axis, relative to the surface normal, for the 3D Silica sample before (left) and after (right) thermal calcination. The intensity scale is logarithmic. The diffracted and reflected intensity is concentrated within a very narrow range close to the surface normal, indicating both that the surface is smooth and that the periodicity within the material is well aligned with the surface.

Figure 4.16 shows a 2D reciprocal space mapping measurement to monitor the alignment before and after calcination. The layers stayed well-aligned to the surface normal for both steps (within around 0.05°).

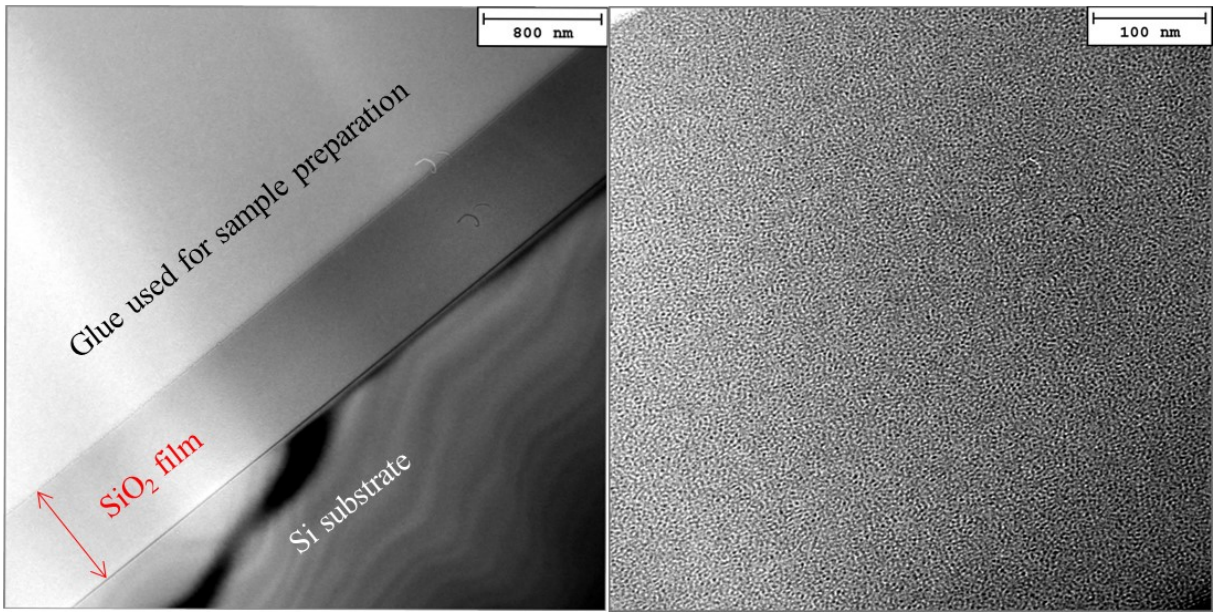

Figure 4.17: HRTEM images showing linearity of the film (left pane) and the morphology (right pane).

Looking deeper into the sample via High Resolution Transmission Electron Microscopy (HRTEM), this disordered structure is confirmed as shown in Fig. 4.17. The thickness was determined to be 740 and 760 nm for spin speeds 2000 and 1500 RPM, respectively. Looking deeper into the material, the morphology has a difference between the silica and the interface between air and the substrate as shown in Fig. 4.18, this layer has a thickness around 5 nm and this phenomenon has been described previously here in Ref. [96].

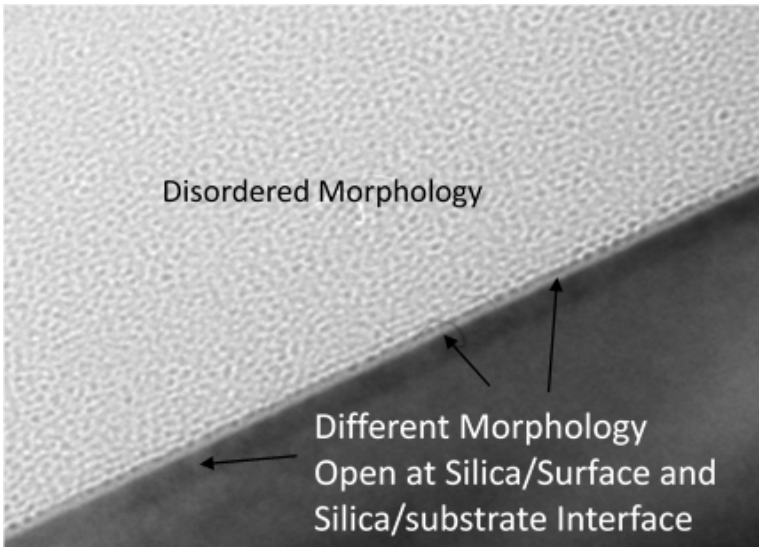

Figure 4.18: HRTEM image of the mesoporous 3D Silica film showing morphology differences at the bulk to air interface.

4.3.2 Transferral Process

The sample 3D Silica has useful properties in terms of positronium production, as we will see later in (Sec. 4.4), the direction of research was now to alter it to allow positronium in the transmission geometry. As the mesoporous material is fused onto the substrate after being calcined disallowing removal, a way was needed to allow removal. The plan was to remove the base sol-gel film before calcination. The method used in this work was to utilize sacrificial layer to allow the film to be released from the substrate. The transferral process has been proposed in [97] and was implemented for the removal of the film from the substrate. A polystyrene (PS) and toluene solution (50 g/mL) was spun at 2000 RPM onto the substrate prior to the sol-gel creating a continuous PS film.

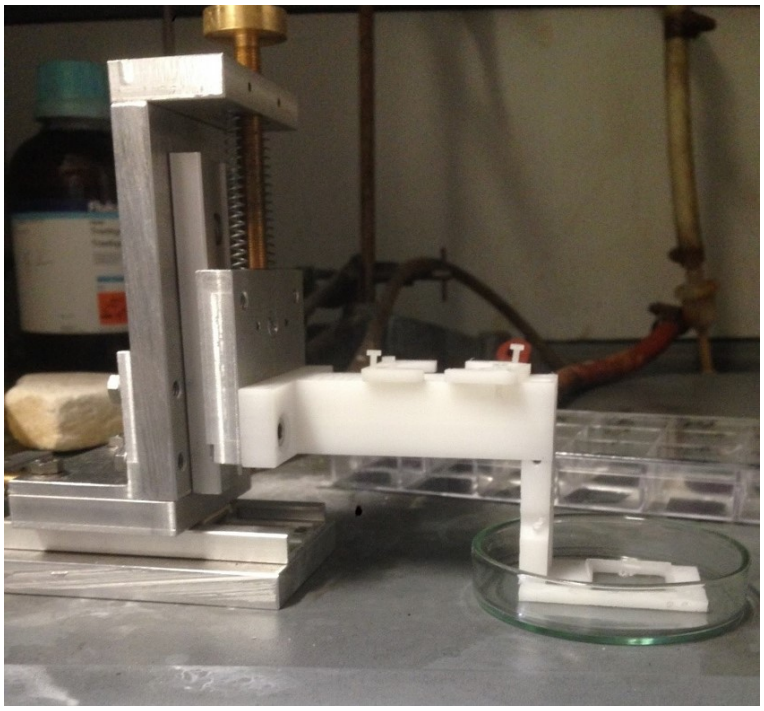

Figure 4.19: Transfer apparatus for the gentle lowering and raising procedures manually.

The sol-gel was spun subsequently on top of this PS layer at the same spin parameters. The sample was then placed in a transfer apparatus designed for lowering and raising these substrates, shown in Fig. 4.19. The substrate was lowered into a toluene filled container to initiate a dissolution process, removing the PS layer and detaching the sol-gel film. This would lead to the film to float on top of the solution ready for the new substrate. A specially laser assisted engineered holed substrate (presented in the next section) was then placed beneath the floating film and raised in line with it. The transfer apparatus was needed due to the fragility of the film over the open sections and to minimise any shocks as the film is removed from the toluene. The sample was left to dry in this position prior to calcination. Findings within the original article concluded that the properties of the mesoporous silica (after calcination) does not change after transferral [97]. Fig. 4.20 illustrates the method used for the the transferral process.

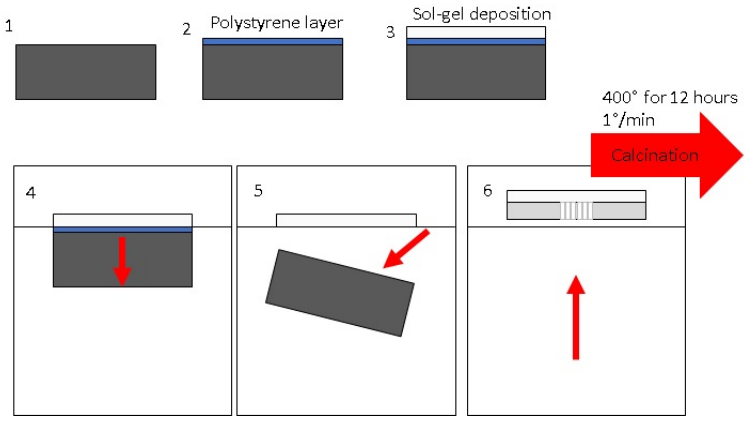

Figure 4.20: This is a concept of the transferral process to achieve the self standing film. 1) is the base silicon substrate, 2) PS layer is spincoat upon the surface then left to dry over an hour period. 3) The original 3D Silica sol-gel recipe is spin coated over that. 4) The sample is introduced to a beak filled with toluene to initiate the desolution process of the PS layer. 5) The PS layer is removed and frees the substrate from the (now floating) sol-gel. 6) A new target with an open volume is introduced using the raising apparatus to lift up the mesoporous material.

4.3.3 Fused Silica Holed Substrate

As mentioned in the Section 2.2.2, a specially machined substrate was needed to allow the substrate to self-stand. Fused silica was chosen for the substrate material, chosen for its close thermal expansion properties to the mesoporous silica. It was important to match these properties to reduce the probability of cracks and destruction during and after calcination. In collaboration with R. Osellame and R. Martínez Vázquez from the Department of Physics of Politecnico di Milano, a glass irradiation and chemical etching technique was utilized for the goal of creating holed substrates with transmission properties [98]. The aim was to reach the largest quantity of empty cell area possible to allow the most positron to positronium conversion with these films. The typical dimension of the fused silica sibstrate was 25 mm $\times$ 25 mm $\times$ 0.5 mm (Fig. 4.21).

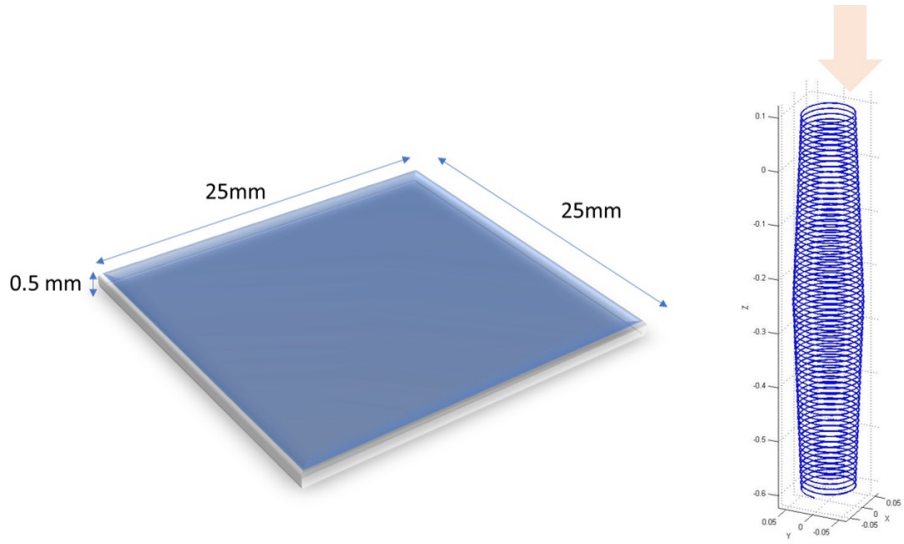

Figure 4.21: A computer generated image of the typical dimensions of the fused silica used (left pane). On the right, illustrates the irradiation path used for the creation of the cylindrical holes to allow an open void to be created. An arrow shows the direction of the laser into the material

The holes were produced by moving the laser down a cylindrical path into the material irradiating the selected zone (shown in Fig. 4.21), then chemical etching would be implemented to remove the glass cylinders out of the substrate, leaving cylindrical holes in the substrate.

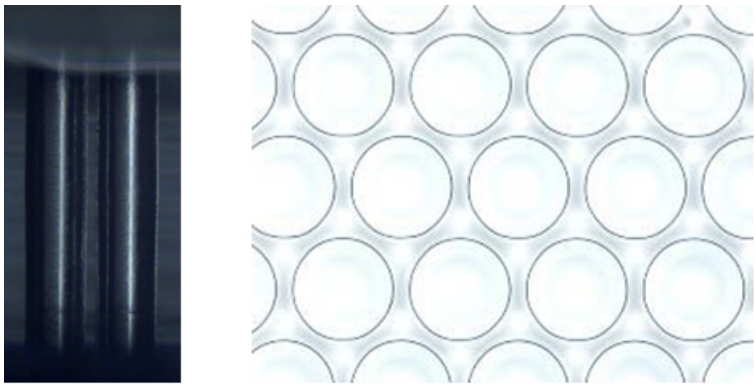

Figure 4.22: The newly created cylindrical voids shown from the side (left pane) and over the top showing the design (right pane).

The first substrate produced had the holes designed in a square cell of hole of 105$\pm$1 μm in diameter, design shown in Fig. 4.22 and an empty cell area of round 35%. This was over a matrix area of 1.95 mm $\times$ 2.1 mm. A proposal was presented to change the design layout of the holes to a more hexagonal based one and to increase the hole diameter to increase further the empty cell area to maximize the amount of positronium in transmission.

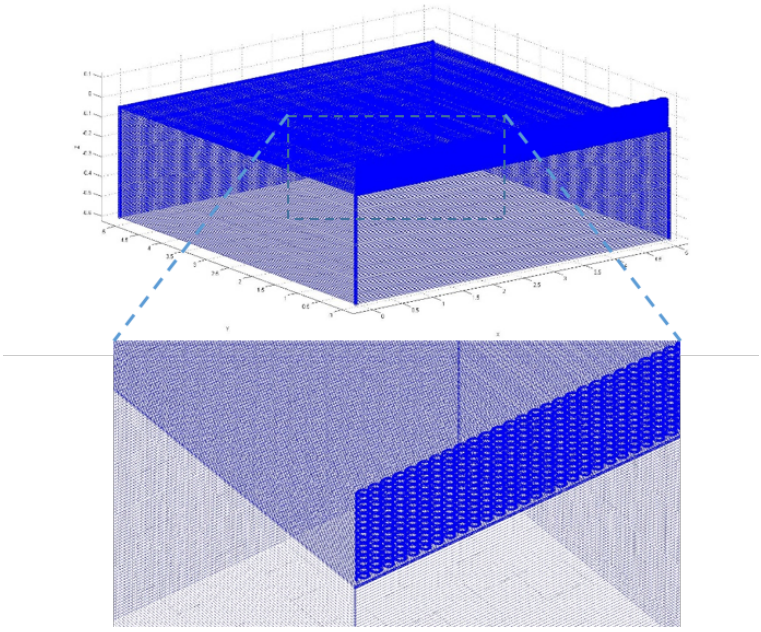

Figure 4.23: Computer aided design of the irradiation path selected for substrate 10 (see Table 4.1). This includes the separate cylindrical path (for the hole creation) and a block radiation section (for thickness reduction).

To further reduce the probability of positronium annihilating with the substrate and to reduce the effect of the substrate expansion during the calcination, the thickness of this area was reduced through block irradiation of the back of the substrate. A simulation shown in Fig. 4.23 shows the irradiation sections and the method used for reducing the substrate thickness.

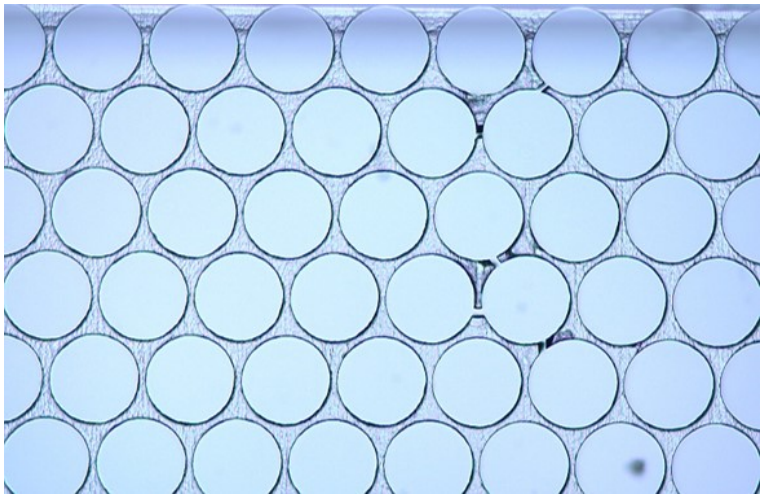

Figure 4.24: An image of the top design of substrate 10 featuring some irregularities due to the large thickness reduction (20 μm).

The lowest thickness possible for the substrate was to around 20 μm, where it showed the limitations of this technology due to irregularities being present, shown in Fig. 4.24. All details on the successfully obtained substrates are shown in Table 4.1. A photo of the 20 μm thick target located at the center of the fused silica glass can be seen in Fig. 4.25.

Substrate	MATRIX (mm^2)	Hole Diameter (μm)	Thickness (μm)	Open cell area (%)
1	1.95×2.1	105(1)	500	35
2	1.95×2.4	123(1)	500	50
3	2.36×2.4	131(1)	500	68
6	2.36×2.4	130(1)	250	68
8	5.15×5.2	139(1)	60	77
10	5.15×5.2	139(1)	20	77

Table 4.1: Table showing the successful laser machined fused silica.

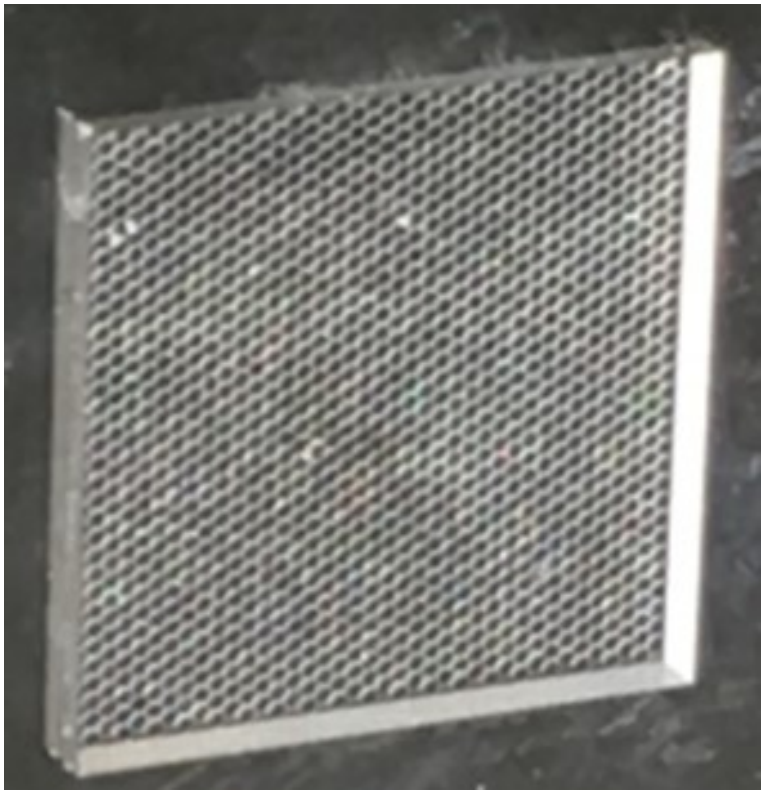

Figure 4.25: Photo showing substrate 10 where the thickness was reduced to 20 μm and leaving an open cell area of 77%.

4.3.4 Final Target

Once the transport was carefully completed, optical analysis needed to be undertaken to determine the quality of the transfered film. This would need to be undertaken before and after the calcination process. In Fig. 4.26, the reflection of the light can be seen across the

hole areas proving the film existed on top of the grided area. Also from this picture, it can be observed that the film isn't perfectly linear across the area where some ripples in the film can occur due to the transfer step. This effect can be reduced by transfering the film at a slower rate with the transfer arm mentioned previously.

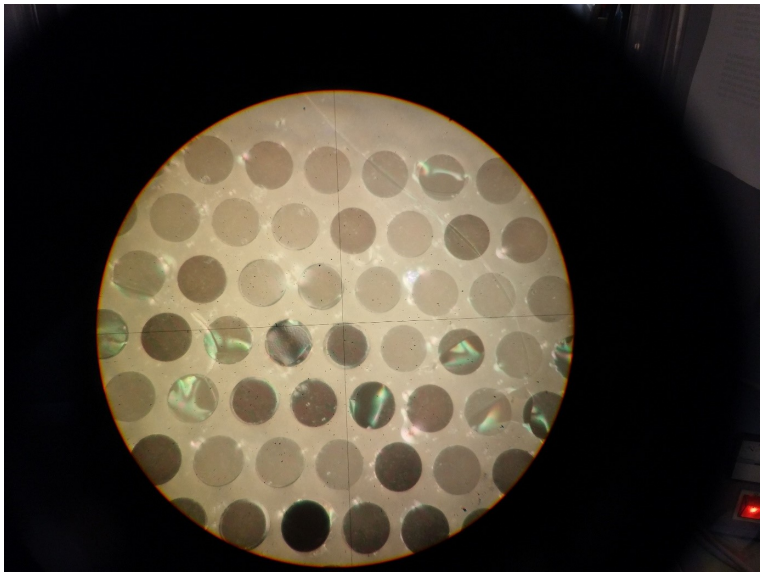

Figure 4.26: Microscope image of the self supported film before calcination of sample T3D Silica (substrate 6).

The more important step is the oservation of the film post-calcination. As the calcination can be very heavy on the mesoporous silica and the thermal expansion properties can cause breakages and curling to occur. With Scanning Electron Microscopy (SEM), it was possible to obtain images to determine the quality of the final film over the open medium. In Fig. 4.27, it can be seen that the silica exists over the open area in its entirety. This is a first time to see a mesoporous thin film over this quantity of open area and stay in its entirety. Due to the sub-micron thicknesses, these films suffer from a high amount of fragility. So great care needs to be undertaken for any experimentation with these films.

The transmission samples measured by means of Positron Annihilation techniques was prepared with substrate 6 (see Table 4.1). New samples are prepared during the writing of this thesis.

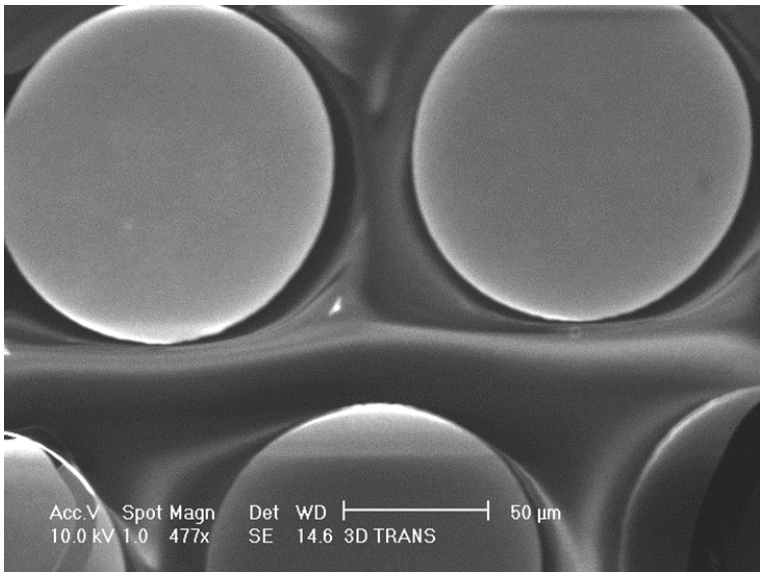

Figure 4.27: SEM image of the mesoporous silica over the empty area of the fused silica substrate after calcination of sample T3D Silica.

4.4 Positron Annihilation results in 3D Silica

4.4.1 Positronium formation

The 3D Silica sample was exposed to the VEPAS slow positron beam for the measurement of the ortho-positronium (o-Ps) yield of the SiO_2 scaffold [99]. The goodness of these features could be considered as a first test for a positron to positronium target performance: the fraction of positronium atoms emitted into vacuum are indeed strictly related to the overall positronium formation and to its possibility to diffuse until the sample surface [100].

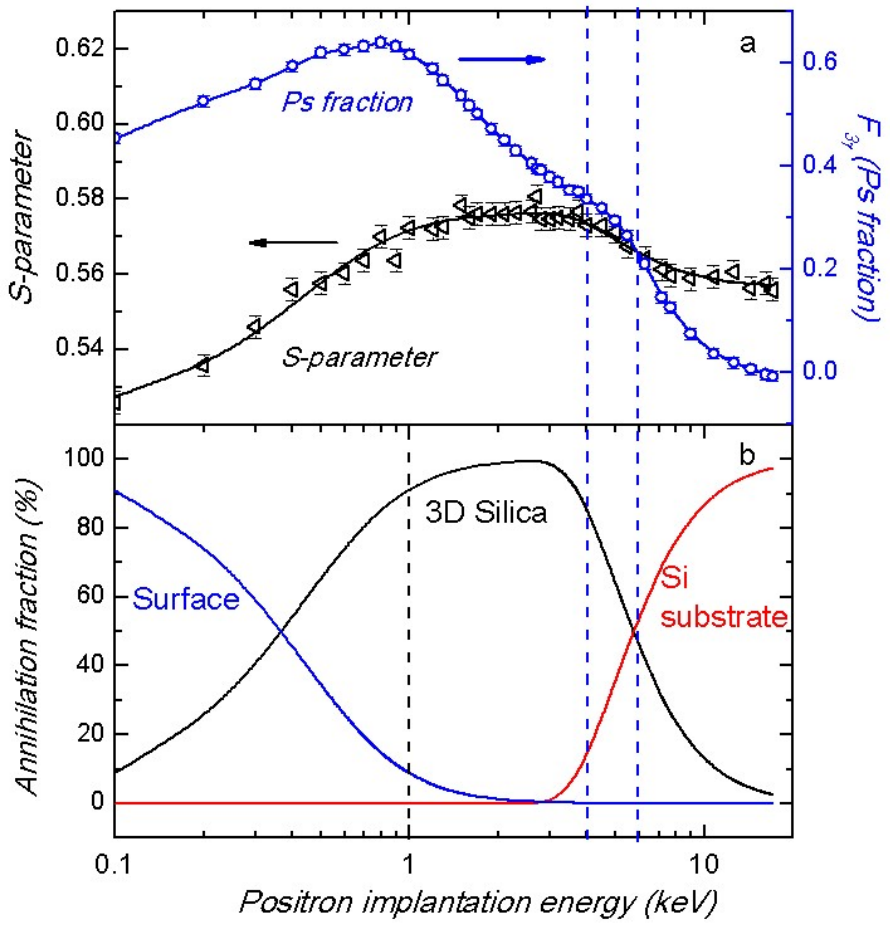

Figure 4.28: a) S-Parameter (black triangles) and o-Ps fraction (blue circles for the 3D Silica sample. The black line represents the VEPFIT best fit of the S-parameter. The blue line is a guide for the eye. b) Annihilation fraction at the surface, into the 3D Silica sample and the substrate.

The energy of the beam ranged from 0.1 keV to 17 keV allowing a complete depth profile, from the surface of the silica to the supporting silicon substrate. The positron annihilation spectra were collected by two HPGe detectors were subsequently analysed in order to calculate both the S-parameter and the three-γ fraction $F_{3\gamma}$ (or Ps fraction), according to the methods described in section (2.2.2) . Figure 4.28a shows the experimental results as a function of the positron implantation energy, while Fig. 4.28b presents the annihilation fraction within each part of the sample: the surface, the mesoporous silica

layer and the silicon substrate at the end.

The evolution of the S-parameter in Fig. 4.28a shows two plateaus. The first for positrons implanted between 1 and 4 keV with a value $S_{SiO_2} \approx 0.58$ corresponding to the mesoporous silica layer. The second, with an asymptotic behaviour, for energies higher than 10 keV tends to $S_{Si} \approx 0.56$ that corresponds to the silicon substrate. Moreover, the steep slope at the lowest implantation energies is symptomatic of a nanometric positron diffusion length inside the silica. In order to give a quantitative description the experimental points were fitted by means of the VEPFIT software [42] using a two-layer model (black line in Fig. 4.28a; the thickness of the mesoporous layer was ranged between 740 nm and 760 nm, as measured by HRTEM, and the free parameters of the model were: the two positron diffusion lengths and the density of the mesoporous silica layer. The best estimations of the parameters were: 0.9 ± 0.1 g cm^{-3} for the density of the mesoporous silica layer, 12 ± 1 nm for the positron diffusion length in silica and 22 ± 10 nm in the p-type silicon (boron, 1-10 Ω cm). In intrinsic Si the positron diffusion length overcomes 200 nm. Instead, in Si p-type decreases to tens of nanometers [101], in agreement with the present finding. In general, positrons diffuse only a few nanometers in mesoporous silica [99]. As a consequence of the short diffusion lengths in silica (compared to the thickness of the mesoporous layer), the vast majority of positrons implanted into the mesoporous silica film form positronium, or positrons that annihilate into the structure of the silica pore walls. In the case with these samples, for positrons implanted within an energy range between 1 and 4 keV (see Fig. 4.28b)).

The Ps fraction curve in Fig. 4.28a (blue circles) brings evidence of the high positronium yield of the 3D Silica material for positrons implanted at energies $\leq$1 keV. More than 60$\%$ of the implanted positrons are converted into Ps; to our knowledge, among the studied positron/Ps converters [12, 80, 99], the Ps yield for the 3D Silica is very high. Between 1 and 4 keV, the shape of the three gamma fraction shows a sharp peak centred at 0.8 keV, followed by a decrease towards higher energies. The form of the peak is related to different

phenomena. At low energies (<0.8 keV) the Ps fraction tends to be lower mainly due to the emission of o-Ps in vacuum at high energy which is not detected (the emission velocities were estimated between 8×10^4 and 5×10^5 m s^{-1} at room temperature [28]. Instead, at higher implantations energies (>1 keV) the Ps fraction decrease is attributed mainly to the Ps migration to the substrate (also at the surface). Another effect that decreases the Ps yield is the pick-off effect, which induces the ortho-positronium atoms to annihilate in two γ rays [102]. There is a range of implantation energies approximately between 4 and 6 keV where the decreasing rate of the Ps fraction suffers a change at about the silica/silicon interface (see the two blue dashed lines in Fig. 4.28). The decrease is due to the more and more positrons implanted into the substrate where the Ps yield tends to zero [103]. The evolution of the Ps fraction in Fig. 4.28a has the typical behaviour to those obtained in thin mesoporous silica films with highly interconnected pores [103, 104], where Ps can annihilate in vacuum even if formed at hundreds of nanometers within. Besides, it has already been proven that a material with a worm-like morphology with pore dimensions similar to the 3D Silica (around 3 nm in diameter, as will be presented below), is suitable for positronium to travel micrometic distances [105].

4.4.2 Positron and Positronium Annihilation Lifetime Spectrometry

The Ps fraction is a useful parameter to evaluate the yield of Ps produced by a certain material, but it does not give information of the amount of Ps emitted into the vacuum. Positron and Positronium Annihilation Lifetime Spectroscopy (PPALS) measurements were performed with the VEPAS beam at a fixed implantation energy (1 keV) in order to obtain information on the amount of Ps emitted in vacuum.

Reflection geometry

The PPALS measurements presented in this section are devoted to characterize the 3D Silica target and test if it emits o-Ps in vacuum in the reflection geometry following the

idea shown in Fig. 4.29. A comparison between two cases with the same mesoporous sample, as prepared and after the deposition of a compact capping layer of silica by e-beam evaporation. Samples identified as 3D Silica and 3D Silica C, respectively. The HRTEM micrograph of Fig. 4.30 shows a capping layer of about 10 nm thick of compact SiO_2 over the mesoporous film in sample 3D Silica C.

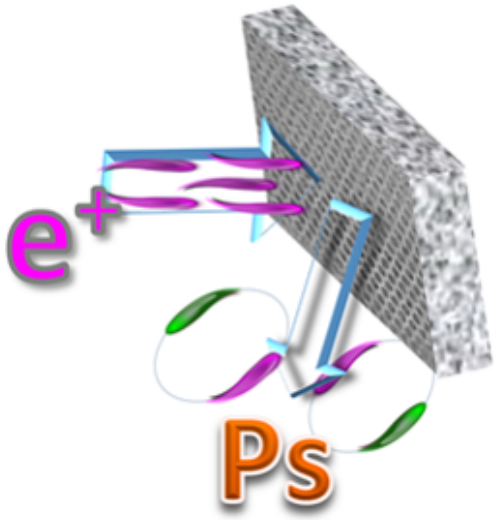

Figure 4.29: Positronium production in the reflection geometry

The o-Ps produced by positrons implanted into the mesoporous film which feature the capping layer (3D Silica C) cannot reach the vacuum. The compact capping layer eliminates this possibility. Instead, Fig. 4.28 showed that in 3D Silica sample the majority of positrons implanted at 1 keV ($\approx 92\%$) into the mesoporous film form Ps. The comparison of these two cases are important to identify the lifetime component of o-Ps confined into the mesopores, that gives information of the characteristics of the sample, and test the o-Ps emission into the vacuum.

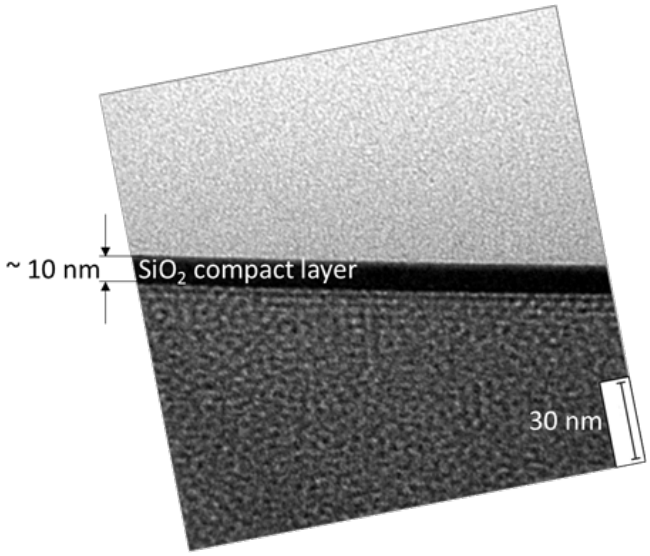

Figure 4.30: HRTEM picture of the 3D Silica C sample showing the presence of a 10 nm thick compact silica layer.

Figure 4.31 shows the PPALS spectra normalized to their peak height value for the 3D Silica samples before, and after the deposition of the capping layer. The area under these spectra is about 10^6 counts taken in one week (at $\approx$1.7 Hz). In the spectra it is possible to distinguish the following details: i) a prompt peak (started at t= 0); ii) a narrower peak due to the positron backscattered phenomenon, as discussed in the Appendix A (the position of this peak depends of the distance between the target and the MCP) and iii) a series of exponential decays that correspond to different positron and positronium lifetimes. The prompt peak is mainly populated by the events related to positrons annihilating within the bulk microstructure of the material (from hundreds of picoseconds to few nanoseconds [12]) and p-Ps annihilation events (125 ps), while the tails of the spectrum are ascribed to the long-lived o-Ps atoms. In Fig. 4.31 it is possible to observe on the right a decrease of the area under the long Ps lifetime component after the deposition of the compact capping layer.

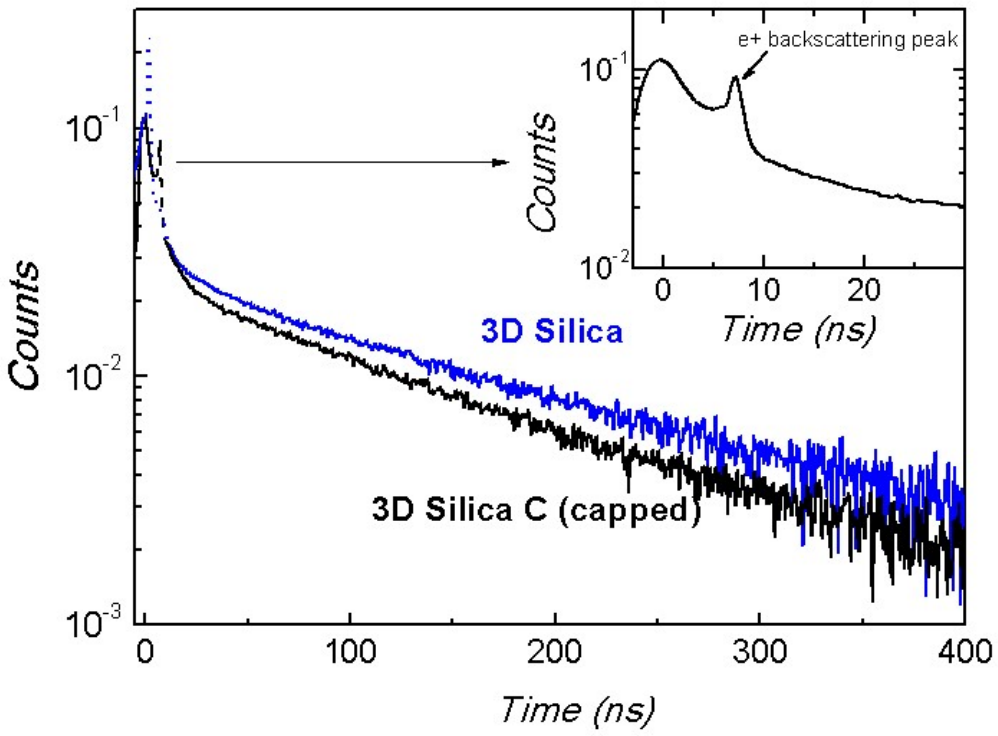

Figure 4.31: PPALS spectra for the 3D Silica with and without the capping layer normalized to the peak value. In the inset:a detail of the prompt peak region of the capped sample (see Appendix A).

In all cases, the spectra were best decomposed into three discrete components (after subtraction of the narrow backscattering peak). The goodness of the model fitting were 0.98 and 0.97 for sample uncapped and capped, respectively. Table 4.2 shows the quantitative results of the analysis. Starting from the left of this table, the components are ascribed to: 1. positrons free annihilations with the electrons of the material, p-Ps annihilations and o-Ps that annihilates into sub-nanometric voids with an average value $\tau_1 = 2.0 \pm 0.5$ ns [12, 106]; 2. annihilation of o-Ps confined within the silica mesoporores ($\tau_2 = 56 \pm 3$ ns); 3. o-Ps annihilating in vacuum with a mean lifetime $\tau_3 = 142$ ns [107]. The mean lifetime of the third component is a well-known value and was fixed to help the determination of the other parameters. For clarity reasons, it is worth pointing out that the o-Ps lifetime of the third

Sample	τ_1(ns)	$I_1(\%)$	τ_2(ns)	$I_2(\%)$	$\tau_3(ns)$	$I_3(\%)$	R^2
3D Silica	2.0(5)	40(2)	56(3)	42(5)	142F	18(3)	0.97
3D Silica C	2.0(5)	61(6)	56(3)	34(3)	142F	5(1)	0.98

Table 4.2: Intensities and mean lifetimes obtained with the fitting procedure for the sample without and with the capping layer. The R^2 fitting parameter is also included.

component reduces its value inside the pores because of the pick-off effect. The relation between the reduced lifetime and the pore dimension is described by a well-established quantum mechanical model Tao-Eldrup [27]. The value found is 56 ns corresponding, under the hypothesis of cylinder-shape tubes at room temperature (≈295 K, temperature of the sample during the measurement), to a diameter of 3.2±0.1 nm; this is in good agreement with the XRD results (see Fig. 4.15) that demonstrate a ≈4 nm periodicity of the SiO_2 scaffold after calcination, considering the space occupied by the pore walls(see Section (4.3.1).

The intensity of the third component is only 5% after the deposition of the capping layer. This low value, as mentioned before, is due to the positrons implanted into the mesoporous volume not being able to reach the vacuum. Only a fraction of the positrons implanted into the capping layer can migrate at the surface and form positronium. Near 40% of the positrons are implanted into the capping layer with 1 keV of implantation energy, consequently positrons annihilates into the compact amorphous SiO_2 microstructure and so the intensity of the first component grows if compared with the uncovered sample. The most interesting thing is to notice that the intensity of the third component is near 18%. This high value demonstrates the emission into the vacuum of an important amount of formed o-Ps.

Transmission geometry

The sample T3D Silica is a quasi-free standing mesoporous membrane. It was prepared with the same technology of the sample 3D Silica, but with the addition that the mesoporous film was transferred to a holed fuse silica substrate (see Sec. 4.3.3). The holed area of the

substrate is ≈68% (substrate 6 in Table 4.1). The PPALS measurements presented in this section were performed mainly to test if this target emits o-Ps in vacuum in transmission geometry following the idea shown in Fig. 4.32.

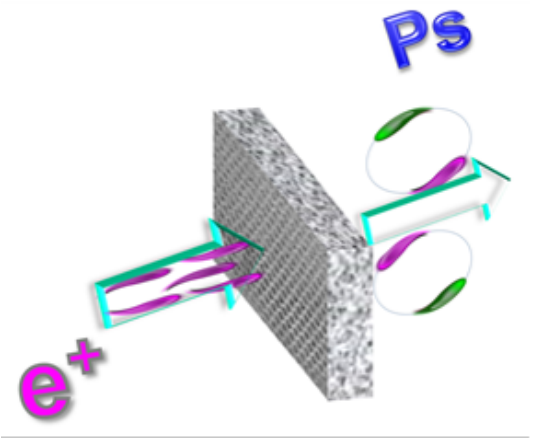

Figure 4.32: Positronium production in the transmission geometry.

T3D Silica was capped by e-beam evaporation before the PPALS measurement to be compared to the results of 3D Silica C presented in the precedent section. The capping layers were grown in the same conditions for both samples (Fig. 4.30). The capping layer was especially designed in silica to produce an additional effect. The o-Ps formed inside the mesopores move in random directions. An amount of Ps atoms that tend to escape in the back direction (opposite to the implanted positrons) interact with the capping layer and are reflected back into the target (transmission direction). Silica was chosen because it is a material that has a low pick-off efficiency. For this reason, it is used to produce and cool positronium.

Figure 4.33 shows a comparison between samples T3D Silica C and 3D Silica C. More interesting is to observe the change of the slope of the tail for the target produced with the holed substrate. That exponential decay is slower than the former two (3D Silica and 3D Silica C) and represents an indication of a substantial increase of the intensity of the positronium lifetime component in vacuum. This is in agreement with Table 4.3 that shows a noticeable increase for the intensity of the third component (142 ns). In both cases, o-Ps

formed inside the mesoporous membrane cannot be emitted in reflection geometry due to the presence of the compact capping layer. The increment of the intensity of the third component only can be justified by the emission of o-Ps atoms in vacuum in the transmission geometry after diffusion and cooling into the mesopores. Previous calculations have shown that using the transmission geometry is optimal for the cooling of Ps. A higher amount of cooled o-Ps in vacuum would be obtain in transmission if compared with the reflection geometry [37]. This condition is suitable and necessary for antimatter experiments as AEgIS and QUPLAS presented in Chapter 3 of this current work.

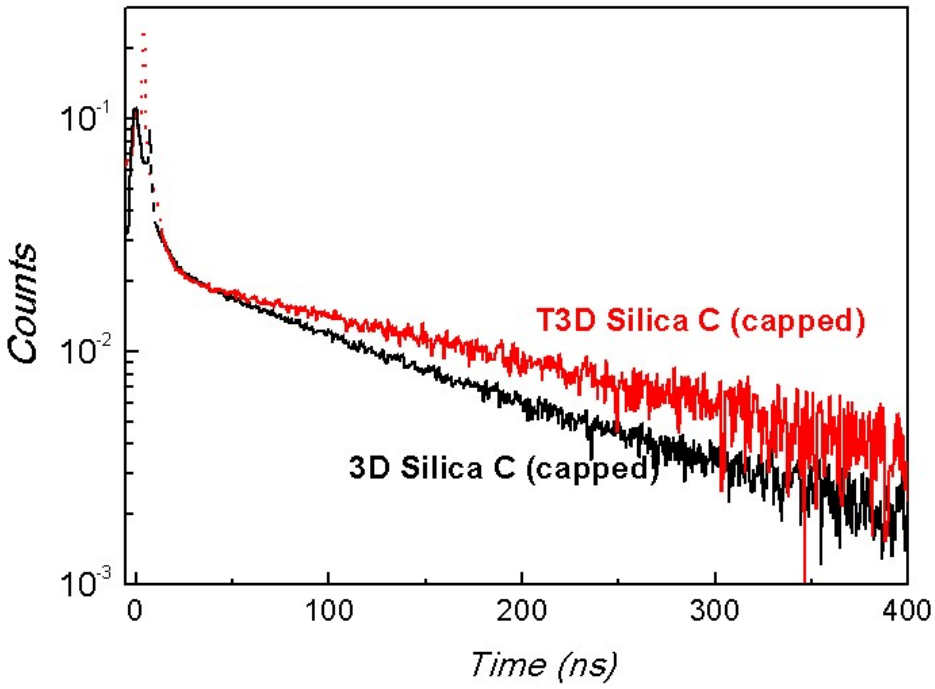

Figure 4.33: PPALS spectra normalized to the peak value for the 3D Silica C and T3D Silica C capped samples.

Sample	τ_1(ns)	$I_1(\%)$	τ_2(ns)	$I_2(\%)$	$\tau_3(ns)$	$I_3(\%)$	R^2
3D Silica C	2.0(5)	44(2)	56(3)	18(5)	142F	38(4)	0.90
T3D Silica C	2.0(5)	61(6)	56(3)	34(3)	142F	5(1)	0.98

Table 4.3: Intensities and mean lifetimes obtained with the fitting procedure for the samples 3D Silica C and T3D Silica C. The R^2 fitting parameter is also included.

CHAPTER 5
CONCLUSION

The main research presented in this thesis provides an alternative self-standing silica target for Ps production in the transmission geometry. This included using novel ways for the fabrication of mesoporous silica thin films, which have the ability to self-stand over an open medium. A fused-silica substrate to maximize the open areas was specially designed and fabricated. This incorporated a spin-coating method which implemented a hybrid transferal process to allow 740 nm thick silica to hold form over an open area.

The VEPAS slow positron beam was utilized for the determination of the positronium yield, the lifetime within the pores and an estimate on the amount of o-Ps in vacuum.

Further measurements need to be undertaken for a better understanding of the o-Ps properties emitted in the transmission geometry, a main one would be a Ps-TOF measurement. This would provide information on the emission energies of the o-Ps.

This material is a good candidate for the proposed upgrade to the Ps production system at AEgIS and a source of Ps for the interferometric measurements with QUPLAS.

APPENDIX A

POSITRON BACKSCATTERED PEAK IN THE LIFETIME SPECTRA

The lifetime spectra discussed in Sec. 4.4.2 show the presence of a narrow peak shifted to the right, in respect to the prompt position, of a few nanoseconds towards higher timings. An example is given in Fig. A.1, black line, for the capped sample 3D Silica C (see Fig. 4.31) at a positron implantation energy of 1 keV. According to our interpretation, this peak is to be ascribed to those signals not triggered by the secondary electrons emitted by the sample surface.

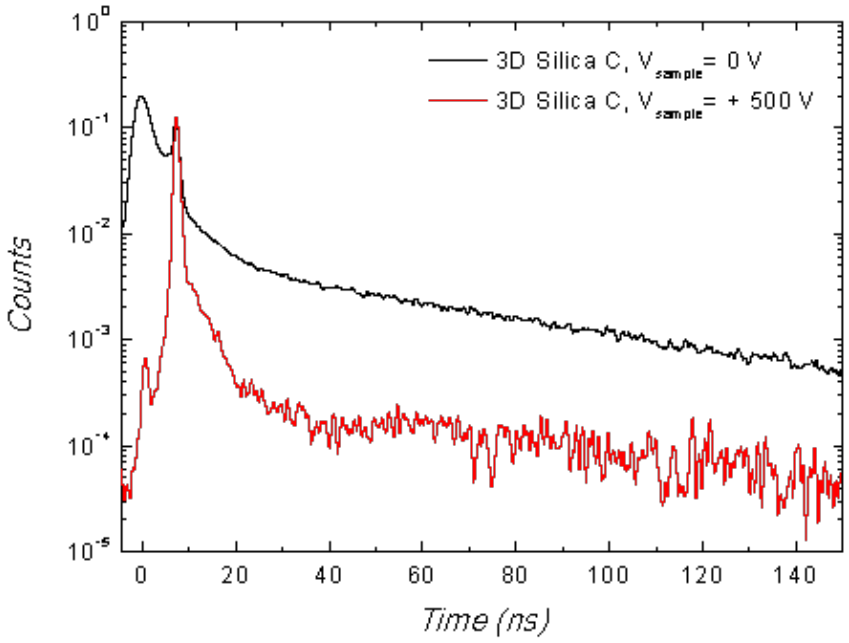

Figure A.1: Black distribution: lifetime spectrum obtained from the silica mesoporous sample after the addition of a thin film of compact silica; red distribution: lifetime spectrum of the same sample raised at 500 V potential in order to avoid signals triggered by the secondary electrons. Both the spectra were taken at 1 keV positron implantation energy.

The start signal of the lifetime spectrometer is given by the secondary electrons, read

by the MCP, produced by the implantation of positrons within the sample. The stop signal, instead, is due to the gamma rays generated from the annihilation process and detected by the BaF_2 scintillator. However, that chain of events can be altered when a positron is backscatterd instead of being implanted [108]. In that case, indeed, the positron is likely to hit the MCP microchannels producing an avalanche of secondary electrons that gives rise to the start signal, while the positron is driven by the MCP electric field towards the first plate where eventually annihilates.

The start signal can then be triggered by two different particles characterized by two significantly different kinetic energies: the secondary electrons with a kinetic energy of tens of eV [47], and the backscattered positrons with a kinetic energy of the same order of magnitude as the implantation energy (in our case $\approx$1 keV) [108]. As a consequence, the two processes are characterized by two prompt peaks with a time shift equal to the difference of the time of flights from the sample surface to the MCP, of the secondary electrons and backscattered positrons, respectively. It is worth noting that the fastest process, i.e. the backscattered positrons, gives rise to an early start signal and, therefore, to a delayed prompt peak (as shown in Fig. A.1).

The time of flight of the secondary electrons can be estimated from the ratio of the average distance between the sample surface and the MCP active area, to the electrons mean momentum. The former is about 1.6 ± 0.1 cm and the latter, considering a kinetic energy of 20 ± 10 eV [47], is about $2.6\pm0.6\times10^6$ m s^{-1}; accordingly the mean time of flight is 6 ± 2 ns. The estimation of the time of flight of the backscattered positrons is calculated in a similar way but with a much higher momentum of 2×10^7 m s^{-1}, i.e. 1 keV of kinetic energy, which leads to a time of flight of 0.80 ± 0.05 ns. These values are in good agreement with all spectra. In Fig. A.1, in particular, the time shift between the two peaks is 7 ns.

With the aim to give an experimental proof of our interpretation as well as to study the shape of the spectrum related only to the backscattered positrons, we performed a lifetime

measurement with the sample at potential of +500 V and the positron beam at 1.5 keV (so to keep the positron implantation energy at 1 keV). The sample potential prevented the secondary electrons to reach the MCP. The outcome of the experiment is presented in Fig. A.1, which shows two spectra: the black evolution represents the spectrum of the capped mesoporous silica thin film and the red evolution represents a spectrum taken in the same conditions except for the 500 V potential imposed on to the sample. It is clear that the second peak in the first spectrum is due to the backscattering of positrons. It is also interesting to note that the red curve is characterized by a lifetime distribution having a mean lifetime of about 4 ns. It might be concluded that positronium production is also involved in the backscattering process.

REFERENCES

[1] P. A. M. Dirac, "The Quantum Theory of the Electron", Proc. R. Soc. of Lond. A, vol. 117 (1928) 610.

[2] C. D. Anderson, "The Positive Electron", Phys. Rev., vol. 43 (1933) 491.

[3] G. Lüders, "Proof of the TCP theorem", Ann. Phys., vol. 2 (1957) 1.

[4] S. De Benedetti, C. E. Cowan and W. R. Konneker, "Angular Distribution of Annihilation Radiation", Phys. Rev., vol. 76, (1949) 440.

[5] J. W. M. Dumond, D. A. Lind and B. B. Watson, "Precision Measurement of the Wave-length and Spectral Profile of the Annihilation Radiation from Cu^{62} with the Two-Meter Focussing Curved Crystal Spectrometer", Phys. Rev., vol. 75 (1949) 1226.

[6] R. Krause-Rehber and H. S. Leipner, "Positron Annihilation in Semiconductors: Defect studies.", Springer Series in Solid-State Sciences, vol. 127 (Springer, Berlin, 1999).

[7] S. Berko and J. Mader, "Momentum Density and Fermi-surface Measurements in Metals by positron annihilation in metal and alloys; Recent experiments with a multicounter two-dimension angular correlation apparatus", J. Appl. Phys., vol. 5 (1974) 287.

[8] A. Dupasquier and W. Brandt, "Positronlike systems in Solids" in Positron Solid State Physics, North-Holland Publishing, 1983.

[9] A. Somoza, A. Dupasquier and R. Ferragut, "Advances in positron studies of age hardening in light alloys", Phys. Stat. Sol. C, vol. 6 (2009) 2295.

[10] F. Tuomisto and I. Makkonen, "Defect indentification in semiconductors with positron annihilation: Experiment and theory", Rev. Mod. Phys., vol 85 (2013) 1583.

[11] Y. C. Jean, P. E. Mallon and D. M. Schrader, "Principles and applications of Positron & Positronium Chemistry", River Edge, New Jersey, Singapore: World Scientific (2003).

[12] G. Consolati, R. Ferragut, A. Galarneau, F. Di Renzo and F. Quasso, "Mesoporous materials for antihydrogen production", Chem. Soc. Rev., vol. 42 (2013) 3821.

[13] C. Hugenschmidt, “Positrons in surface physics”, Surf. Sci. Rep, vol. 71 (2016) 547.

[14] J. A. Baker, M. Touat and P. G. Coleman, “Branching Ratios for electron-volt positrons a a Cu(110) surface”, J. Phys. C: Solid State Phys., vol. 21 (1998) 4713.

[15] Th. Gessmann, M. P. Petkov, M. H. Weber, K. G. Lynn, K. P. Rodbell, P. Asoka-Kumar, W. Stoeffl and R. H. Howell, “Study of Positronium in Low-k Dielectric Films by Means of 2D-Angular Correlation Experiements at a high-Intensity Slow-positron beam”, 12th Int. Conf. Pos. Ann., vol. 363 (2001) 585.

[16] S. Valkealahti and R. M. Nieminen, “Monte Carlo calculations of keV electron and positron slowing down in solids. II”, Appl. Phys. A, vol. 35 (1984) 51.

[17] A. P. Mills Jr and R. J. Wilson, “Transmssion of 1 - 6 keV positrons through thin metal films”, Phys. Rev. A, vol. 26 (1982) 490.

[18] K. G. Lynn and H. Lutz, “Slow Positrons in single-crystal samples of Al and Al-Al_x O_y”, Phys. Rev. B, vol. 22 (1980) 4143.

[19] W. Brandt, “Positrons dynamics in solids” Appl. Phys. A, vol. 5 (1974) 1.

[20] M. J. Puska, C. Corbel and R. M. Nieminen, “Positron trapping in semiconductors”, Phys. Rev. B, vol. 41 (1990) 9980.

[21] St. Mohorovičić, “Möglichkeit neuer Elemente und ihre Bedeutung für die astrophysik”, Astronomische Nachrichten, vol. 253 (1934) 93.

[22] A. E. Ruark, “Positronium”, Phys. Rev., vol. 68 (1945) 278.

[23] J. Pirenne, “The proper field and the interaction of Dirac I - III”, Arch. Sci. phys. nat, vol. 28 (1946) 233.

[24] A. Ore and J. L. Powell, “Three-Photon Annihilation of an Electron-Positron Pair”, Phys. Rev., vol. 75 (1949) 1696.

[25] M. Deutsch, “Evidence for the Formation of Positronium in Gases”, Phys. Rev., vol. 82 (1951) 455.

[26] A. Ore, “Three-Photon Annihilation of an Electron-Positron Pair”, Phys. Rev., vol. 75 (1949) 1696.

[27] S. J. Tao, “The Formation of Positronium in Molecular Substances”, Phys. Rev., vol. 10 (1975) 67.

[28] Y. Nagashima and Y. Morinaka and T. Kurihara and Y. Nagai and T. Hyodo and T. Shidara and K. Nakahara, "Origins of positronium emitted from SiO_2", Phys. Rev. B, vol. 58 (1998) 12676.

[29] D. B. Cassidy et al., "Positronium cooling in porous silica measured via Doppler spectroscopy", Phys. Rev. A, vol. 81 (2010) 012715.

[30] S. Mariazzi, A. Salemi and R. S. Brusa, "Positronium cooling into nanopores and nanochannels by phonon scattering", Phys. Rev. B, vol. 78 (2008) 085428.

[31] J. Algers, P. Sperr, W. Egger, G. Kögel and F. H. J. Maurer, "Median implantating depth and implantation profile of 3-18 keV positrons in amorphous polymers", Phys. Rev. B, vol. 67, (2003) 125404.

[32] M. Eldrup, D. Lightbody and J. N. Sherwood, "The temperature dependence of positron lifetimes in solid pivalic acid", J. Chem. Phys., vol. 63 (1981) 51.

[33] G. S. Kanda, L. Ravelli, B. Löwe, W. Egger and D. J. Keeble, "Positron annihilation lifetime spectroscopy study of kapton thin foils", J. Phys. D: Appl. Phys., vol. 49 (2016) 025305.

[34] G. F. Knoll, "Radiation Detection and Measurement", University of Michigan. Ann Arbor, Michigan. John Wiley $\&$ Sons (1999).

[35] P. Kirkegaard, N. J. Pedersen and M. M. Eldrup, "PATFIT-88 A data-processing system for positron annihilation spectra on mainframe and personal computers", Risø National Laboratory Press, DK-4000 Roskilde, Denmark, vol. 2740 (1989).

[36] J. Kansy, "Microcomputer Program for Analysis of Positron-Annihilation Lifetime Spectra", Nucl. Instrum. Methods Phys. Res., Sect. A, 373 (1996) 235.

[37] S. Aghion, "Study of thin films and mesoporous materials by means of positron annihilation spectroscopy for applied and fundamental physics," PhD thesis, Politecnico di Milano, 2015.

[38] R. Anderson-Sprecher, "Model Comparisons and R^2", A. Stat. 48 (1994) 113.

[39] K. G. Lynn and B. Nielsen, "Development and use of a thin-film transmission positron moderator", Appl. Phys., Lett. 47 (1985) 239.

[40] K. F. Canter, P.H. Lippel, W. S. Crane, A. P. Mills Jr., "Development of high brightness low positron beams", Positron Studies of Solids, Surfaces, and Atoms, World Scientific (1986), 199.

[41] D. A. Dahl, "SIMION for the personal computer in reflection", Int. J. Mass Spectrom, vol. 200 (2000) 3.

[42] A. van Veen et al., "Analysis of positron profiling data by means of VEPFIT", AIP Conf. Proc., vol. 218 (1991) 171.

[43] K. G. Lynn, J. R. MacDonald, R. A. Boie, L. C. Feldman, J. D. Gable and M. F. Robbins,"Positron-Annihilation Momentum Profiles in Aluminum: Core Contribution and the Independent-Particle Model", Phys. Rev. Lett. 38 (1977) 241.

[44] K. G. Lynn and D. O. Welch, "Slow positrons in metal single crystals. Positronium formation at Ag (100), Ag (111) and Cu (111) surfaces", Phys. Rev. B, vol. 22 (1980) 99.

[45] A. P. Mills Jr., "Positronium Formation at Surfaces", Phys. Rev. Lett., vol. 41 (1978) 1828.

[46] S. Szpala, M. P. Petkov and K. G. Lynn, "A simple positron lifetime spectrometer for magnetically guided low-energy beam", Rev. Sci. Instrum., vol. 73 (2002) 147.

[47] E. Schreiber and H.-J. Fitting, "Monte Carlo simulation of secondary electron emission from the insulator SiO_2", J. Electron. Spectrosc. Relat. Phenom., vol. 124 (2002) 25.

[48] O. Chamberlain, E. Segrè, C. Wiegand and T. Ypsilantis, "Observation of Antiprotons", Phys. Rev., vol. 100 (1955) 947.

[49] B. Cork, G. R. Lambertson, O. Piccioni and W. A. Wenzel, "Antineutrons Produced from Antiprotons in Charge Exchange Collisions", Phys. Rev., vol. 104 (1956) 1193.

[50] T. Massam, Th. Muller, B. Righini, M. Schneegans and A. Zichichi, "Experimental observation of antideuteron production", Il Nuovo Cimento, vol. 63 (1965) 10.

[51] D. E. Dorfan, J. Eades, L. M. lederman, W. Lee, and C. C. Ting, "Observation of Antideuterons", Phys. Rev. Lett., vol. 14 (1965) 1003.

[52] G. Baur et al., "Observation of antihydrogen produced in flight at CERN", Hyperfine Interact., vol. 109 (1997) 191.

[53] S. Baird et al., "The Antiproton Decelerator: AD", Nucl. Instrum. Meth. A, vol. 391 (1997) 210.

[54] K. S. Fine and the ATHENA Collaboration, "The ATHENA antihydrogen experiment", AIP Conf. Proc., vol. 498 (1999) 40.

[55] G. Gabrielse et al., "Background-Free Observation of Cold Antihydrogen with Field-Ionization Analysis of Its States", Phys. Rev. Lett., vol. 89 (2002) 213401.

[56] T. Yamazaki, N. Morita, R. S. Hayano, E. Widmann and J. Eades, "Antiprotonic helium", Phys. Rep., vol. 366 (2002) 183.

[57] S. Maury. W. Oelert. W. Bartmann. P. Belochitskii. H. Breuker. F. Butin. C. Carli. T. Eriksson. S. Pasinelli and G. Tranquille, "ELENA: the extra low energy antiproton facility at CERN", Hyperfine Interact., vol. 229 (2014) 105.

[58] P. Belochitskii, T. Eriksson and S. Maury, "The CERN antiproton decelerator (AD) in 2002: status, progress and machine development results", Nucl. Instrum. Meth. B, vol. 214 (2004) 176.

[59] A. Kellerbauer et al. (AEGIS Proto-Collaboration), "Proposed antimatter gravity measurement with an antihydrogen beam", Nucl. Instrum. Meth. B, vol. 226 (2008) 351.

[60] G. Drobychev et al. (AEGIS Proto-Collaboration), "Proposal to the SPS Experiments Committee", SPSC-2007-017, CERN (2007).

[61] D. S. Hajdukovic, "Dark energy, antimatter gravity and geometry of the Universe", Astrophys. Space Sci., vol. 330 (2010) 1.

[62] J. D. Anderson and J.G Williams, "Long-range tests of the equilavence principle", Class. and Quantum Grav. (2001) 2447.

[63] S. Schlamminger, K.Y. Choi, T. A. Wagner, J. H. Gundlach and E. G. Adelberger, "Test of the Equivalence Principle Using a Rotating Torsion Balance", Phys. Rev. Lett., vol. 100 (2008) 041101.

[64] R. S. Van Dyck Jr., D. J. Wineland, P. A. Ekstrom and H. G. Dehmelt, "High mass resolution with a new variable anharmonicity Penning trap", Appl. Phys. Lett., vol. 28 (1976) 446.

[65] T. W. Darling, F. Rossi, G. I. Opat and G. F. Moorhead, "The fall of charged particles under gravity: A study of experimental problems", Rev. Mod. Phys., vol. 64 (1992) 1.

[66] The ALPHA Collaboration and A. E. Charman, "Description and first application of a new technique to measure the gravitational mass of antihydrogen", Nature Commun., vol. 4 (2013) 1785.

[67] E. A. Hessels, D. M. Homan and M. J. Cavagnerol, “Two-stage Rydberg charge exchange: An efficient method for production of antihydrogen”, Phys. Rev. A, vol. 57 (1998) 1668.

[68] M. Charlton, “Antihydrogen production in collisions of antiprotons with excited states of positronium”, Phys. Lett. A, vol. 143 (1990) 143.

[69] T. Breeden and H. Metcalf, “Stark Acceleration of Rydberg Atoms in Inhomogeneous Electric Fields”, Phys. Rev. Lett., vol. 47 (1981) 1726.

[70] S. L. Rolston and G. Gabrielse, “Cooling antiprotons in an ion trap”, Hyperfine Interact., vol. 44 (1988) 233.

[71] M. K. Oberthaler et al., “Inertial sensing with classical atomic beams”, Phys. Rev. A, vol. 54 (1996) 3165.

[72] G. Testera et al. (AEgIS Collaboration), “Formation Of A Cold Antihydrogen Beam in AEGIS for Gravity Measurements”, AIP Conf. Proc., vol. 1037 (2008) 5.

[73] S. Aghion et al. (AEgIS Collaboration), “A moiré deflectometer for antimatter”, Nature Commun., vol. 5 (2014) 4538.

[74] C. Pistillo et al. (AEgIS Collaboration), “Emulsion detectors for the antihydrogen detection in AEgIS”, Hyperfine Interact., vol. 233 (2015) 29.

[75] S. Aghion et al. (AEgIS Collaboration), “Positron bunching and electrostatic transport system for the production and emission of dense positronium clouds into vacuum”, Nucl. Instrum. Meth. B, vol. 362 (2015) 86.

[76] S. Aghion et al. (AEgIS Collaboration), “Laser excitation of the n3 level of positronium for antihydrogen production”, Phys. Rev. A, vol. 94 (2016) 012507.

[77] S. Cialdi, I. Boscolo, F. Castelli, F. Villa, G. Ferrari and M. G. Giammarchi, “Efficient two-step Positronium laser excitation to Rydberg levels”, Nucl. Instrum. Meth. B, vol. 269 (2010) 1527.

[78] S. L. Andersen et al., “Positronium formation from porous silica in backscattering and transmission geometries”, Eur. Phys. J. D, vol. 68 (2014) 124.

[79] D. B. Cassidy, S. H. M. Deng, H. K. M. Tanaka and A. P. Mills Jr., “Single shot positron annihilation lifetime spectroscopy”, Appl. Phys. Lett., vol. 88 (2006) 194105.

[80] S. Mariazzi, P. Bettotti, S. Larcheri, L. Toniutti and R. S. Brusa, “High positronium yield and emission into the vacuum from oxidized tunable nanochannels in silicon”, Phys. Rev. B, vol. 81 (2010) 235418.

[81] S. Aghion et al. (AEgIS Collaboration), "Characterization of a transmission positron/ positronium converter for antihydrogen production", Nucl. Instrum. Meth. B, vol. 407 (2017) 55.

[82] S. L. Andersen et al., "Positronium emission and cooling in reflection and transmission from thin meso-structured silica films", J. Phys. B At. Mol. Opt. Phys., vol. 48 (2015) 204003.

[83] C. Davisson and L. H. Germer, "Diffraction of Electrons by a Crystal of Nickel", Phys. Rev., vol. 30 (1927) 705.

[84] H. von Halban and P. Preiswerk, "Experimental evidence of neutron diffraction", C.R. Hebd. Séances Acad., vol. 203 (1936) 73.

[85] H. von Halban and P. Preiswerk, "Beugung von Molekularstrahlen", C.R. Hebd. Séances Acad., vol. 61 (1930) 95.

[86] S. Aghion, A. Ariga, T. Ariga, M. Bollani, E. Dei Cas, A. Ereditato, C. Evans, R. Ferragut, M. Giammarchi, C. Pistillo, M. Romé, S. Salab and P. Scampolic, "Detection of low energy antimatter with emulsions", J. Instrum., vol. 11 (2016) P06017.

[87] S. Sala, F. Castelli, M. Giammarchi, S. Siccardi and S. Olivares, "Matter-wave interferometry: towards antimatter interferometers", J. Phys. B: At. Mol. Opt. Phys., vol. 48 (2015) 195002.

[88] C. Amsler, A. Ariga, T. Ariga, S. Braccini, C. Canali, A. Ereditato, J. Kawada, M. Kimura, I. Kreslo and C. Pistillo, "A new application of emulsions to measure the gravitational force on antihydrogen", J. Instrum., vol. 8 (2013) P02015.

[89] K. J. Edler and B. Yang, "Formation of mesostructured thin films at the air-liquid interface", Chem. Soc. Rev., vol. 42 (2013) 3765.

[90] H. Yang, N. Coombs, I. Sokolov and G. A. Ozin, "Free-standing and oriented mesoporous silica films grown at the airwater interface", Nature, vol. 42 (1996) 589.

[91] R. Vogel, C. Dove, A. Whittaker, G. Edwards, J. D. Riches, M. Harvey, M. Trau and P. Meredith, "Postsynthesis stabilization of free-standing mesoporous silica films", Langmuir, vol. 381 (2004) 2908.

[92] H. Yang, G. A. Ozin and C. T. Kresge, "The role of defects in the formation of mesoporous silica fibers, films ad curved shapes", Adv. Mater., vol. 10 (1998) 883.

[93] H. Kanazawa, Y. H. Ohtsuki and S. Yanagawa, "Positronium formation in Metals", vol. 138 (1965) A1155.

[94] S. Besson, T. Gacoin, C. Jacquoid, C. Ricolleu, D. Babonneau and J. Boilot, "Structural study of 3D-hexagonal mesoporous spin-coated sol-gel films", J. Mater. Chem., vol. 10 (2000) 1331.

[95] D. K. Bowen and K. Tanner, "High Resolution X-ray Diffraction and Topography", Taylor & Francis, Ltd. (1998) 113.

[96] Y. Lu, R. Ganguli, C. A. Drewien, M. T. Anderson, C. J. Brinker, W. Gong, Y. Guo, H. Soyez, B. Dunn, M. H. Huang and J. I. Zink, "Continuous formation of supported cubic and hexagonal mesoporous films by solgel dip-coating", Nature, vol. 389 (1997) 354.

[97] R. Bandyopadhyaya, E. Nativ-Roth, R. Yerushalmi-Rozen and O. Regev, "Transferable Thin Films of Mesoporous Silica", Chem. Mater., vol. 15 (2003) 3619.

[98] K. C. Vishnubhatla, N. Bellini, R. Ramponi, G. Cerullo and R. Osellame, "Shape control of microchannels fabricated in fused silica by femtosecond laser irradiation and chemical etching" Opt. Express, vol. 17 (2009) 8685.

[99] R. Ferragut, S. Aghion and G. Tosi, "Positronium production in engineered porous silica", J. Phys. Chem. C, vol. 117 (2013) 26703.

[100] D. B. Cassidy, T. H. Hisakado, V. E. Meligne, H. W. K. Tom and A. P. Mills Jr., "Delayed emission of cold positronium from mesoporous materials", Phys. Rev. A, vol. 82 (2010) 052511.

[101] W. Bauer-Kugelmann, J. A. Duffy, J. Störmer, G. Kögel and W. Trifftshäuser, "Diffusivity and surface transition rate of positrons in crystalline silicon as a dunction of dopant concentration", Appl. Surf. Sci., vol. 116 (1997) 231.

[102] T. Goworek, K. Ciesielski, B. Jasińska and J. Wawryszczuk, "Positronium states in the pores of silica gel", J. Chem. Phys., vol. 230 (1998) 305.

[103] B. Xiong, W. Mao, J. Yue, X. Xu and C. He, "Mesoporosity in silica films studied by a slow positron beam and ellipsometry", Phys. Lett. A, vol. 378 (2014) 249.

[104] C. He, T. Oka, Y. Kobayashi, N. Oshima, T. Ohdaira, A. Kinomura and R. Suzuki, "Evolution of pores in mesoprorous silica films: Porogen loading effect", Appl. Surf. Sci., vol. 255 (2008) 183.

[105] C. He, S. Wang, Y. Kobayashi, A. Kinomura, T. Ohdaira and R. Suzuki, "Role of pore morphology in positronium diffusion in mesoporous silica thin films and in positronium emission from the surface", Phys. Rev. B, vol. 86 (2012) 075415.

[106] K. Sato, D. Shanai, Y. Honani, T. Ougizawa, K. Ito, K. Hirata and Y. Kobayashi, "Positronium formed by recombination of positron-electron pairs in polymers", Phys. Rev. Lett., vol. 96 (2006) 228302.

[107] R. S. Vallery, P. W. Zitzewitz and D. W. Gidley, "Resolution of the orthopositronium-lifetime puzzle", Phys. Rev. Lett., vol. 90 (2003) 203402.

[108] M. J. Puska and R. M. Nieminen, "Theory of positrons in solids and on solid surfaces", Rev. Mod. Phys., vol. 66 (1994) 841.